The Development of a 3D Piezoelectric Active Microtissue Model for Airway Smooth Muscle

by

Matthew Walker

Submitted in partial fulfilment of the requirements
for the degree of Master of Applied Science

at

Dalhousie University
Halifax, Nova Scotia
April 2013

DALHOUSIE UNIVERSITY

School of Biomedical Engineering

The undersigned hereby certify that they have read and recommend to the Faculty of Graduate Studies for acceptance a thesis entitled "The Development of a 3D Piezoelectric Active Microtissue Model for Airway Smooth Muscle" by Matthew Walker in partial fulfilment of the requirements for the degree of Master of Applied Science.

Dated: April 8, 2013

Supervisor: _____

Readers: _____

_____

_____

Departmental Representative: _____

DALHOUSIE UNIVERSITY

DATE: April 8, 2013

AUTHOR: Matthew Walker

TITLE: The Development of a 3D Piezoelectric Active Microtissue Model for Airway Smooth Muscle

DEPARTMENT OR SCHOOL: School of Biomedical Engineering

DEGREE: MASc CONVOCATION: October YEAR: 2013

_____

Signature of Author

Table of Contents

List of Tables

List of Figures

Abstract

Although asthma is primarily thought to be an inflammatory disease of the airways, it has recently been hypothesized that the altered mechanical environment of an asthmatic airway may contribute to the development of the disease through changes in cellular phenotype. In regards to this hypothesis, the effects of stretch on airway smooth muscle (ASM) have previously been investigated using 2D cell culture. However, over the last few years there has been an increasing appreciation to the importance of the role of the 3D extracellular matrix in the regulation of cellular response. For this reason, the work presented in this thesis covers the development of a device capable of high-throughput investigations into the effects of acute or chronic, uniaxial, oscillatory mechanical strain on an array of miniature, 3D, multi-cell, tissue-engineered constructs.

A mathematical model of actuator dynamics with tissue loading was used to identify many important relationships for the optimization of device design. Standard microfabrication techniques were used to manufacture arrays of miniature piezoelectric actuators/sensors out of lead zirconate titanate (PZT). Bimorph actuators with dimensions of 2mmx400μmx70μm (lxwxt) generated an average peak deflection of 12.39±0.49μm when driven with a ±20 volt sinusoidal wave at 0.3 Hz.

The actuators were coated with parylene C to act as a barrier for electrical insulation and biocompatibility. Tissues consisting of 80% ASM cells and 20% 3T3 fibroblasts in a collagen matrix were fabricated within the device. We confirmed that live tissues formed around the tops of the actuators with negligible cell mortality.

A LabVIEW-based, video analysis program was developed to track the peak deflection of the actuators. Using the mathematical model for the actuator dynamics with tissue loading, and comparing peak deflections with and without the presence of the tissues, the stiffness of the tissues were determined during acute strains ranging from ± 0.5% to ±5% when at baseline and after 80mM potassium chloride (KCl), 0.1mM forskolin, and 10μM cytochalasin D. We found that tissue stiffness significantly decreased as the amplitude of mechanical strain increased ($n=4$, $p<0.01$). Moreover, when $<\pm 1\%$ strain was applied, the tissue stiffness following KCl (23.0±2.0N/m), a contractile agonist, was measurably greater than after forskolin (16.9± 5.4N/m), a relaxant agonist, and cytochalasin D (16.8±5.7N/m), an actin polymerization inhibitor ($n=4$, $p<0.1$).

The last part of the thesis provided proof of concept for an alternative method of tracking the deflection of the actuators while simultaneously measuring the tissue force. This method was based upon measuring the charge generated by the capacitance of actuators and the variations caused by externally applied forces. It found to be capable of tracking deflections as small as 4.7nm and should be able to measure tissue mechanical properties if the device contained enough actuators with attached tissues.

To conclude, this thesis has established the feasibility of a piezoelectric straining device for studying the effects of oscillatory stretch in an array of miniature 3D cell cultures. This thesis has also included detailed sections on the potential of the device to directly study cellular mechanics through changes in tissue stiffness and possibly contractility. Taken together, the findings from this thesis indicate that the device should one-day be able to be used to further our knowledge of the roles of stretch and the 3D extracellular matrix in diseases such as asthma.

List of Abbreviations and Symbols Used

ASM = airway smooth muscle
PZT = lead zirconate titanate
KCl = potassium chloride
d = generated tip deflection (m)
Q = generated electrical charge (C)
F = applied tip force (N)
V_{in} = applied voltage (V)
L = length of actuator (m)
w = width of actuator
t_m = thickness of elastic layer (m)
t_p = thickness of piezoelectric layer (m)
s_{11}^m = elastic compliance of elastic layer (m^2/N)
s_{11}^p = elastic compliance of piezoelectric layer (m^2/N)
d_{31} = transverse piezoelectric coefficient (m/V or C/N)
ε_{33}^x = dielectric permittivity (F/m)
ε_o = permittivity of free space ($8.854\times 10^{-12} F/m$)
ε_3^x = dielectric constant (F/m)
S_t = stiffness of the tissue (N/m)
E_t = elastic modulus of the tissue (Pa)
A_t = area of the tissue (m^2)
l_o = initial length of the tissue (m)
s_{11}^c = elastic compliance of coating (m^2/N)
σ = mechanical stress (Pa)
ε = mechanical strain
M = moment of force (N×m)
I = moment of inertia (m^4)
δ = phase (degrees)
C_P = capacitance of piezoelectric actuators (F)
C = capacitance of feedback capacitor (F)
C_R=capacitance of reference capacitor (F)
V_{out} = Output voltage (V)
i_{bias} = bias current of the amplifier (A)
R_{FP} = leakage resistance ofof piezoelectric actuator (Ω)

Acknowledgements

I would like to express my deepest appreciation for my supervisor, Professor Geoff Maksym. Without his never-ending patience and seemingly boundless knowledge, I doubt that I could have reached my goals for this project. I especially want to thank him for the day-to-day interest that he showed not only for this work, but also for my future career aspirations. For his aid in my development as scientist and his mentorship, I am in his debt.

I would also like to thank my committee members, Professor Jeremy Brown and Professor Paul Gratzer. Without the use of Jeremy's microfabrication lab, this research could not have been completed. Moreover, Jeremy's creativity and his continued interest in the project were fundamental to its success. I also greatly appreciated Paul's support that he showed during my committee meetings and his feedback on my progress.

Lastly, I would like to acknowledge the funding that I received from the Nova Scotia Heath Research Fund (NSHRF), and the Canadian Institutes of Health Research (CIHR) grant funding for our laboratory. Their financial support not only aided the completion of this project but also gave me the ability to acquire and improve my laboratory and general research skills to become a better investigator.

Chapter 1: Introduction

1.1 Thesis Structure

This Thesis is organized into six chapters, beginning with an introduction containing the relevant background information, a general hypothesis, and the three thesis aims. Chapters two, four, and five each address an individual aim outlined in the introduction including the rationale, methods, results and discussion. In chapter three, the software developed for tracking the deflection of the actuators is discussed. Chapter six concludes this thesis with a summary of the significant findings and considerations for future work.

1.2 Asthma

Bronchial asthma is one of the most common disorders encountered in clinical medicine today, making it a worldwide health and economic burden (3). It is traditionally regarded as a chronic inflammatory disease of the airways characterized by variable airflow obstruction. The histological features of asthma include infiltration of the airway wall with leukocytes and macrophages, airway surface epithelium shedding and damage, mucous plugging, and airway wall thickening due to subepithelial fibrosis, and hyperplasia and hypertrophy of the airway smooth muscle (ASM) (8). Together these features lead to hyperresponsive and hypersensitive airways that limit the exchange of air into and out of the lungs.

1.3 Airway Smooth Muscle

The medial layer of an airway consists of ASM cells in approximately circumferential orientation. The physiological function of ASM is unclear, however several possible roles have been suggested in the literature including: 1) peristalsis to assist exhalation; 2) peristalsis to assist mucus propulsion; 3) peristaltic contraction in the fetal lung to generate fluid pressure; 4) promoting lymphatic and venous flow; 5) ventilation/perfusion matching; 6) protecting the peripheral lung; 7) protecting airway structure; 8) stabilizing airways; 9) enhancing the effectiveness of cough; and 10) optimizing anatomic dead space volume (41). Seow and Fredberg (47) also commented that because there is no known physiologic deficit associated with its absence, ASM may simply be a vestigial remnant of its common embryologic origin with the gastrointestinal system with no modern function. In any case, it is generally agreed upon that the difficulty in breathing during an asthmatic episode is due to airway narrowing caused by ASM contraction with an excessive amount of cell shortening (2). However, it is not understood whether this is caused by changes in the contractile capability of the ASM, and/or mechanical changes in the elastic load that the muscle works against, which is set by the non-contractile elements of the airway wall and the surrounding lung parenchyma (28).

Although there is compelling evidence in support for both explanations, only the former is within the scope of this thesis. The evidence in support for it follows. First, perhaps one of the most striking and likely significant changes observed in asthmatic subjects is ASM hypertrophy and hyperplasia. A thicker muscle layer likely enhances contractile force generation, which would lead to airway narrowing (30, 44). In addition,

the cells seem to be functionally different. Like other smooth muscle cells (48), ASM cells have been shown to undergo rapid phenotypic modulation in primary culture due to environmental and functional requirements (23), and an increase in contractile protein content has been interpreted in the literature as a switch from a synthetic-proliferative phenotype to a contractile phenotype (22). Since they have a greater amount of myosin light chain kinase per cell (1, 36), it therefore seems that ASM cells from asthmatic airways have a more contractile phenotype. Furthermore, ASM cells from subjects with asthma have a 7 amino acid insert in the myosin heavy chain, which leads to more rapid shortening (34). The significance of a faster muscle is explained later on in the introduction. Lastly, ASM cells in asthmatic airways may differ in their cytoskeletal organization. Greater cytoskeletal organization, which has been shown to result from loading conditions similar to in asthma (5, 6, 19, 49, 50), may increase contractile efficiency and/or decrease the impedance to shortening, leading to greater airway narrowing.

1.4 Stretch Induced Effects in ASM

Stretch is Beneficial

Airway caliber was initially thought to be an equilibrium between a static active force generated by the ASM and the passive reaction force set by the elasticity of the airway wall and lung parenchyma. However, in healthy airways there is strong evidence to suggest that cyclic stretches from tidal breathing and periodic deep inspirations lead to

much greater airway caliber than that predicted by a static system.

One of the most pivotal findings to our understanding of airway caliber demonstrated that cyclic stretching of maximally contracted bovine tracheal muscle tissue strips leads to lengthening and decreases in active tissue force directly corresponding to the stretch amplitude (14, 32). Furthermore, the muscle became less stiff, which reflects the number of actin-myosin interactions, and more hysteretic, which reflects the rate of turnover of those interactions. From these results, it was hypothesized that cyclic loading perturbs the interaction between actin and myosin filaments, and thus, the number of bridge attachments in a static condition is never attained in a dynamic system (15). This is known as the bronchodilatory effect of stretch. Curiously, the effect from large amplitude stretches remained, albeit reduced, when the stretch amplitude was decreased (15). This is known as the bronchoprotective effect of stretch. Although the effect of stretch due to transient deep inspirations and tidal breath are widely accepted, the magnitude and duration of the effect *in vivo* is currently debated (31).

The perturbed actin-myosin binding hypothesis was key to our understanding of the dynamic regulation of airway caliber, however, several investigations into ASM rheology have shown that the relaxation time of cells' elastic modulus do not correspond to the specific attachment/detachment rates of myosin cross bridges (9, 10, 33, 46). Instead, the relaxation times were broadly distributed, and therefore, cannot be associated solely with actomyosin dynamics (29). In other words, the perturbed actin-myosin binding hypothesis is now seen only to be one part of a bigger picture (29). Instead, present understanding of ASM cells considers that their mechanical properties behave as a soft glassy material (SGM). One of the most striking features of SGMs is that in the absence of external perturbations, they act as solids with low Young's modulus (Pa to

kPa), but when subjected to strains of sufficient magnitude they become much more fluid-like. This behavior has been documented in many cell types, including ASM cells. When subjected to a single transient stretch, ASM cells acutely fluidizes their cytoskeleton: both the storage (i.e. elastic stresses) and loss (i.e. frictional stresses) components of their stiffness decreases rapidly together in a strain dependent manner (54). When the stretch is stopped, however, the cell solidifies over hundreds of seconds.

Unfortunately in asthma, both the bronchodilatory and bronchoprotective effects of stretch seem to fail (11, 62), which renders the muscle in a static or 'frozen' state (15). The reason for this impairment remains unclear. It is possible that such behaviour is consistent with airway closure; it is more difficult to expand closed airways (20, 62). Another possibility is that since ASM from asthmatics seems to have a faster intrinsic rate of cycling (34), a detached bridge will more quickly reattach, and once again contribute to active force and stiffness (12). Yet another possibility is that stretch induces a myogenic response in asthmatic ASM. The last possibility worth mentioning is that stretch-induced ASM softening is reduced in asthmatic airways because their ASM may simply receive a smaller amplitude of tidal stretch due to an increase in ASM layer stiffness associated with chronic activation and/or mechanical stress, and/or the decrease in the parenchymal tethering load associated with inflammatory remodeling of the peribronchial adventitia (13, 40, 44).

Stretch can be Harmful

In addition to the inflammatory derivation of Asthma, some investigators have suggested that the hyperresponsiveness and hypersensitivity of the ASM could be due in

part to the altered mechanical environment of an asthmatic airway: primarily through an increase in tone and changes in the loading pattern (40). The most significant contributions to this hypothesis are summarized below.

As previously described, transient stretch in healthy airways can be beneficial, leading to muscle relaxation and larger airway diameters, whereas in asthma, delivery of an acute stretch does not lead to any of these effects. This lack of response to a deep inspiration seen in asthmatic airways is mimicked in individual cells grown with chronic cyclic strain as they more quickly recover their initial stiffness after an acute period of large oscillatory stretches than compared to control cells (40). Therefore, it is possible that chronic mechanical stretch may alter ASM function so that an acute stretch is no longer beneficial.

Chronic mechanical stretch may also be harmful or maladaptive, leading to stronger, faster, stiffer muscle with an increased ability to shorten. For instance, cyclic stretching of ASM cells on flat, flexible silastic membranes has been shown to lead to increased proliferation and contractile specific protein expression (51). Mechanical strain is also known to be a potent stimulus for cytoskeletal remodeling and stiffening (5, 6, 19, 49, 50). These changes are believed to involve RhoA activation, a key regulator of actin formation and contractile function (49), and are associated with increased force generation, calcium sensitivity (53), velocity of shortening and shortening capacity (52).

Interestingly, the changes in contractile function seem to depend on the strain field; non-uniform, uniaxial stretch leads to pro-contractile changes, whereas uniform, biaxial stretch leads to results consistent with a reduction in contractility (40, 55). Because strain in healthy airways is largely isotropic, increasing similarly in both diameter and length with inspiration (25), stretch would limit contractile function.

Whereas asthmatic airways likely deform anisotropically due to the increase in tone limiting bronchial dilation relative to lengthening (40), and thus, in this situation, stretch would promote increased contractile function.

1.5 3D Cell Culture

In-vivo, many cell types, including ASM, exist within a 3D, complex, dynamic environment, which consists of: (1) an extracellular matrix (ECM) comprised of a scaffold of collagens and other structural proteins that is interlaced with proteoglycans; (2) mechanical stimulation; and (3) soluble signals from neighboring cells. In contrast, most research to date into cellular response has been conducted using static 2D cell cultures grown on either plastic or glass. However, growing cells on an artificial, flat, rigid substrate may lead to a different cellular behavior than *in-vivo* since cells often undergo phenotype regulation according to their environment (16).

In fact, in a recent review, Griffith and Swartz (17) argued that the majority of cells require signals from a 3D environment to form physiologically relevant structures *in-vitro*. Some of the key reasons made in their argument follows: 1) a 3D culture offers another dimension for external mechanical inputs and cell adhesion, which dramatically affects integrin ligation, cell contraction and associated intracellular signaling; 2) within a 3D ECM, externally applied mechanical stress not only directly transmits forces to cells, it changes the relative distances between cells, ECM components and effector molecules, and thus, could alter extracellular gradients, cell-to-cell communication or local concentrations of secreted ligands; 3) a 3D ECM controls the bulk and local mechanical

environment, and thus, determines the mechanical signals transmitted to the cell culture; 4) the ECM contributes to the microenvironment through its own signaling moieties; and 5) through its ability to bind effector proteins, the ECM regulates the local concentration and gradients of many growth factors, cytokines and enzymes. Because of these reasons, 3D quasi-organ *in-vitro* models will likely have an increasingly important role in applications such as screening new drugs for efficacy and safety in humans before clinical trials.

Therefore a few 3D cell culture models have recently begun to be developed. Previous work conducted by my laboratory group has used a *passive* microtissue model for 3D cell culturing, which consists of an array of wells each containing two flexible cantilevers 600μm apart (60, 61). Approximately 100 to 200 cells in a liquid collagen solution are introduced into the wells, and self-assemble around the cantilevers to form a 3D arrangement similar to human tissue. In contrast, the research conducted for this thesis was to adapt this work for an *active* microtissue model in which the cantilevers are both actuators and force sensors.

1.6 Previous Tissue and Cell Stretching Devices

As already discussed, the effects of mechanical strain on ASM have previously been investigated using traditional motion actuators ((i.e. stepper or DC servomotor drives) to stretch ex-vivo tissue strips (14, 32), and a commercially available vacuum system to stretch 2D in-vitro cell cultures grown on a silastic membranes (5, 6, 19, 49, 50, 51). There are advantages and disadvantages to both these methods. Although *ex-vivo*

tissue strips are structurally relevant to an intact lung, they lack the control over environmental and biochemical factors necessary to elucidate responses at the cellular level. Further disadvantages to experimenting on human ASM strips include their limited availability, an inability to conduct chronic experiments, and a markedly lower intrinsic tone than observed *in vitro*. In contrast, 2D *in-vitro* cell cultures offer a highly controllable environment to study cellular and biochemical responses but fail to recapitulate physiological conditions, which are known to affect cellular response.

To fill the gap left by *ex-vivo* tissue strips and 2D in-vitro cell culture, devices capable of stretching 3D cell cultures have recently been developed. In these devices, cells are evenly distributed within a user-designated gel with a tunable stiffness to match *in vitro* conditions while retaining the necessary control over environmental factors to study cellular and biochemical responses. Many of these 3D cell cultures are, however, centimeter scale, which confounds investigations into the rapid dynamics of cellular contractility due to diffusion limited concentration gradients (35). For instance, assuming that diffusion is governed by Fick's second law, the time required for diffusion scales with the thickness of the construct squared; therefore, concentration gradients in microtissues (thickness of 100μm) should equilibrate 100x faster than bulk gels (thickness 1mm). For this reason, a device capable of studying the effects of stretch in micron-scale 3D cell cultures is desirable.

This desire for a small-scale 3D cell culture-stretching device, however, requires a smooth continuous actuation system with a resolution within the nanometer-range. Since piezoelectric actuators are routinely used in fine position control, they may be suitable for stretching cell cultures as well. Indeed, piezoelectric technology has already been used to stretch and measure changes in stiffness in single cells (40). However, their usefulness for

stretching 3D cell cultures has yet to be examined.

1.7 Piezoelectricity

Lead Zirconate Titanate (PZT)

Discovered in 1880 by Pierre and Jacques Curie, the piezoelectric effect is understood to be the linear relationship between mechanical and electrical states in crystalline materials with no inversion symmetry, such as PZT. In other words, materials that display piezoelectricity will internally generate electrical charge resulting from mechanical strain. This is referred to as the direct piezoelectric effect. Since piezoelectricity is a reversible process, materials that exhibit the direct piezoelectric effect will also exhibit the inverse piezoelectric effect, in which internal mechanical strain results from an applied electrical field. This phenomenon is presently used in many applications, such as the production and detection of sound, generation of high voltages, electronic frequency generation, microbalances, and ultrafine focusing of optical assemblies.

PZT is currently a widely used industrial norm. It is a polycrystalline ceramic with a Perovskit structure of ABO_3. Where A, B and O represents a double positive charged ion (lead), a four-fold positive charged ion (titanium, zirconium), and a double negative charged ion (oxygen), respectively. Above the Curie temperature, T_C, PZT crystallites have symmetric cubic elementary cells with no piezoelectricity due to their symmetric center. Falling below the Curie temperature, the lattice structure becomes deformed and

asymmetric, either tetragonal or rhombohedral dependent upon the molecular ratio of titanium to zirconium. At this point, the PZT crystallites exhibit spontaneous polarization; the unit cells are piezoelectric. However, because of the random distribution of the Weiss domains, no macroscopic piezoelectric behavior is observable. Applying a sufficient electric field with a defined direction aligns the domains with the field direction, poling the ceramic. Once the field is removed, remnant polarization allows the ceramic to exhibit piezoelectricity. If the polarization does not become degraded by exceeding the mechanical, thermal and electrical limits of the material, PZT will behave in a predictable manner for the duration of the device's lifespan.

Unimorph Actuators

Because of the relatively small piezoelectric coefficient, the range of travel and force sensitivity of a linear actuator/sensor is often too small to be used in most applications. Instead, a bender configuration, such as a unimorph, can be adopted to amplify the motion and force sensitivity. A unimorph actuator consists of a piezoelectric layer, with its electrodes, bonded to a passive elastic metal layer (Figure 1-1). A bending moment is produced when length changes in the piezoelectric plate, due to the transverse piezoelectric effect, are constrained by the elastic plate. On the other hand, unimorphs can also be used as mechanical sensing elements since the amount of electric charge generated on the electrodes is directly proportional to strain. The generated tip deflection, d, and electrical charge, Q, of a unimorph with a perpendicular tip force, F, can be expressed by the following set of equations (57, 58):

$$d = \alpha F + \beta V_{in} \quad (1)$$

$$Q = \beta F + C_p V_{in} \quad (2)$$

where,

$$\alpha = \frac{4 s_{11}^p s_{11}^m (s_{11}^p t_w + s_{11}^m t_p) L^3}{Kw} \quad (3)$$

$$\beta = \frac{3 d_{31} s_{11}^p s_{11}^m t_m (t_m + t_p) L^2}{K} \quad (4)$$

$$C = \frac{Lw}{t_p}\left(\varepsilon_{33}^x - \frac{d_{31}^2 t_m (s_{11}^m t_p^3 + s_{11}^p t_m^3)}{K}\right) \quad (5)$$

where,

$$K = (s_{11}^m)^2 (t_p)^4 + 4 s_{11}^m s_{11}^p t_m (t_p)^3 + 6 s_{11}^m s_{11}^p (t_m)^2 (t_p)^2 + 4 s_{11}^m s_{11}^p t_p (t_m)^3 + (s_{11}^p)^2 (t_m)^4 \quad (6)$$

$$\varepsilon_{33}^x = \varepsilon_0 \cdot \varepsilon_3^x \quad (7)$$

Using these equations, the cantilever dimensions can be optimized for travel range and force sensitivity.

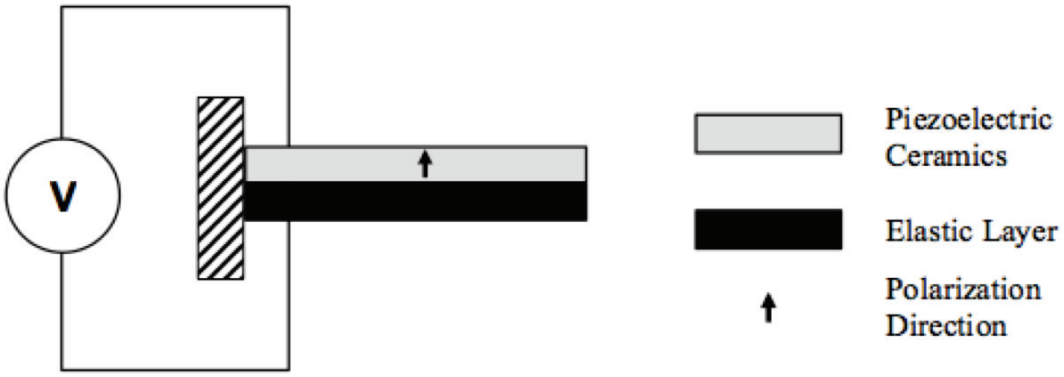

Figure 1-1: The structure of a unimorph actuator.

Bimorph Actuators

In the previous section, unimorph actuators were introduced as a simple method to amplify the range of travel and force sensitivity of piezoelectric actuators. To further

amplify the deflection and improve the sensing capability, bimorph actuators can be used. Bimorphs are structurally similar to unimophs except a second piezoelectric layer replaces the passive elastic layer. The piezoelectric plates in a bimorph operate together so that when one plate expands, the other contracts. The net effect is a bending deflection. The generated tip deflection and electrical charge can be modeled by substituting the following equations into equations (1) and (2) (57, 58):

$$\alpha = \frac{4s_{11}^{p}L^{3}}{wt^{3}} \quad (8)$$

$$\beta = \frac{3d_{31}L^{2}}{2t^{2}} \quad (9)$$

$$C = \frac{\varepsilon_{33}^{x}Lw\left(1-k_{31}^{2}/4\right)}{t} \quad (10)$$

where,

$$k_{31}^{2} = d_{31}^{2}/\varepsilon_{33}^{x}\, s_{11}^{p} \quad (11)$$

Bimorphs can be connected in one of two ways: parallel and series connection (Figure 1-2). In parallel connection, the piezoelectric plates have the same polarization direction but the polarity of the electrical fields in the plates opposes one another. The electrical field strength is the applied voltage divided by half of the total actuator thickness. Whereas in series connection, the piezoelectric plates have opposing polarization direction and the electric field is applied across the entire thickness of the actuator (i.e. the electrical field strength is the applied voltage divided by the total actuator thickness). Thus bimorphs in series connection require twice the driving voltage to achieve the same deflection as bimorphs in parallel connection, making them less desirable as actuators. Instead bimorphs in series connection are widely used as sensors (42) because their capacitance is half of a bimorph in parallel connection, which doubles

the output voltage (i.e. sensitivity) when read directly off the sensor.

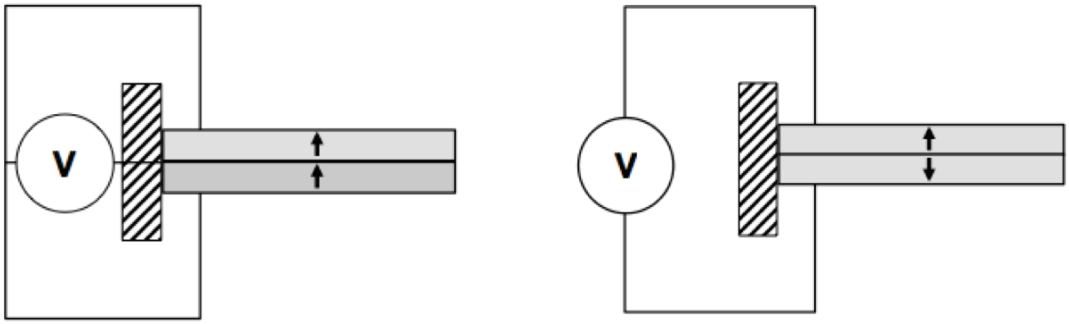

Figure 1-2: The structure of a bimorph actuator in parallel (left) and series (right) connection.

1.8 General Hypothesis

It is my general hypothesis that piezoelectric technology and tissue engineering techniques can be used to develop a device capable of achieving ±5%, chronic, sinusoidal stretch on an array of microtissues within an incubator with live cells while simultaneously measuring changes in tissue mechanical parameters. For practical reasons, the device must not be sensitive to temperature, must be usable for a range of frequencies from 0.1 to 1 Hz, and must possess an uncertainty in motion and force detection of less than 10%. This general hypothesis is addressed by the following set of specific aims.

1.9 Thesis Aims

Aim #1

Design a protocol to fabricate an array of actuator pairs capable of achieving +/-

5% continuous oscillatory stretch of a microtissue at breathing frequency.

Aim #2

As a proof of concept, assess whether live cells can form into 3D microtissues, survive, and produce detectable contractions in the device while being subjected to length oscillations.

Aim #3

In keeping with a previously published self-sensing method, fabricate the necessary electronics to accurately measure the cantilever deflection and changes in tissue force while simultaneously stretching the tissue.

Chapter 2: Piezoelectric Miniature Actuator Array Fabrication and Characterization

2.1 Rationale

The action of breathing makes the airway a mechanically active environment. For instance, if we assume that an airway wall stretches isotropically corresponding to the cube root of lung volume change (25), then a normal tidal lung inflation would be equivalent to roughly 4% strain, a sigh would be equivalent to roughly 12% strain, and an inflation from functional residual capacity to total lung capacity would be equivalent to roughly 25% strain (14).

As described in the introduction, stretch has already been shown to have potent effects on *ASM ex vivo* strips and 2D *in vitro* cell culture. Previous investigations into the effects of oscillatory stretch on 2D cell cultures have shown that a chronic strain of 10% is a sufficient stimulus. Whereas investigations on *ex-vivo* bronchial tissue strips have used an acute strain up to ±4%, although marked differences in muscle active force, stiffness and hysteresivity started to appear when strain was increased from a static condition to beyond ±0.5%. Therefore, the device was intended to achieve a maximal ±5% stretch of the 600μm tissue, since at this amplitude the tissue should elicit a measurable response that directly reflects an intact airway.

In keeping with the microtissue design outlined by Legant *et al.* (35)**,** the device consisted of sets of miniature cantilevers in an array format fixed to a common base. However, instead of *passive* polydimethylsiloxane (PDMS) cantilevers, the cantilevers *actively* stretch the tissue along a single axis. It is important to note that although uniaxial

stretch is not physiological, it has merit when studying asthma because it matches the changes in the strain pattern due to radial stiffening of the airway. Also if desired, the design can be adapted for biaxial stretch at a later time by using four cantilevers per tissue that move along one of two axes.

Larger-scale tissue strip stretching devices have previously been fabricated using *traditional* motion actuators (i.e. stepper or DC servomotor drives) in combination with an external force transducer (14, 37, 39). However, *traditional* technologies suffer from some amount of friction and stiction, which causes uncertainty in position repeatability and limits resolution due to wobble, hysteresis and backlash. For this device, these *traditional* technologies are therefore not suitable. A relatively cheap alternative is piezoelectric actuators, such as unimorphs and bimorphs. Because the movement of a piezoelectric actuator is based on ionic shift, the resolution is theoretically unlimited. However, voltage source noise, even in the μV range, could cause measurable position changes, and thus, a loss in accuracy. Then again, when driven with a low-noise amplifier, piezoelectric actuators are capable of achieving smooth continuous accurate motion with a resolution often in the nanometer or even the subnanometer range, making them perfect for this aim. Shown in Figure 2-1 is the device design with unimorph cantilevers.

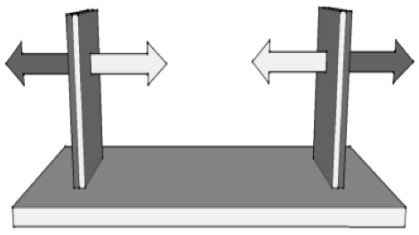

Figure 2-1: **A schematic of the piezoelectric microtissue design. The piezoelectric ceramic is the inner layer, while the elastic metal is the outer layer.**

2.2 Theoretical Design Optimization for Unimorph Actuators

Free Deflection

Since the actuators were spaced apart by 600μm, ±5% stretch corresponds to a 15μm peak deflection when both actuators are in motion. Using the equations (1-6) from the introduction, cantilever dimensions (length, width, elastic layer thickness, and piezoelectric layer thickness) and materials were chosen to achieve this deflection. Shown in Figure 2-2a) and b) are the effects of changing the piezoelectric layer thickness and elastic layer thickness on free deflection, respectively, when operating at the maximally allowed applied voltage (i.e. the coercive field).

In both figures, the curves peak at an optimal piezoelectric/elastic layer thickness ratio. This is clear if we consider the two limiting cases. First, when the elastic layer is too thick and/or the piezoelectric layer is too thin, the bending stiffness is infinite and/or the bending moment is infinitely small. In the second case, when the piezoelectric layer is too thick and/or the elastic layer is too thin, the generated transverse strain in the piezoelectric layer is subjected to an infinitely small constraining force and so the actuator will not bend. It is also shown that the peak shifts to a thinner elastic layer and/or thicker piezoelectric layer when the compliance of the elastic layer decreases. This was especially important to consider when choosing the elastic layer material for my application because of a desired post thickness in accordance with the passive microtissue design and the available thicknesses of elastic layer material.

a)

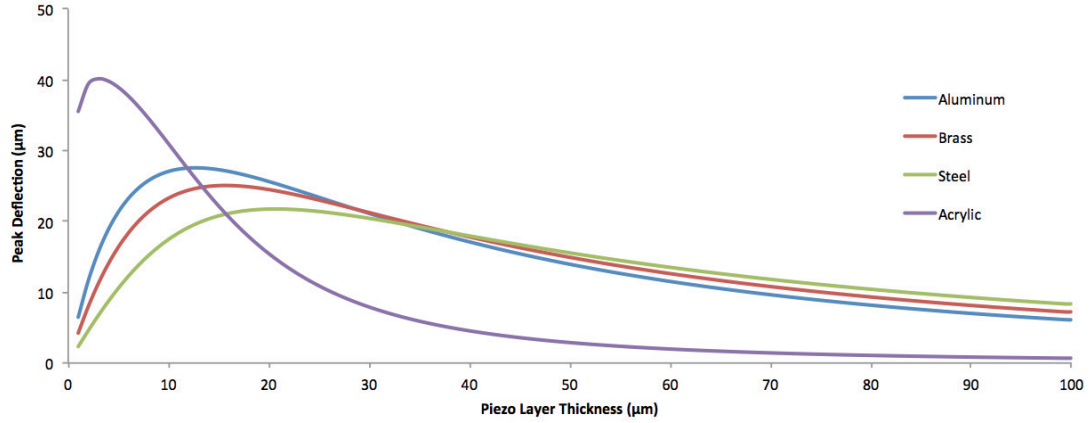

b)

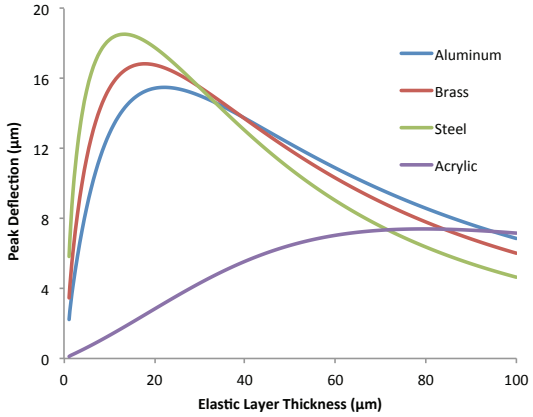

c)

Constant	Value
S_p^{11} (m^2/N)	1.631e-11
S_{al}^{11} (m^2/N)	1.54e-11
S_b^{11} (m^2/N)	9.52e-12
S_s^{11} (m^2/N)	5e-12
S_{ac}^{11} (m^2/N)	3.23e-10
d_{31} (m/V)	-320e-12
E_c (V/m)	0.78e6

Figure 2-2: The theoretical effects on peak deflection, normalized to cantilever length, when varying (a) the piezoelectric layer thickness while the elastic layer was kept constant at 25µm, and (b) the elastic layer thickness while the piezoelectric layer thickness was kept constant at 45µm. In both plots, four different elastic layer materials are shown. Table (c) contains the mechanical and piezoelectric constants used in the model.

Deflection with a Constant Force

When designing the actuators, it was important to consider the forces that must be generated to overcome the tissue elasticity (passive force) and contractility (active force). In the simplest case, a constant force is applied to the actuators; when working against the load, deflection is lost, however, it is regained in the other direction when operating with the load. In other words, the full peak-to-peak deflection is attained, but around a new

offset position determined by the mechanical equilibrium between a static cantilever and the load.

For my application, at small strains, a constant force was likely a reasonable approximation because the passive force should be relatively small, as it is in the "toe region" of the nonlinear tissue length-tension curve, compared to the active force, which in similar sized maximally contracted ASM microtissues has been found to be roughly 20μN (60). It is also important to note that a muscle's *active* force depends on its length. However, small fluctuations in strain around the ideal length, often the resting length, will have little effect on contractility because the relationship between length and force is parabolic in shape (43, 56). The effects of changing the piezoelectric and elastic layer thicknesses have upon the offset position are shown in Figure 2-3a) and b). To produce a measurable offset in order to calculate contractile force, thinner piezoelectric and elastic layers are favoured.

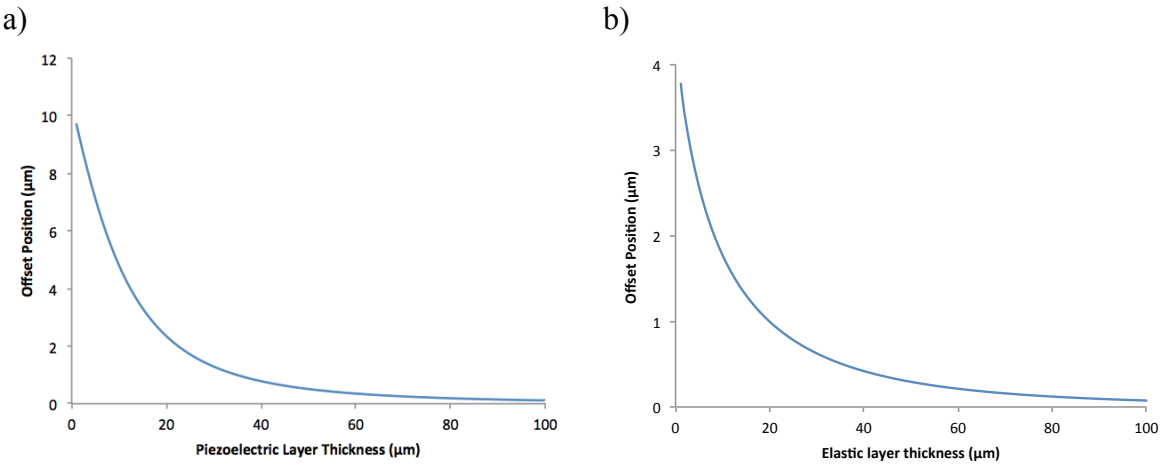

Figure 2-3: The theoretical effects on offset position with a constant tip force of 20μN applied to an actuator with a width of 200μm, and length of 2.5mm when varying (a) the piezoelectric layer thickness while the brass elastic layer was kept constant at 25μm, and (b) the brass elastic layer thickness while the piezoelectric layer was kept constant at 40μm.

Deflection with an Elastic Force

At larger strains, where the passive force is in its "linear region", the tissue elasticity becomes much more important, and thus, the tissue force is no longer constant. A previous study using passive cantilevers estimated the elastic modulus of similar microtissues formed with fibroblasts in a collagen matrix to be roughly 25kPa (35). Assuming that the tissue stretches perfectly elastically and homogeneously, the elastic force can be expressed as:

$$F = -S_t d = -\frac{E_t A_t}{l_o} d \quad (12)$$

This expression can be subbed into equation (1) and then simplified to give:

$$d = \frac{\beta V}{1 + \alpha \left(\frac{E_t A_t}{l_o}\right)} \quad (13)$$

With the assumption that the tissue's resting length (i.e. the length where there is no elastic force) is 600μm and thickness is 100μm, the effects of changing the piezoelectric and elastic layer thicknesses, and actuator length on deflection when oscillating against an elastic tissue are shown in Figure 2-4a), b), and c). These figures reveal that peak deflection is decreased when stretching an elastic tissue because the electrical potential energy supplied to the actuator is being converted into elastic potential energy both through the bending of the cantilever, and as well as, through the stretching of the tissue. This does, however, provide a method for the device to track changes in tissue stiffness by measuring its impact on the peak deflection of the actuators. Furthermore, according to these figures, the sensitivity of an actuator to the tissue's elasticity can be increased by scaling the actuator's dimensions to a smaller stiffness (i.e. decreased thickness or increased length).

a)

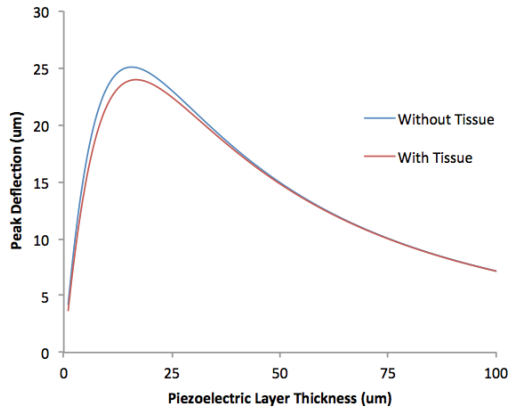

b)

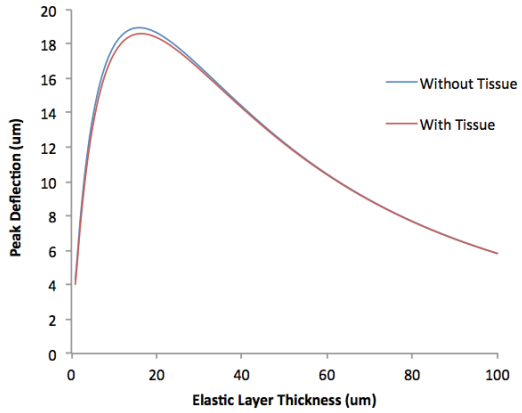

c)

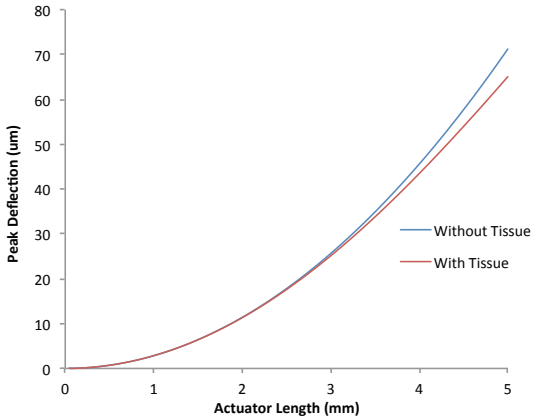

d)

Constant	Value used in the model
Elastic Modulus, E_t (Pa)	25 000
Width (m)	200e-6
Thickness (m)	100e-6
Initial Length, l_o (m)	600e-6

Figure 2-4: The theoretical effects on peak deflection when stretching an elastic tissue at the tip of the actuators with varying (a) the piezoelectric layer thickness while the elastic layer and actuator length were kept constant at 25µm and 2.5mm, respectively, (b) the elastic layer thickness while the piezoelectric layer and actuator length were kept constant at 40µm and 2.5mm, respectively, and (c) the actuator length while the elastic layer and piezoelectric layer were kept constant at 25µm and 40µm, respectively. Table (d) contains the constants used to model the tissue.

2.3 The First Approach

2.3.1 Methods (the first approach)

Device Fabrication

In the first approach, I attempted to fabricate the device out of a single block of piezoelectric material (5mmx 5mmx 2mm; lxwxt) (EBL Products, EBL #3, East Hartford,

CT) with several simple steps:

1) Two cuts perpendicular to the poling direction were made with the dicing saw (DISCO, DAD3220, Tokyo, Japan) using a fine grit diamond blade (DISCO, B1A801 SD400N50M51, Tokyo, Japan). The depth of the cuts was dependent on the desired length of the miniature cantilevers, and the space between the cuts was dependent on the desired separation of the miniature cantilevers. To achieve the desired deflection, preliminary designs used a depth of 2.5 mm, and to be consistent with previous microtissue arrays, a separation of 600μm measured from the inner most edges.

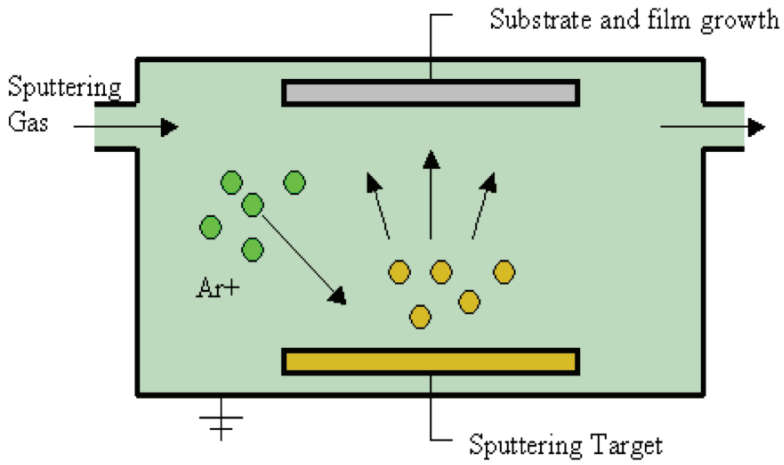

Figure 2-5: An illustration of the sputtering process. An RF field ionizes argon gas to form plasma. Due to the polarization of the electrical field, the ions are accelerated and collide with the sputtering target. These collisions knock off atoms from the sputtering target that flow towards the sample and deposit on its surface.

2) A thin layer (< 1μm) of aluminum was sputtered (Material Research Corporation, 8667-8671, Orangeburg, NY) onto the device to form the outer electrodes. Sputtering is a very common method used to deposited thin films. A diagram illustrating the process is shown in Figure 2-5. All sputtering was conducted at a pressure of 10mtorr. For the samples that were etched prior to sputtering, a pressure

of 15mtorr was used. Before loading the samples into the machine they were cleaned with methanol and compressed air.

3) For preliminary work, 25μm thick brass shims (9011K1, McMaster-Carr, Los Angeles, CA) were used as the elastic layers. They were cut out with the dicing saw to match the dimensions of the inside surfaces of the cuts made in step 1). The elastic layers were then epoxied (301, Epotek, Billerica, MA) flush to the cut surfaces and clamped into place over night for the epoxy to cure. It is important to note that for the equations to hold, this bonding layer must be flawless and of negligible thickness.

4) The device was encased in cyanoacrylate glue (Hot Stuff, Lee Valley, Ottawa, ON) to supply the necessary structural support for the steps that follow. The glue was removed once all the cuts were made by placing the sample in a cyanoacrylate-releasing agent (Super Solvent, Lee Valley, Ottawa, ON) for several hours.

5) A third cut was made parallel to, and between, the cuts outlined in the first step keeping in mind the desired piezoelectric layer thickness. At this point, the device resembled two large unimorphs fixed to a common base.

6) The device was sputtered with aluminum for a second time to form the inner electrodes, and the excess aluminum connecting the outer and inner electrodes was removed by sanding with fine-grit sand paper so that an electrical field could be formed across the piezoelectric layer.

7) A number of cuts were made in the poling direction (i.e. perpendicular to the other cuts) to divide the two large unimorphs into several sets of smaller miniature cantilevers.

8) Micro-coaxial cables were attached to the inner and both the outer electrodes with conductive epoxy (EE129-4, Epotek, Billerica, MA).

Experimental Methods for Tracking Deflection

A photograph and a flow diagram of the experimental setup are shown in Figure 2-6a) and b), respectively. The deflection of the posts was captured by a 15 frame per second (fps) firewire camera (MC-F433C, 1st Vision, Andover, MA) with a resolution of 640x480. The camera was firmly fixed above the sample to one of the two arms of the micromanipulator (MLW-3 three axis water hydraulic, Narishige, Tokyo, Japan). The fine control of the micromanipulator has a resolution of 0.04μm, which allowed the camera to focus at the top of the actuators. A 40x microscope objective was used in front of the camera to magnify the image. Measuring the pixel distance between lines on an image of a hemocytometer taken with this setup gave a sensitivity of 1.037μm/pixel. All the measurements were done on a vibration isolation table (VH Isolation, Newport, Irvine, CA) to prevent any spurious deflection artifacts. The camera feed was acquired and analyzed in real-time in a LabVIEW program that designed was to track the motion of the actuators. The validation for that program is discussed in the following chapter.

A function generator (FG-7002C, EZ Digital, Melrose, MA) with a 20X voltage amplifier (A-301, AA Lab Systems, Ramat-Gan, Israel) was used to drive the actuators at the tested frequencies and voltages. The voltage from the function generator was recorded via a 16-bit data acquisition card (NI-6035E, National Instruments, Austin, TX) at 1000Hz and then averaged to 15Hz to match the speed of the camera. The function generator was later replaced with the digital to analog convertor on the NI-6035E card to

have greater control over the signal used to drive the actuators.

a)

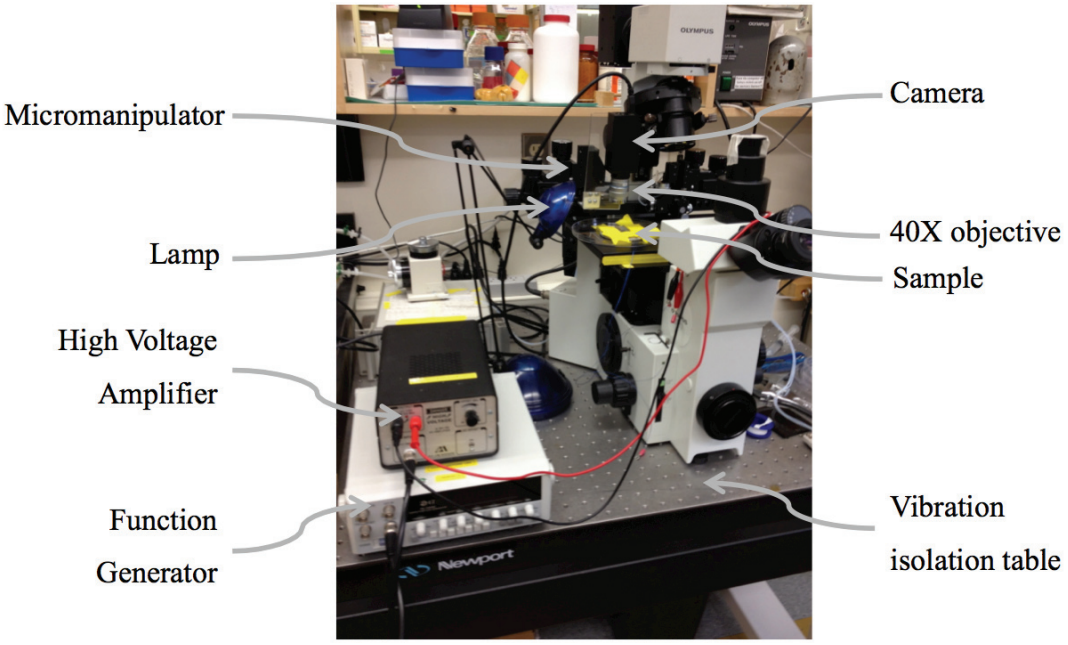

b)

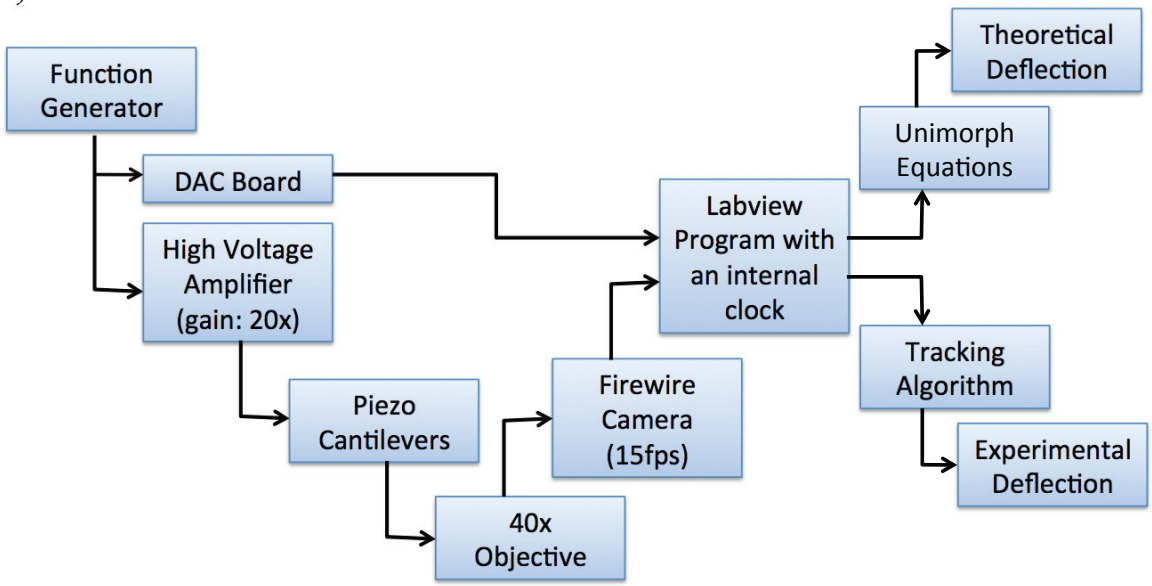

Figure 2-6: (a) A photograph and (b) a flow diagram of the experimental set-up used to track the free actuator deflection. The actuators were driven with a high voltage function, and the resulting tip deflection was captured by a camera mount to a micromanipulator above the sample. The video feed was then analyzed in Labview in real-time to determine tip position.

2.3.2 Results (the first approach)

Device Fabrication

Several changes to the protocol were made; mainly experimenting with different post dimensions, sputtering times, and epoxy types. Other changes include: 1) the vice used to clamp the elastic layer while the epoxy was curing was switched to a higher quality machining vice that had a more even force distribution so the bonding layer would be uniform; 2) the elastic layer was extended beyond the base of the actuators to provide additional support; 3) the cyanoacrylate glue was removed prior to sputtering so it did not off-gas and contaminate the electrodes; and 4) the gap between the actuators was filled with cyanoacrylate glue for support during the final dicing step. Despite these efforts, three main problems persisted: 1) dicing the actuators without causing the piezoelectric layer to crack; 2) delamination between the piezoelectric and elastic layers; and 3) sputtering on a conductive inner electrode with complete coverage. Photographs taken of the actuators are shown in Figure 2-7a) and b). These problems and experiments conducted to address them are briefly outlined in the individual sections that follow.

a) b)

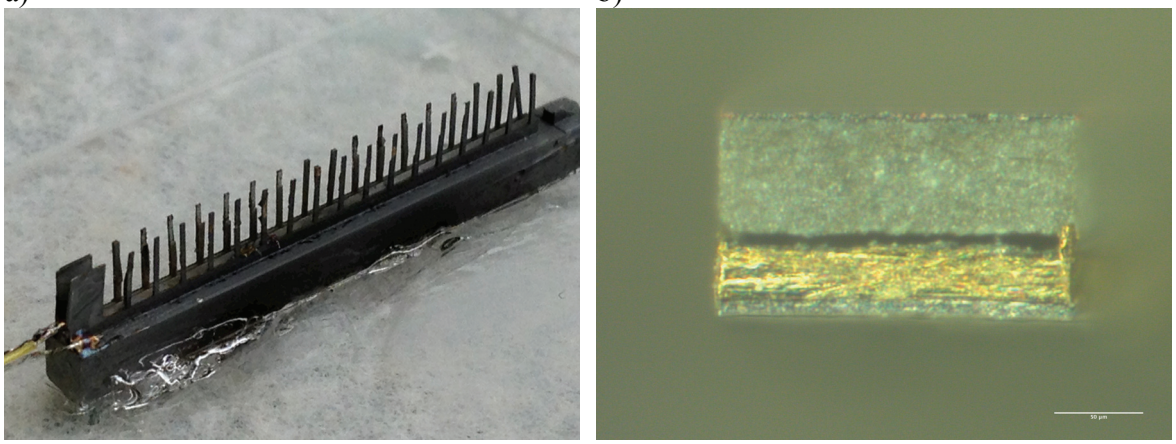

Figure 2-7: Photographs taken of the device fabricated with the first approach. Panel (a) is a macroscopic view of the array of actuators. Panel (b) is a microscope view of the tip of an actuator.

1. Dicing the actuators without causing the piezoelectric layer to crack

From examining several samples under an optical microscope it was clear that nearly all, if not all, the actuators had cracks in their piezoelectric layer. The potential impact this problem might have had on the movement of the posts is related to the size of the cracks. Small cracks might have had no impact, whereas large cracks are locations for stress relief and loss of conductivity, and thus may have prevented the actuators from moving. Because of this potential downfall, I investigated whether changing the cantilever stiffness, mainly the width and thickness, as well as the stresses produced from dicing, mainly the feed speed, would affect crack formation.

Samples of piezoelectric material were diced as outlined in steps 1-5 in the protocol above. But because sputtering and epoxying on an elastic layer would have made it difficult to visualize the cracks, these steps were omitted. The samples were diced to 25, 35 and 45μm thicknesses with either a 2mm/sec or 0.5mm/sec feed speed. The depth of the cuts was 3mm on the outer side and 2.5mm on the inner side of the posts and the revolution speed of the blade was 30000rpm. In general, it was found that decreasing the feed speed, and increasing the PZT thickness both reduced the appearance of cracks, and that a thickness of 45μm was the thinnest the actuators could be made reliably.

45, 60, and 90μm thick actuators were then diced as in step 7 to different widths (100, 200, 400, 800μm). The feed speed was 0.5mm/sec, the revolution speed was 30000rpm and the depth of cut was 2.5mm. The same blade was used as above. However, every width and thickness combination tested cracked during dicing. These results indicate that the majority of cracks in preliminary attempts to fabricate the actuators were caused by exposing the thin, high aspect ratio cantilevers to high shear, vibrational, and/or torsional stresses when the samples were cut into individual actuators.

2. Delamination of the piezoelectric and elastic layers

The preliminary attempts at fabricating the actuators all had a sizeable gap between the piezoelectric and elastic layers. This gap would likely dramatically decrease actuator deflection for several reasons. First, because the compliance of the epoxy is much higher than the elastic layer, a thick epoxy layer would act as a buffer, decreasing the ability of the elastic layer to constrain the transverse strain in the piezoelectric layer. Secondly, the epoxy layer was likely very heterogeneous; in some places the layer was very thick, and in others, there was no epoxy at all. Lastly, a thick epoxy layer increases the bending stiffness of the cantilever by increasing the moment of inertia.

By visual inspection, the mechanism of delamination seemed to be an interfacial failure with the bond between the epoxy and the brass shim as the weak link. To improve the adhesion to the brass I tried making the posts with using two other epoxies (Loctite M-31CL, Ellsworth, Germantown, WI; and 105/205, West System, Bay City, MI). These epoxies vary in their chemistries, viscosities and shear strengths, and so they may have had better bonding strength to brass than Epotek 301. Elevating the curing temperature to 60^{o}C was also evaluated with using Epotek 301 as this has been shown to be effective to increase the bonding strength and chemical resistance in other epoxies through increases in cross-linking (45). Abrading the elastic layer to create a mechanical interlock to increase the bond strength was also evaluated again with Epotek 301. Unfortunately none of these changes improved the appearance of the posts.

After examining samples before and after sputtering it was clear that the gap between the layers was formed during the sputtering process. It is believed that the high temperature from long sputtering times, which can be in excess of 200^{o}C, exceeded the glass transition temperature of the epoxy, causing the epoxy to pass into a rubbery state

and redistribute unevenly between the two layers. Long periods of high-sustained heat also likely had effects on the adhesive properties of the epoxy, as the layers were easily separable at that point.

Alternatives to the elastic layer

In an attempt to avoid the problems encountered with epoxying the layers together, several different approaches were investigated. These are discussed briefly in individual sections that follow. For various reasons none of these alternative approaches improved the fabrication process.

2.1 Sputtering on the elastic layer

After step 1, the sample was laid flat and sputtered at 500W for 15x10-minute intervals with 5-minute breaks in between and a prior 30-second etch. The 30-second etch is meant to clean the surface from debris. The thickness of the sputtered aluminum layer was measured from a calibrated image to be 20.6μm. The sample was then flipped and sputtered on the other side with the same settings. The sample was then encased in cyanoacrylate glue for the subsequent dicing steps. However while the glue was curing, the aluminum layer delaminated. Delamination of thick films produced by sputtering is a common problem; because thicker films are inherently stiffer, the residual stresses between the substrate and the film formed during the disposition process are higher, and therefore they are more prone to delamination.

2.2 Inside-out posts

The protocol was altered so that a sample could be fully sputtered before epoxying

on the elastic layer. The space between the posts was cut out first, sputtered and filled with cyanoacrylate glue. The sample was then diced again to the desired piezoelectric layer thickness and sputtered again. Finally, the elastic layer was epoxied on. This change to the protocol prevented delamination however the other problems still existed.

2.3 Solder as a bonding agent rather than epoxy

After step 1, the sample was evaporated with a thin layer of gold (75nm)-chrome (4nm). Strips of brass were coated with low temperature solder paste (SMDLTLFP-ND, Digi-Key, Thief River Falls, MN). The solder-coated brass and gold-coated piezoelectric ceramic were clamped together and heated so the solder would reflow, creating a joint between them. Unfortunately in many places the thin gold layer completely solubilized, and the few places where a joint was made, the solder had a thickness of upwards of 20μm, which would noticeably decrease the actuator deflection.

2.4 Solder as the elastic layer

After step 1, the sample was evaporated with a thin layer of gold-chrome as above. The low temperature solder was then applied to the cut surfaces in place of brass for the elastic layer. The sample was heated past the melting point of the solder. The solder would have then been thinned to the desired thickness with the dicing saw, but as above, the gold solubilized so a joint was not made.

2.5 RAINBOW actuators

To prevent problems with delamination, Haertling (21) developed a technique to fabricate monolithic piezoelectric bending actuators called reduced and internally biased

oxide wafer (RAINBOW) devices. Basically the RAINBOW device is a unimorph bender**,** consisting of a piezoelectric active layer and a chemically reduced nonpiezoelectric inactive layer with a sharp interface between them. The inactive layer is selectively reduced by a chemical redox reaction with graphite driven by high temperature, and for PZT-5H based RAINBOW actuators, the rate of reduction follows a simple parabolic law, allowing for control over the reduced layer thickness.

For my purpose, samples (5mmx5mmx2mm) were heated to 1085^{o}C for 1.25hr with a block of graphite (GT001125, The Graphite Store, Buffalo Grove, IL) on either side to reduce both outer surfaces to a non-piezoelectric layer while leaving a piezoelectric layer in between. This gave a reduced layer thickness of approximately 800μm with a measured rate of 716μm/hour$^{1/2}$. This rate is much higher than a previously published result of 293μm/hour$^{1/2}$ (59) likely because of an open microstructure consistent with poorly sintered PZT. The edges were then diced off because of an uneven reaction rate caused by exposure to atmospheric oxygen. However because of residual stresses formed during cooling due to differences in thermal expansion coefficients, the sample cracked upon dicing. Also the rate of reduction was not uniform along the sample, again likely due to the open microstructure of the sample. Both these factors made this alternative approach unsuitable.

3. Sputtering conductive electrodes with complete coverage

Several different sputtering times and settings were tested for both the inner and outer electrodes. In preliminary work, it was found that the sample had to be sputtered twice to form an outer electrode with low resistance (i.e. the sample was laid on its side, sputtered, flipped, and sputtered again). Etching the sample prior to sputtering was also

found to be very important to prevent the electrode from delaminating. With these considerations in mind, a high-quality, low resistance outer electrode could be sputtered with little difficulty. Shown in Figure 2-8 is a graphical representation of how changing sputtering power and sputtering time affected the electrical resistance of an electrode sputtered on a flat sample.

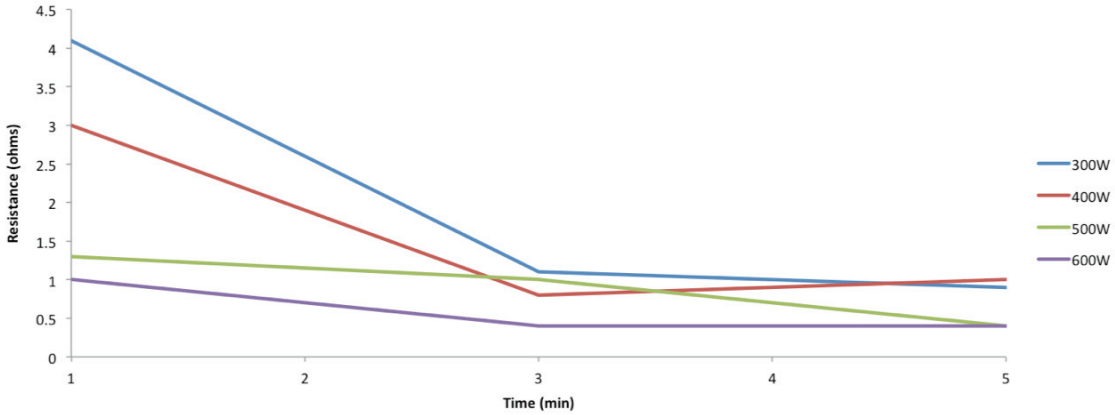

Figure 2-8: The effects of sputtering time and sputtering power on electrode resistance for flat samples.

Unfortunately it was a completely different story for the inner electrode. A lot of the time, the sample was not clean enough from dust or residual cyanoacrylate glue contaminated the sputtered electrode. Furthermore, the inner electrodes were uneven; sputtering left a thick layer at the top of the posts and a thin layer, if at all, at the bottom. To get a more even coating on sides of the actuators, I tried tilting the sample by 10^{o}, sputtering for 3x5min at 500W, tilting the sample the other way by 10^{o}, and resputtering at the same setting. The advantages of this change to the protocol were marginal at best as it still left an uneven electrode. It was also possible to space the actuators further apart so to lessen the aspect ratio. However, I did not see this as a suitable option because I wanted to stay consistent with the tissue length of the present microtissue design, and also by

spacing the actuators further apart, they would need to deflect more to generate the same amount of strain in the tissue.

Deflection Data

Despite these problems, I managed to get a single actuator to work. Shown in Figure 2-9 is the deflection data in the time domain from the only working actuator being driven with a ±20V square wave. The dimensions of the unimorph used for the theoretical data were measured from a calibrated image. Before I could get any data at different voltages or frequencies, the actuator unfortunately broke, likely because of high shear stresses from being driven by a square wave. However, from this data, the experimental deflection matched well with the theoretical prediction. It also revealed that either the electrodes had a considerable amount of resistance, the actuator was affected by mechanical creep, and/or it took several seconds for all the energy consumed by the high frequency event to be regained as elastic potential energy.

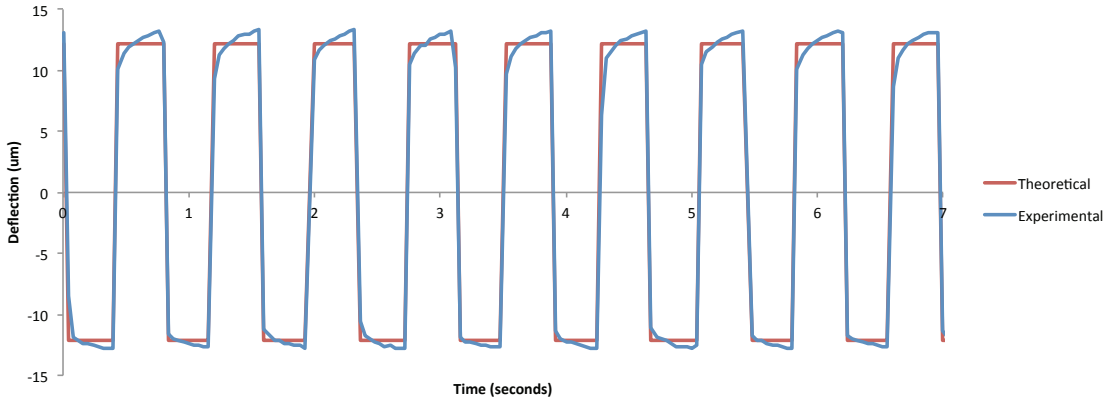

Figure 2-9: Deflection data of a unimorph actuator (2.5mmx200µmx25µmx35µm; lxwxt_mxt_p) driven by a +/-20V, 1.38Hz square wave.

2.3.5 Discussion (the first approach)

The main finding from this portion of my thesis was that functioning miniature piezoelectric actuators could be fabricated. However, due to the major problems identified with this protocol, other methods of fabricating the actuators were required.

2.3 The Second Approach

2.4.1 Methods (the second approach)

Device Fabrication

Because of all the difficulties identified with the first approach used to fabricate the device, a new protocol was designed to avoid the downfalls of the previous. The steps are briefly outlined below:

1) A flat plate of piezoelectric ceramic (PSI-5H 4E, Piezo Systems INC., Woburn, MA) with the manufacture's electrodes was epoxied to a thin brass shim. As with the previous protocol, it was critical that the epoxy layer was even and a negligible thickness.
2) The piezoelectric layer was lapped to the desired layer thickness.
3) An electrode was sputtered using a low temperature setting. A setting of 5x 1-minute intervals at 500W with 5-minutes breaks produced a low resistance (<0.5 Ω) electrode while keeping the sample below 71^{o}C.

4) The edges of the sample were diced away so that there was no electrical connection between the electrodes, and the sample was diced in half so to produce two identical unimorphs.
5) The two identical unimorphs were epoxied to a common conductive base to space the unimorphs apart by the desired tissue length.
6) The sample was encased in cyanoacrylate glue and diced into individual posts.
7) A micro-coaxial cable was attached using conductive epoxy to the common base and the outer electrodes.

Data Analysis for Deflection Results

The posts were tracked with the same setup as in the first approach for 60 seconds. The data was then analyzed in the frequency domain to find the amplitude of deflection. Errors bars on all graphs are the standard error.

2.4.2 Results (the second approach)

Device Fabrication

The second approach avoided many of the problems of the previous. Since the posts were fabricated independently of the base, the middle electrode could be sputtered with the sample laying flat to get an even covering, while using a low temperature setting to prevent delamination. Furthermore because the sample was lapped to thickness instead of diced, thinner actuators could be made without the actuators cracking. Using higher

quality PZT also prevented the posts from cracking during the final dicing step. Photographs of the actuators fabricated with this approach are shown in Figure 2-10a) and b).

a) b)

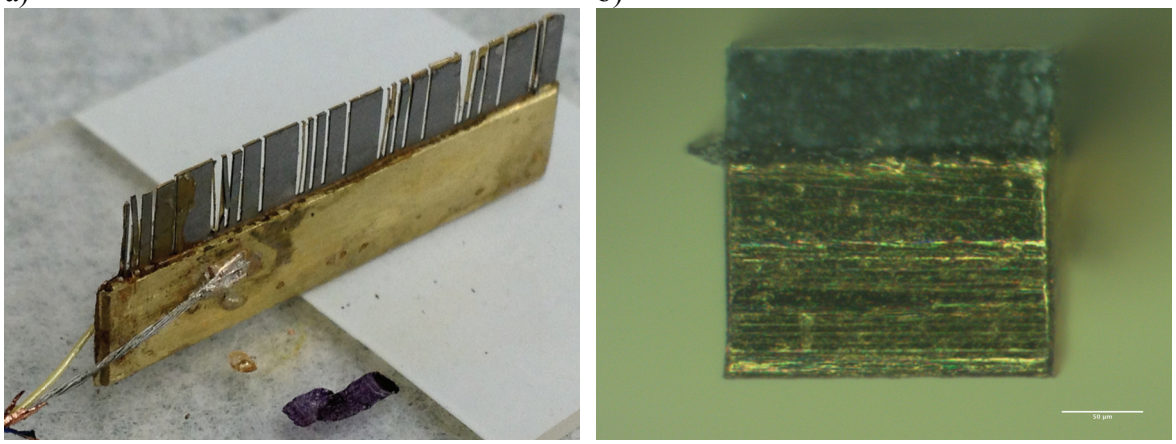

Figure 2-10: Photographs taken of the device fabricated with the second approach. Panel (a) is a macroscopic view of the array of actuators. Panel (b) is a microscope view of the tip of an actuator.

Alternative approaches to the new protocol

Although I had success with fabricating functioning actuators with this protocol, which is demonstrated further on in this chapter, I did investigate a few alternative protocols. These are briefly described in the sections that follow.

1. Lapping and sputtering before epoxying on the elastic layer

Because I did not want to risk exceeding the glass transition temperature of the epoxy during sputtering, samples were lapped and sputtered before the elastic layer was epoxied on. However, the samples were too thin to handle without breaking and so it was decided that epoxying on the elastic layer should be done before lapping.

2. Cutting the individual actuators flat

Once steps 1-4 had been completed, instead of assembling the sample and standing it upright to cut the individual sets of actuators, I first tried to dice out the actuators with the sample lying flat because it was thought that the actuators would be less likely to break with this method. However, the relatively large radius blade used by the dicing saw left a track a few millimeters long beyond the desired length of the actuator. Also the brass was not cleanly cut near the base of the actuators because the blade was not cutting deep enough at that point. For these reasons, and since the actuators did not crack when diced in the alternate upright orientation, this approach was not of any benefit.

3. Solder as the elastic layer

As with the first approach, I tried to fabricate actuators using solder as the elastic layer but instead of evaporating a thin layer of gold, I used samples with thicker gold electrodes created by the manufacturer. The sample was heated to 170^{o}C and low temperature solder was applied. Unfortunately, when solder enters its molten phase its surface tension increases, which caused the solder to bead up on the surface of the sample instead of spreading. In an attempt to prevent this from occurring, I tried using leaded solder (SMD4300AX10, Digi-Key, Thief River Falls, MN), which had a marginal improvement, and solder flux (WS78090, Fastenal, Winona, MN), which only helped for a short period of time (a few seconds). The solubility of the gold coating in the solder was still problematic.

Despite these problems, one sample did get coated well enough to be made into actuators. It was milled flat, lapped to the desired elastic and piezoelectric layer

thicknesses and sputtered. However, after lapping, the sample curled because of residual stress formed during cooling due to the differences in the thermal expansion coefficients of the layers. Also the solder slightly reflowed during sputtering because of the high temperatures. Nevertheless, the sample was diced into 200um wide actuators but they were too brittle and broke during dicing.

Deflection Data

The first successful sample using the new protocol was cut into several actuators (3.25mmx 50μm x 48μm; lxt_mxt_p) of different widths (100, 200, 400 and 800μm). All the 100μm wide actuators broke during dicing and as well as some of the 200μm wide posts. Shown in Figure 2-11a) is example deflection data of a 400μm post driven by a 30V sine wave at 0.33Hz expressed in the time domain. The relationships between post width and deflection, and frequency and deflection are examined in Figure 2-11b) and c), respectively. A two-way ANOVA could not be performed because the majority of the actuators did not work. However, simply by examining the data collected, there did not seem to be an observable correlation between post widths and deflection, and as well as frequency and deflection, except for maybe at higher voltages, the deflection was greater at a lower frequency. Because there did not seem to be any relationships between frequency or width and deflection, all the data was combined into a single deflection vs. voltage plot (Figure 2-11d). This graph reveals a linear relationship between deflection and voltage with a slope nearly identical (0.55μm/V vs. 0.50μm/V) to the theoretical prediction but offset by only a few microns (13.11μm vs. 14.85μm at 30V).

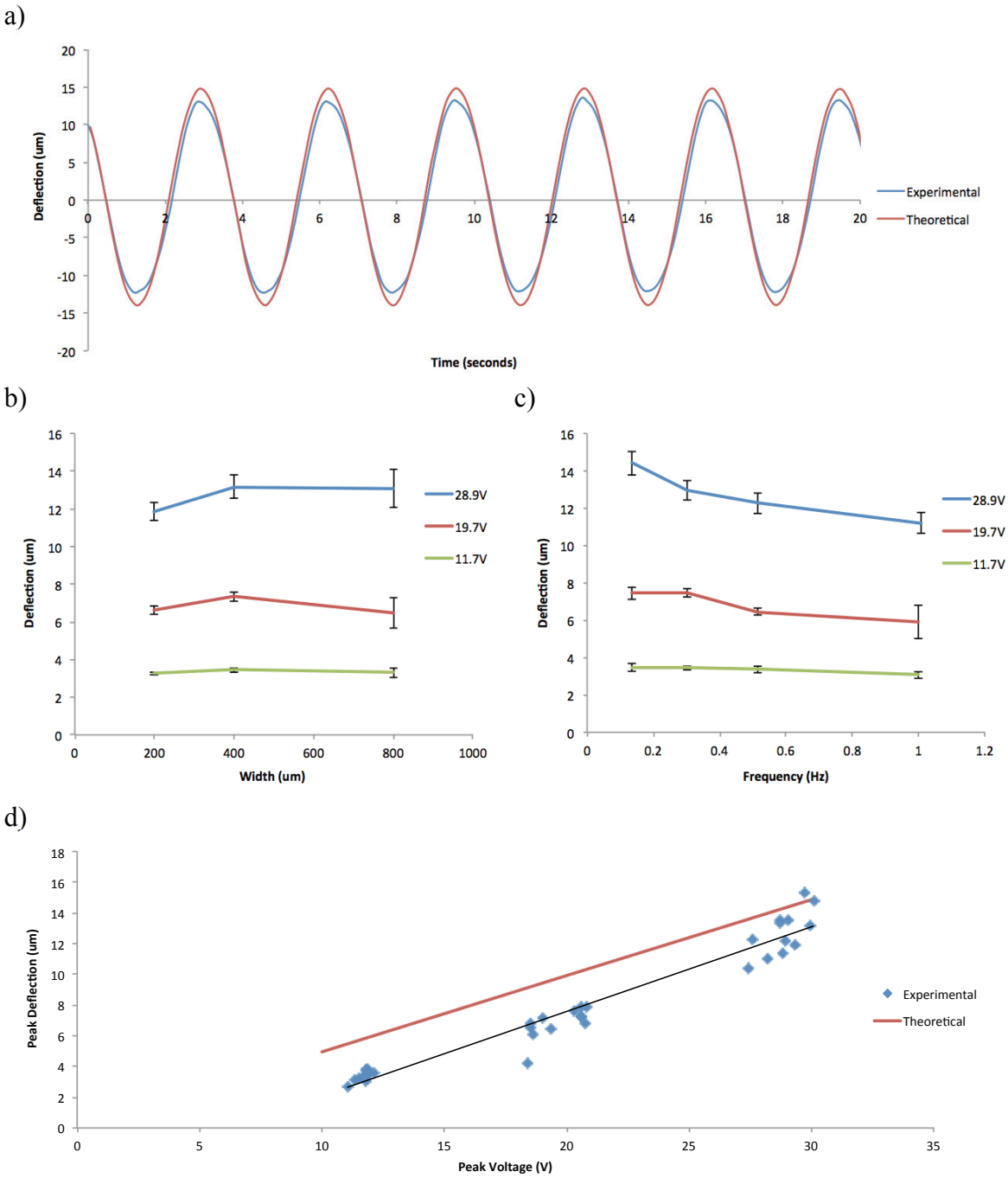

Figure 2-11 (a) Example deflection data in the time domain of a unimorph actuator (3.25mmx50µmx48µm; lxt_mxt_p) being driven by a 0.33Hz, 30V sine-wave. Peak deflection was calculated by solving for the amplitude at 0.33Hz of the Fourier transform. The relationships between (b) post width and deflection (n=3), and (c) frequency and deflection (n=4). Since there were no observable correlations, all the data was combined into a (c) deflection-voltage plot.

Since 400µm wide actuators had nearly the same deflection as the others (200 and 800µm) and they seemed to be as small as I was able to make the actuators reliably, for

the next sample I decided to make all my actuators 400µm wide. In this sample, I investigated how consistently identical posts could be manufactured. Shown in Figure 2-12 is the average voltage-deflection relationship for several actuators (3.5mmx400umx25umx40um; lxwxt_mxt_p) operating at 0.3Hz. Again the slope of the voltage-deflection relationship nearly matched (0.81µm/V vs. 1.12µm/V) the theoretical prediction but was offset by a number of microns (32.75µm ± 3.29µm vs 47.54µm at 42.3V). This data does show, however, that ±5% tissue stretch (i.e. 15µm peak deflection) can certainly be attained with this method.

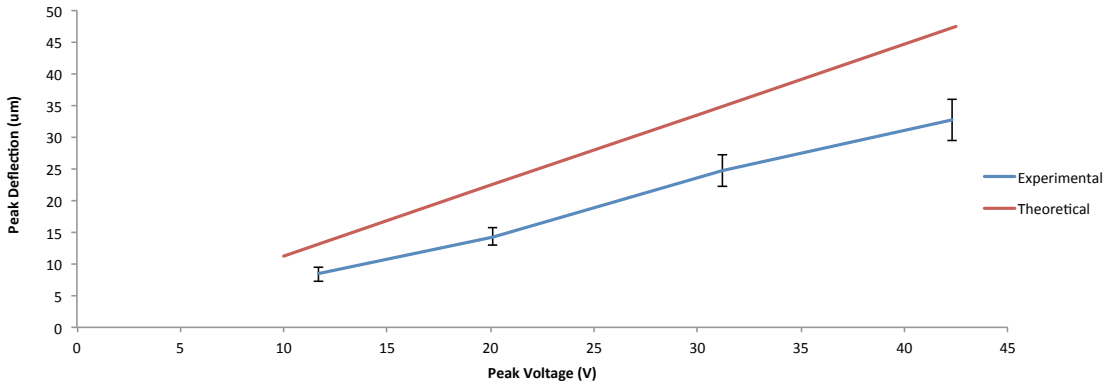

Figure 2-12: The relationship between peak deflection and applied voltage for a set of identical unimorphs (3.5mmx400µmx25µmx40µm; lxwxt_mxt_p) (n=14). Note the large standard error at each voltage.

2.4.3 Discussion (the second approach)

The main finding from this portion of my thesis was that this approach of assembling unimorphs and then securing them to a base was a great improvement compared to the first approach and it could be used to produce an array of miniature actuators that were able to achieve the desired ±15µm deflection.

The actuator deflection had a nearly linear voltage response, albeit a few microns

less than the theoretical prediction. There are a number of possible reasons as to why the post deflection did not match the theoretical prediction, which include: 1) a drop in voltage due to resistance at the electrodes; 2) the thickness of the epoxy layer may not have been negligible; 3) stiffer than theoretical brass or piezoelectric layers. These possibilities were not further investigated as this thesis was meant to be a proof of concept that an array of miniature piezoelectric actuators, with dimensions near the cellular level, could be fabricated by this technique.

In addition to measuring the voltage-deflection relationship, I investigated the effects of actuator width and operational frequency on the measured peak deflection. It was expected that posts with very large widths would deflect less because of an increased lateral bending mode, which would promote warping of the actuator rather than longitudinal bending. It was also expected that as the frequency of oscillation increased, the peak deflection would decrease because of greater air damping at higher velocities. Furthermore, since air resistance is proportional to surface area, wider posts should have been more affected by the dissipation of air, leading to decreased deflection at higher frequencies. However, none of these relationships were found, likely because none of these effects were significant within the small ranges of tested widths and frequencies. Nevertheless, it was found that a width of 400μm was the smallest the actuators could be fabricated reliably, and at breathing frequency, 0.3Hz, the actuators deflected in a smooth continuous motion that could be tracked with the video-tracking method.

In the following sample, I assessed the variability in the peak deflection among actuators fabricated with identical dimensions (3.5mmx400umx25umx40μm; $lxwxt_mxt_p$). For practicality the variability needs to be low so that all the tissues receive the same magnitude of stretch. The large standard error in Figure 2-12 indicates, however, there

was a considerable amount of variability between actuators in this sample. Variability can arise from inhomogeneity in the brass, piezoelectric and/or epoxy layers. Limiting this variability should be a major consideration for future work.

It is also important to note that for the last data point in Figure 2-12, the applied field (1.06V/μm) exceeded the coercive field (0.78V/μm) given by the manufacturer yet the motion of the actuator did not seem to be affected. Because the movement of the actuators remained perfectly sinusoidal, there was likely no change in the polarization direction by exceeding the coercive field for this short period of time. Another possibility worth mentioning is that the resistance at the electrodes may have caused a significant drop in voltage and so the coercive field was not actually exceeded. As discussed above, this theory would also explain why the experimental deflection was less than the theoretical prediction.

Taken together, these findings have shown that an array of miniature unimorph actuators can be successfully fabricated with this approach. However, the large actuator length was worrisome. In the passive microtissue model, the cantilever length is only 200μm whereas the actuators in Figure 2-12 had a length of 3.5mm. At this point in my thesis, I did not know how the greater length would impact tissue formation but highly suspected that shorter actuators were needed for the tissues to compact solely at the top of the device. For this reason, a third approach was investigated, which used bimorph actuators instead of unimorphs to generate greater deflection with a shorter length.

2.5 The Third Approach

2.5.1 Theoretical Design Optimization for a Bimorph

Free Actuation, a Constant Force, an Elastic Force

As with the unimorphs, the dimensions (thickness and length) of a bimorph can be chosen to generate a desired deflection. When there is no external load or the external load is constant, thinner (and longer) actuators are desired, as they will generate greater peak deflection. Moreover, when a constant tip force is applied, thinner (and longer) actuators have a greater offset position, as shown in Figure 2-13a), which would allow easier measurements of tissue contractility.

As for an elastic force, Equation 13, introduced earlier to model an unimorph actuating against an elastic tissue, can also be used for bimorphs with the proper expressions for α and β. Shown in Figure 2-13b) is the effect that changing the actuator thickness has upon the peak deflection when an elastic tissue is and is not present. The peak deflection of a very thick actuator is small and nearly unchanged with the tissue, whereas the peak deflection is markedly decreased with a thin actuator, as it cannot generate the necessary force to stretch the tissue. The ideal actuator thickness would be somewhere between those two limits; it should generate a large peak deflection that is significantly affected by the presence of a tissue to allow for measurement of tissue stiffness, yet not so much so that it becomes incapable of achieving the desired ±5% stretch.

Actuator length is another dimension that should be optimized for stretching an elastic tissue. As shown in Figure 2-13c), the peak deflection with and without a tissue

diverges as the actuator length increases, which would allow for easier measurement of tissue stiffness. Furthermore, as the actuator length increases, the ideal actuator thickness increases. All the above relationships should be considered in future work to optimize the actuator design to allow for tissue stretching and measurement of tissue mechanics.

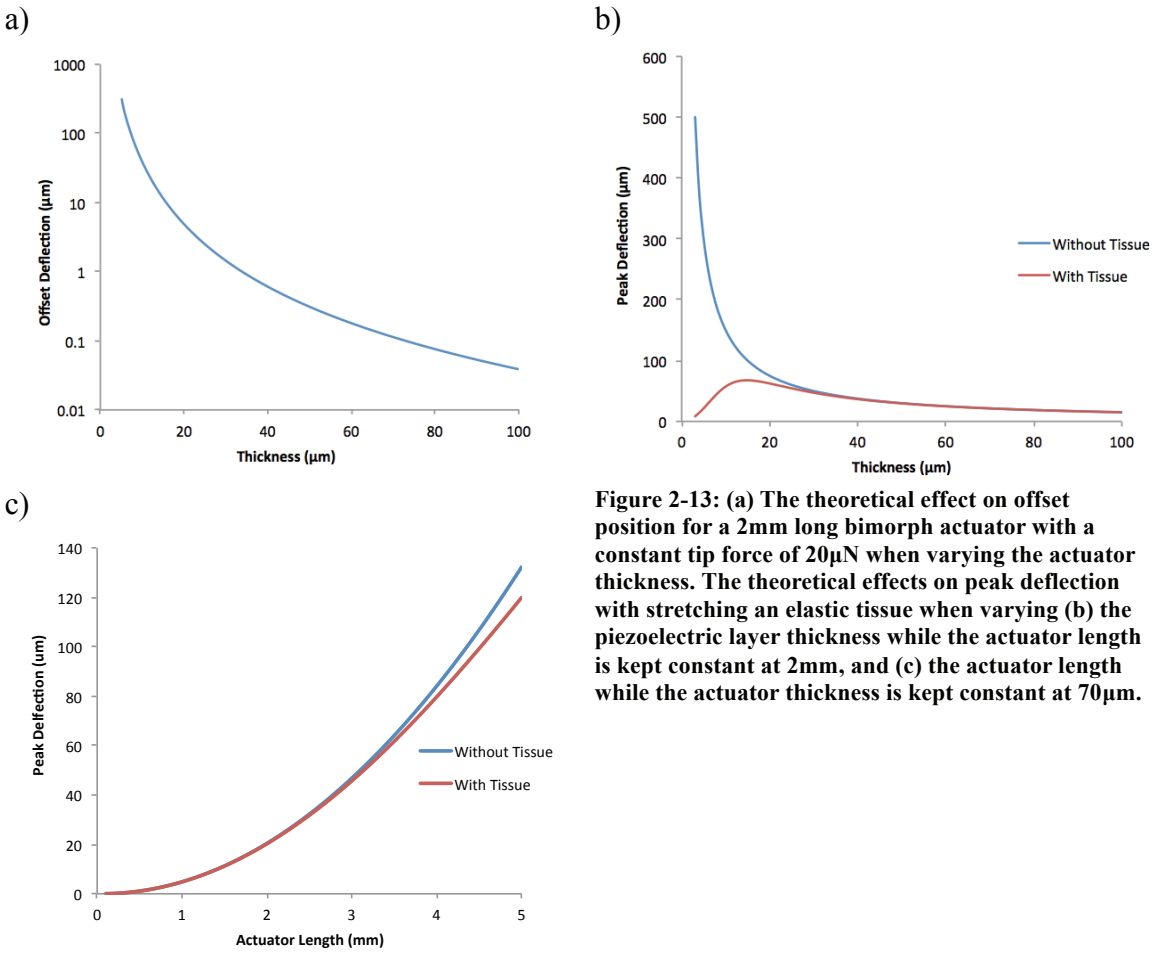

Figure 2-13: (a) The theoretical effect on offset position for a 2mm long bimorph actuator with a constant tip force of 20µN when varying the actuator thickness. The theoretical effects on peak deflection with stretching an elastic tissue when varying (b) the piezoelectric layer thickness while the actuator length is kept constant at 2mm, and (c) the actuator length while the actuator thickness is kept constant at 70µm.

Modeling of coated bimorphs

Piezoelectric Bending

Modifying the approach outlined by Dunsch and Breguet (7), the effect of a coating on piezoelectric bending can be modeled with the following assumptions: 1)

actuator bending can be described by Euler-Bernoulli beam theory; 2) there is no slip between the layers; and 3) the beam is in a static equilibrium: ΣF=0;ΣM=0. Shown in Figure 2-14 is the cross-section of a coated bimorph and the coordinate system used in the equations.

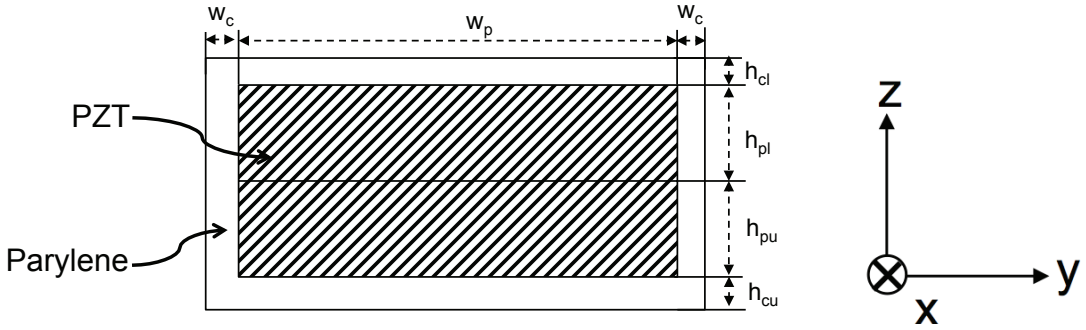

Figure 2-14: The cross section of a coated bimorph used for modeling piezoelectric bending.

The force and moment acting in the bender can be calculated by integrating the stress, σ, over the cross-sectional area.

$$F = \iint \sigma dydz \quad (14)$$

$$M = \iint \sigma z dydz \quad (15)$$

Unlike previous approaches used to model piezoelectric bending, the approach by Dunsch and Breguet (7) incorporates the position of the neutral axis, γ, within the limits of integration so that it can easily be found when the bender is not symmetrical. The limits of integration in the z-direction for a bimorph with an exterior coating are therefore as follows:

$$z_1 = \gamma;\ \ z_2 = z_1 + h_{cl};\ \ z_3 = z_2 + h_{pl};\ \ z_4 = z_3 + h_{pu};\ \ z_5 = z_4 + h_{cu};\ \ (16)$$

The stresses in the actuator are:

$$\sigma_{cu} = \frac{1}{s_{11}^c} w(\varepsilon_o z) \quad (17)$$

$$\sigma_{pu} = \frac{1}{s_{11}^p} w(\varepsilon_o z - d_{31} E_3^u) \quad (18)$$

$$\sigma_{pl} = \frac{1}{s_{11}^p} w\left(\varepsilon_o z + d_{31} E_3^l\right) \quad (19)$$

$$\sigma_{cu} = \frac{1}{s_{11}^c} w(\varepsilon_o z) \quad (20)$$

With the above set of equations, the resulting force and moment can be calculated.[1]

$$F = \int_{z_1}^{z_2} \left(\int_0^{w_p+2w_c} \frac{1}{s_{11}^c} (\varepsilon_o z) dy \right) dz + \int_{z_2}^{z_3} \left(\int_{w_c}^{w_p+w_c} \frac{1}{s_{11}^p} \left(\varepsilon_o z + d_{31} E_3^l\right) dy \right.$$
$$\left. + \int_0^{w_c} \frac{1}{s_{11}^c} \varepsilon_o z \, dy + \int_{w_p+w_c}^{w_p+2w_c} \frac{1}{s_{11}^c} \varepsilon_o z \, dy \right) dz + \int_{z_3}^{z_4} \left(\int_{w_c}^{w_p+w_c} \frac{1}{s_{11}^p} \left(\varepsilon_o z - d_{31} E_3^l\right) dy \right.$$
$$\left. + \int_0^{w_c} \frac{1}{s_{11}^c} \varepsilon_o z \, dy + \int_{w_p+w_c}^{w_p+2w_c} \frac{1}{s_{11}^c} \varepsilon_o z \, dy \right) dz + \int_{z_4}^{z_5} \left(\int_0^{w_p+2w_c} \frac{1}{s_{11}^c} (\varepsilon_o z) dy \right) dz \quad (21)$$

$$M = \int_{z_1}^{z_2} \left(\int_0^{w_p+2w_c} \frac{1}{s_{11}^c} (\varepsilon_o z) z dy \right) dz + \int_{z_2}^{z_3} \left(\int_{w_c}^{w_p+w_c} \frac{1}{s_{11}^p} \left(\varepsilon_o z + d_{31} E_3^l\right) z dy \right.$$
$$\left. + \int_0^{w_c} \frac{1}{s_{11}^c} (\varepsilon_o z) z \, dy + \int_{w_p+w_c}^{w_p+2w_c} \frac{1}{s_{11}^c} (\varepsilon_o z) z \, dy \right) dz$$
$$+ \int_{z_3}^{z_4} \left(\int_{w_c}^{w_p+w_c} \frac{1}{s_{11}^p} \left(\varepsilon_o z - d_{31} E_3^l\right) z dy + \int_0^{w_c} \frac{1}{s_{11}^c} (\varepsilon_o z) z \, dy \right.$$
$$\left. + \int_{w_p+w_c}^{w_p+2w_c} \frac{1}{s_{11}^c} (\varepsilon_o z) z \, dy \right) dz + \int_{z_4}^{z_5} \left(\int_0^{w_p+2w_c} \frac{1}{s_{11}^c} (\varepsilon_o z) z dy \right) dz \quad (22)$$

[1] Note that the integration is about both the z and y directions because the sides of the bimorph are also coated.

The equations for force and moment can then be solved for the internal strain, $\varepsilon_o z$, and the position of the neutral plane, γ, with the equilibrium condition that $\Sigma F=0;\Sigma M=0$. Then according to beam theory, the deflection of the actuator can be calculated by the double integration with respect to x.

$$\theta(x) = d'(x) = \int \varepsilon_o \, dx \quad (23)$$

$$d(x) = \int d'(x) dx \quad (24)$$

The effect on the theoretical peak deflection of altering the coating thickness and elastic modulus is shown in Figure 2-15. The theoretical modulus of parylene-C films is 4.2GPa. As expected, thin compliant coatings have little effect, while thick stiff coatings will greatly decrease piezoelectric bending.

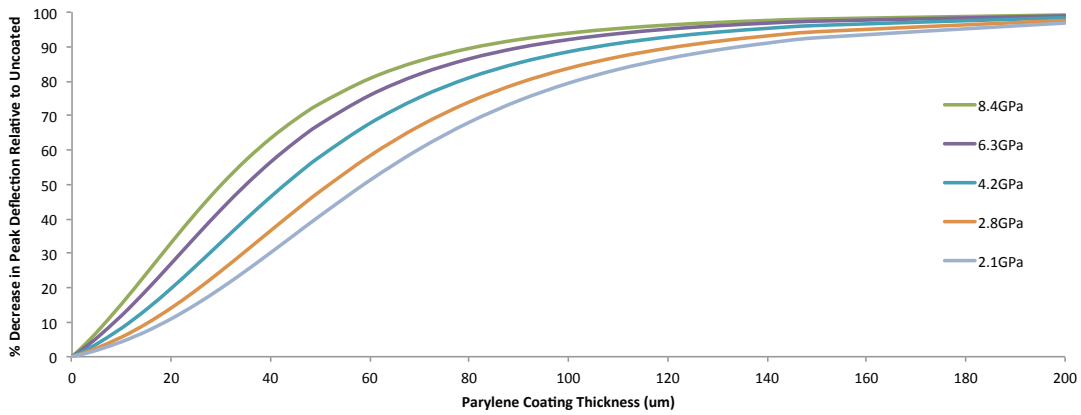

Figure 2-15: The effect of varying the parylene coating thickness and compliance on piezoelectric bending of a 70μm thick actuator with the maximal allowed applied voltage (i.e. the coercive field).

Mechanical Bending

Since the actuators will also be exposed to external forces from the baseline tone and contractility of the tissue, a model of mechanical bending of a coated post was

required as well. For modeling purposes, the same assumptions as in the piezoelectric bending model had to be made.

When a beam is subjected to pure bending, the curvature of the neutral surface may be expressed as

$$\theta = \frac{d^2z}{dx^2} = \frac{M(x)s_{11}}{I} \quad (25)$$

Where M(x) is the externally applied bending moment, I is the moment of inertia, and s_{11} is the elastic compliance. For a composite beam made of two materials with different compliances, the equation becomes

$$\frac{d^2z}{dx^2} = \frac{M(x)}{\sum EI} = \frac{M(x)}{I_p/s_{11}^p + I_c/s_{11}^c} \quad (26)$$

For a coated bimorph the moments of inertia of the piezoelectric material, I_p, and of the parylene, I_c, are

$$I_p = \frac{bh^3}{12}; \; I_c = \frac{BH^3 - bh^3}{12} \quad (27)$$

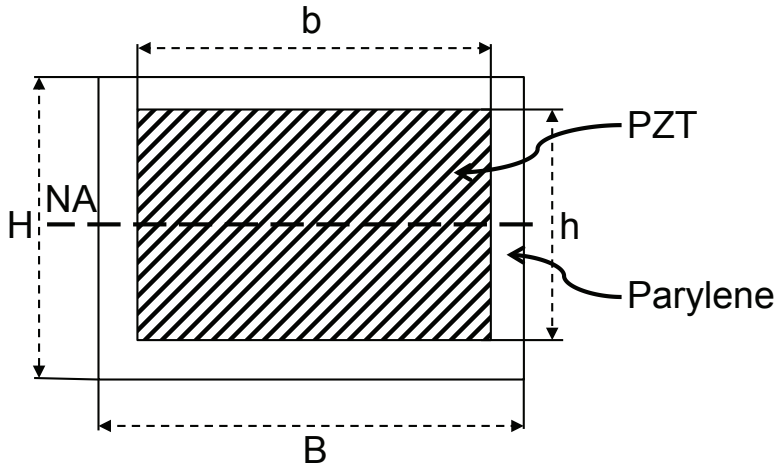

Figure 2-16: The cross section of a coated bimorph used for modeling mechanical bending.

A formula for the tip deflection can then be derived by substituting the moments of inertia

into equation (26) and integrating twice with respect to x.

$$d_c = \frac{FL^3}{3\left(I_p/s_{11}^p + I_c/s_{11}^c\right)} \quad (28)$$

Since we are concerned with the difference between the deflection without and with a coating, the ratio is:

$$\frac{d_c}{d} = \frac{\frac{FL^3}{3\left(I_p/s_{11}^p + I_c/s_{11}^c\right)}}{\frac{s_{11}^p FL^3}{3I_p}} \quad (29)$$

which can be simplified to:

$$\frac{d_c}{d} = \frac{1}{1 + I_c s_{11}^p / I_P s_{11}^c} \quad (30)$$

The effect on the theoretical peak deflection of altering the coating thickness and compliance is shown in Figure 2-17. Similarly to piezoelectric bending, thin compliant coatings have little effect, while thick stiff coatings will greatly decrease mechanical bending.

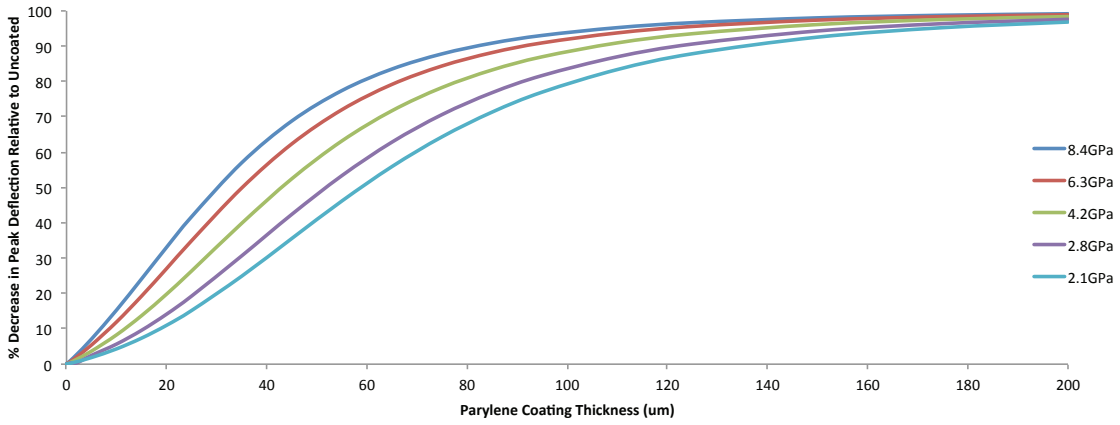

Figure 2-17: The effect of varying the parylene coating thickness and compliance on mechanical bending of a 70µm thick actuator.

2.5.3 Methods (the third approach)

Device Fabrication

Although I had much more success with the second protocol compared to the first, it still had its limitations, most of which had to do with the attachment to the base. A number of samples ended up with both sides epoxied together, or sides that were skewed and not parallel. For this reason, a third approach was developed, in which bimorphs, instead of unimorphs, were epoxied into slots spaced apart by the desired tissue length in a separate base. Photographs taken during the array fabrication and schematic drawings are shown Figure I-1 and I-2, respectively, in the appendix. The protocol is briefly outlined below:

1) A flat plate of piezoelectric ceramic with the manufacture's electrodes was lapped to half the desired total actuator thickness.
2) The sample was then sputtered for a short time (i.e. 5x1min at 500W) to form an inner electrode. This sputtering step was likely not critical to the actuation of the bimorphs since a series connection was used. However, it likely improved the consistency between actuators in a sample because it ensured a homogeneous electrical field across both piezoelectric plates even if the epoxy layer holding them together was uneven. Besides, it did not affect the deflection since the electrode was at the neutral axis and a negligible thickness.
3) A second flat plate of piezoelectric ceramic with the manufacture's electrodes was epoxied on top of the first plate with the polarization directions opposing one another. As with the previous protocols, it was critical that the epoxy layer was even and a negligible thickness.

4) The sample was lapped again so the thickness of the second piezoelectric layer matched the bottom piezoelectric layer.
5) The sample was sputtered again for a short time (i.e. 5x1min at 500W) to form one of the outer electrodes. The other outer electrode was the manufacturer's electrode on the bottom of the first plate.
6) The edges of the sample were diced away to ensure no electrical connection between the electrodes, and the sample was diced in half so to produce two identical bimorphs.
7) Two 100μm wide slots were diced into a block of PZT. The slots were spaced apart by 600μm, the desired tissue length. Chemically resistant, clear PVC eventually replaced the PZT as the material for the base in later samples because of the cytotoxicity and optical opacity of PZT.
8) The bimorphs were gently slid into each slot and epoxied into place.
9) The sample was encased in cyanoacrylate glue and diced into many miniature actuators. The cyanoacrylate glue was removed once the dicing was completed using the cyanoacrylate solvent.
10) Micro-coaxial cables were attached using conductive epoxy to each outer electrode.
11) A thin layer of parylene C (Speciality Coating Systems, Indianapolis, IN) was chemically vapour deposited (Labcoater PDS 2010, Speciality Coating Systems, Indianapolis, IN) onto the sample to act as a barrier for biocompatibility and electrical insulation. The parylene thickness was estimated using a calibration curve based on the mass of parylene dimer loaded into the machine. To confirm the parylene thickness, sections of parylene were taken from the surface of the

plate that the sample was resting on during the coating process and measured using a thickness gauge (ID-H0530E, Mitutoyo, Aurora, IL) with a resolution of 0.5um.

The fabrication process did take several weeks to complete a sample, largely because of waiting times for epoxies to cure. For future investigations, it is certainly possible to speed the fabrication of several samples by working on them in parallel.

Stiffness Measurements

For measurements of actuator stiffness, the same camera setup as for capturing piezoelectric bending was used. On the other arm of the micromanipulator, a force transducer (406A, Aurora Scientific, Aurora, ON) was mounted perpendicular to the actuators with a pointed glass microcapillary tube attached to its input tip. Photographs of the experimental setup are shown in Figure 2-18a), b) and c). The force transducer has previous been used in our lab for studying the effects of stretch on individual cell stiffness, and so its resolution of 10nN was more than sufficient to measure the actuator stiffness. Using the micromanipulator, the force transducer was moved until the tip of the microcapillary tube just contacted the top of an actuator. The point of contact was determined by a change in the force output channel. The tracking program then measured the actuator deflection while the force transducer was slowly advanced ~10μm and then brought back to its original position. From the deflection and force unloading data, a quasi-static post stiffness was derived for uncoated and coated actuators under both short and open circuit conditions.

a)

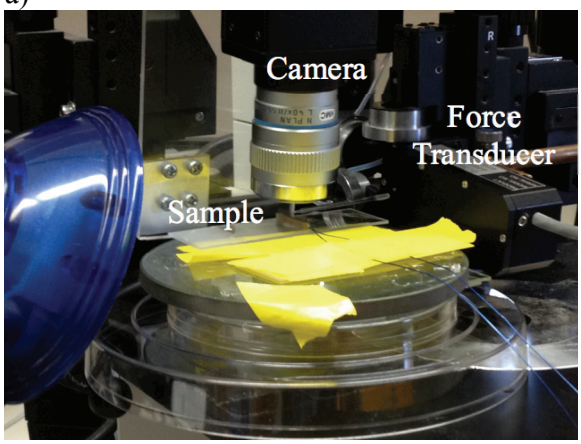

b)

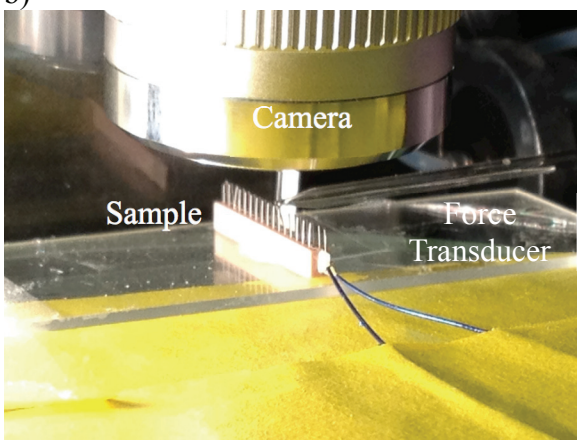

c)

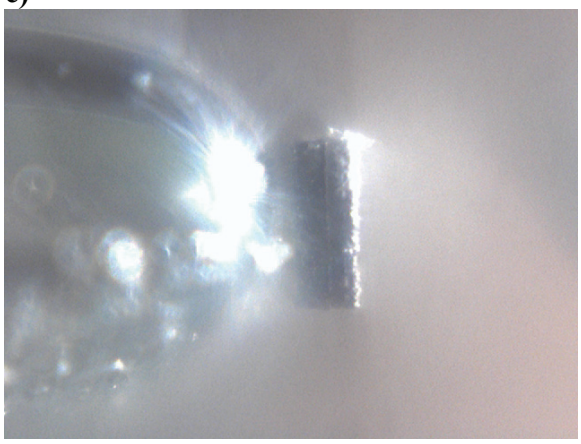

Figure 2-18: **(a) and (b) Photographs taken of the setup used to measure actuator stiffness. A force transducer mounted on a micromanipulator slowly bent one actuator at a time while a camera mounted above the sample captured the tip deflection. (c) An image of the microcapillary tube attached to the force transducer contacting the tip of an actuator.**

Blocking Force

Using the same setup as for the measurements of stiffness, the blocking force of the actuators was determined. Again the force transducer was moved with the micromanipulator until it just contacted the top of an actuator. Then instead of advancing the force transducer any further, a DC voltage was applied so the actuator would push against the microcapillary tube attached to the force transducer. At the same time the motion of the actuators was tracked to ensure that the post deflection could be accounted in the calculation of blocking force. For the data analysis, the force was average over 10 seconds once the signal had began to flattened out.

Actuator Dimensions

The width, thickness and length used in modeling the actuators were confirmed by measuring the pixel distance on calibrated images.

Data Analysis

Deflection data was collected with the same setup as in the previous approaches and analyzed in the frequency domain to find the peak deflection. Repeated measures two-tail t-tests were used to compare the deflection of uncoated to coated actuators with a F-test to confirm homogeneity of variances. A one-way ANOVA was conducted to test for a frequency response with a Levene's test to confirm homogeneity of variances. A two-way ANOVA was used to examine for a change in stiffness due to the parylene coating and a change in PZT compliance when in open or short circuit. For all statistical comparisons, $P<0.05$ was significant. Errors bars on all graphs are the standard error.

2.5.4 Results (the third approach)

Device fabrication

The third approach avoided many of the problems of the previous two. Like the second approach, there was no problem with sputtering on the electrodes or with delamination between the layers. Placing the actuators in slots in a separately manufactured base was also a great improvement compared to the other two approaches as it spaced the actuators evenly apart and made sets of actuators parallel to one another.

Photographs of the actuators fabricated with this approach are shown in Figure 2-19.

a) b)

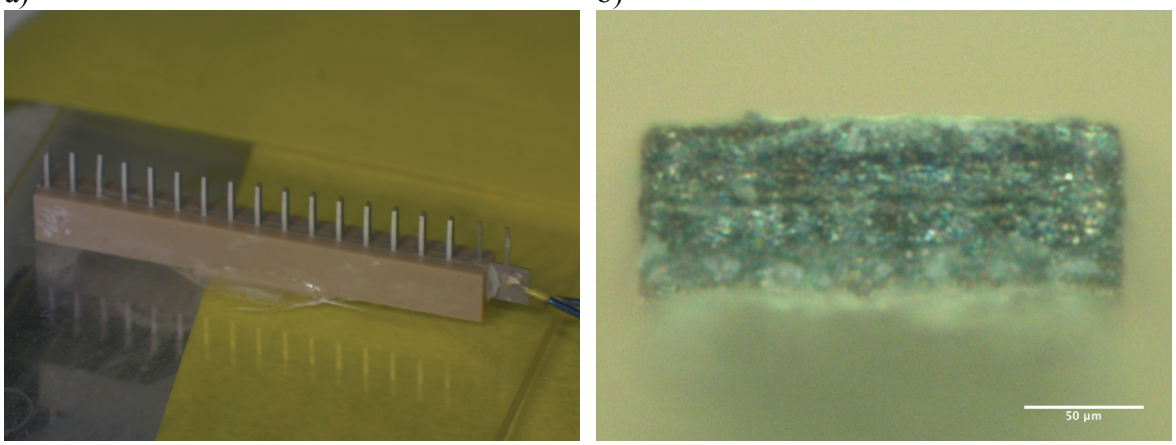

Figure 2-19: Photographs taken of the device fabricated with the third approach. Panel (a) is a macroscopic view of the array of actuators. The distance between sets of actuators is 1mm. Panel (b) is a microscope view of the tip of an actuator.

Deflection Data

The deflection of the actuators was measured with the same setup as for the previous approaches of actuator fabrication. A thin (3µm) layer of parylene was then deposited onto the actuators to act as a barrier for biocompatibility and electrical insulation. The deflection of the actuators was measured a second time to examine for the effect that the parylene coating may have had on deflection. Shown in Figure 2-20a) is the peak deflection at various voltages for uncoated and coated actuators when driven with a 0.3Hz sinewave. Surprisingly the peak deflection (17.14 ± 0.45µm at 20V) was greater than the theoretical prediction (7.87µm at 20V) for an uncoated bimorph with the same dimensions (2mmx70µmx200µm) for all tested voltages. The parylene coating significantly decreased the peak deflection by 19.6% but the deflection still remained greater than the theoretical prediction (Figure 2-20b). The deflection at the highest measured voltage (13.88 ± 0.40µm at 20V) for the coated actuators was slightly less than

the desired deflection (15µm). However at 20V, the electric field for a 70µm thick actuator (0.29V/µm) was considerably lower than the coercive field (0.78V/µm) given by the manufacturer so higher voltages may have been acceptable.

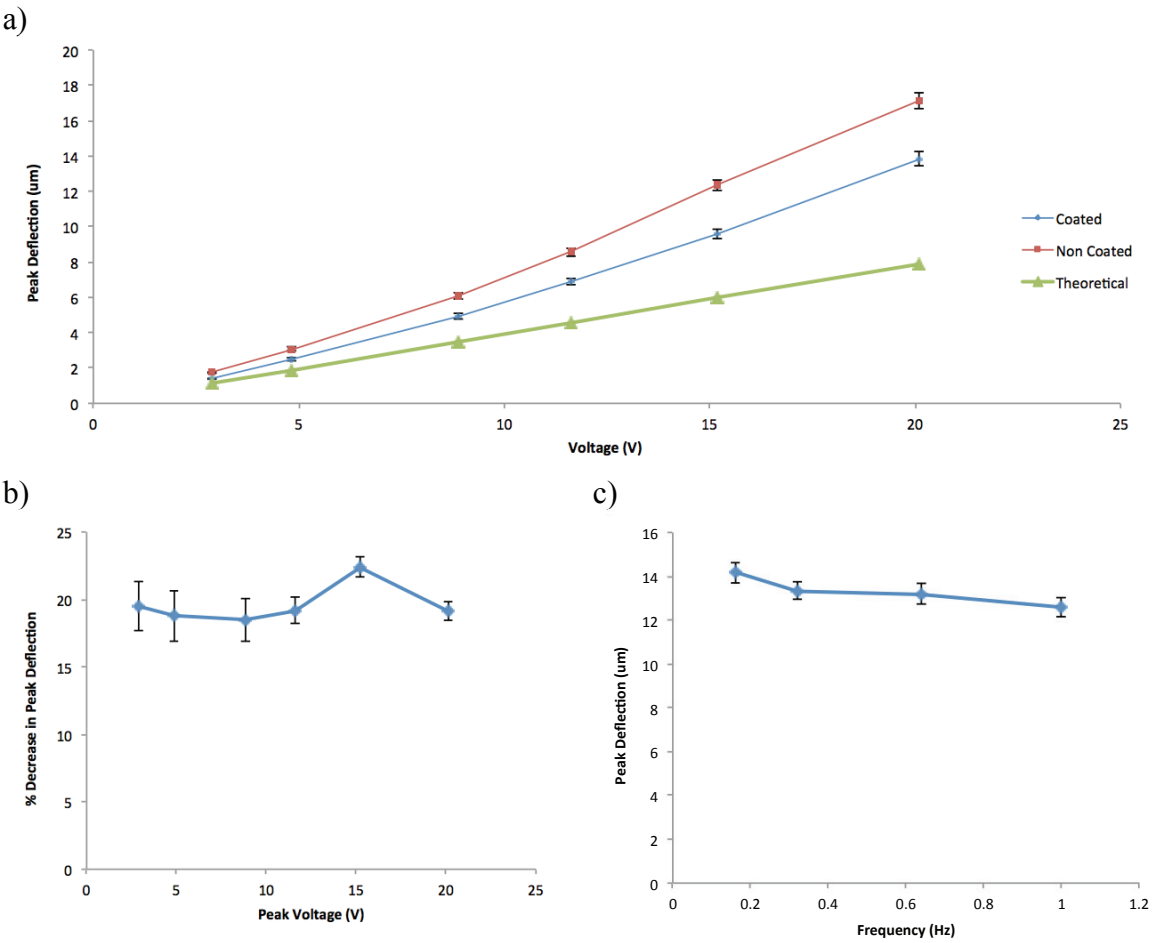

Figure 2-20: (a) The relationship between voltage and peak deflection for non-coated, and parylene coated actuators (2mmx200µmx70µm; lxwxt) when operating at 0.3Hz (n=15). At all measured voltages, the actuators achieved peak deflections greater than theoretically predicted. (b) The parylene coating accounted for roughly a 20% decrease in peak deflection at all measured voltages. (c) The relationship between frequency and peak deflection. There was no statistical difference in actuator deflection when operating between 0.15 and 1Hz.

For these tests, I was extremely cautious with applying high voltages. In another sample with thinner (50µm) actuators the measured peak deflection at 20V was 23.10 ±1.04µm, however the peak deflection of the actuators significantly decreased when the

applied voltage was increased to 30V. The method of failure is unknown. It is possible that the high strains caused a mechanical failure, however there was no visible evidence of cracks. An alternative hypothesis is that the high strains caused the ceramic to depole even though the field strength was below the coercive field. Since the actuators were connected in series, they could not be simply repoled to test this hypothesis. For future work, a parallel connection would be of great benefit.

In a similar manner to the unimorphs, the bimorphs were tracked at frequencies ranging from 0.15 to 1Hz with a 20V-applied sinewave. Shown in Figure 2-20c) is the frequency response of coated posts. A one-way ANOVA did not reveal any significant differences between the frequencies ($p=0.097$). In other words, the useable frequency range to achieve the statistically same deflection is at least from 0.15 to 1Hz.

Stiffness Measurements

Representative force-deflection curves for non-coated and coated actuators are shown in Figure 2-21a) and the average measurements are shown in Figure 2-21b). The stiffness of the actuators were also measured under both open and short circuit conditions since it was expected that the piezoelectric effect would generate charge that would oppose bending. The measured stiffness of non-coated actuators was 33.0 ± 1.4 μN/μm. A two-way ANOVA found that the parylene coating significantly increased actuator stiffness by 24.6%[1], while there was no difference in stiffness when measured under open

[1] This value is given as a percent change in stiffness, however the models represented the effect of the parylene coating as a percent change in deflection. If this value were converted to a percent decrease in deflection it would be 19.7%.

a)

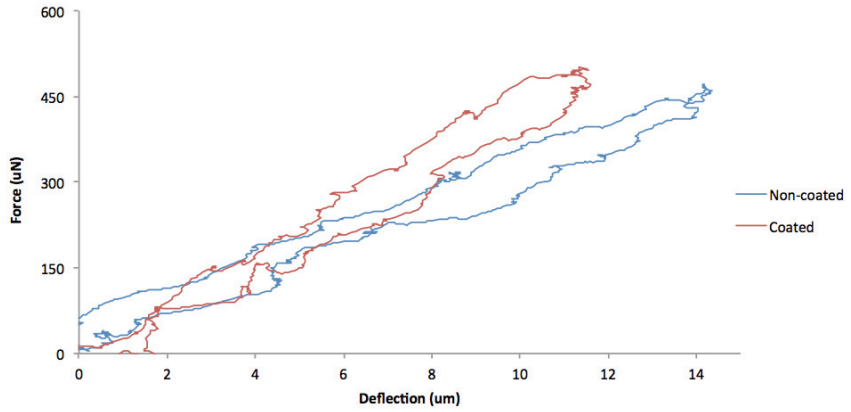

b)

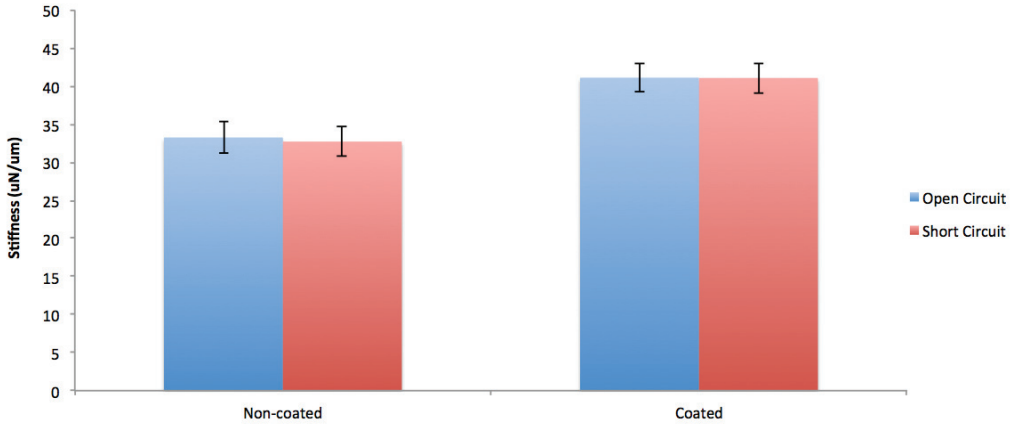

c)

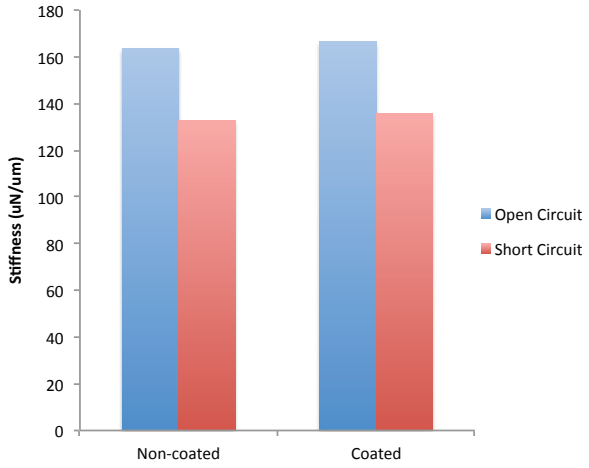

d)

Constant	Value
S_p^{11} (short) (m^2/N)	0.1631e-10
S_p^{11} (open) (m^2/N)	0.131e-10
S_c^{11} (m^2/N)	0.2381e-10
t_p (m)	70e-6
t_c (m)	3e-6
l (m)	2e-3
w (m)	200e-6

Figure 2-21: (a) Representative force-deflection curves for coated and non-coated actuators. (b) The average stiffness for coated and non-coated actuators measured under open and short circuit conditions (n=6). A two-way ANOVA found that the parylene coating caused a significant increase in stiffness, while the circuit condition had no effect. (c) The theoretical actuator stiffness modeled using the constants in Table (d).

or short circuit conditions. The absence of a difference in stiffness due to circuit condition can likely be explained by the relatively large surface area of the electrodes dissipating the charge off of the relatively small area of a single actuator. Another possibility is that, because of the slow rate of loading, all the generated charge leaked out of the actuator before it accumulated to a significant value.

Blocking Force

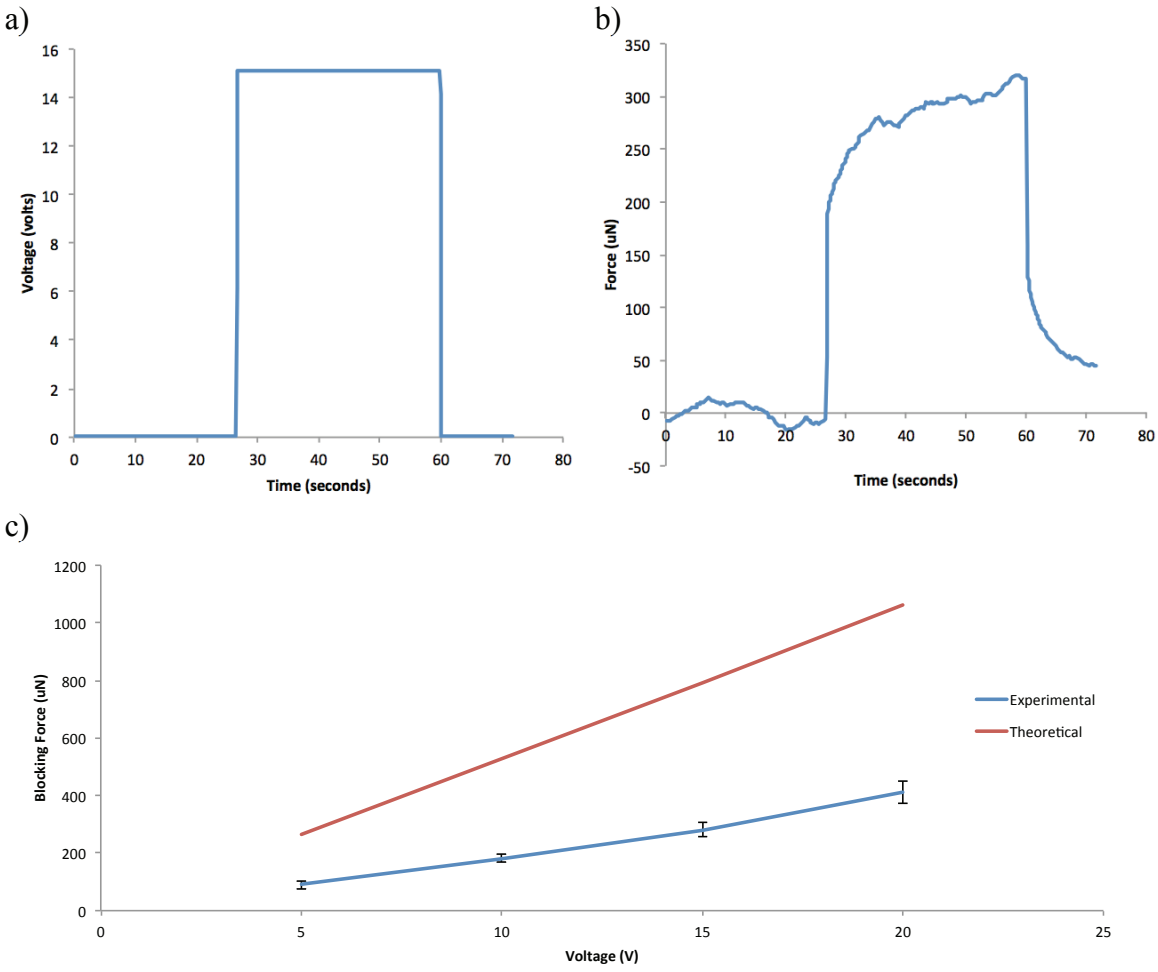

Figure 2-22: (a) To measure blocking force, a low frequency voltage square wave was sent into the device while (b) the resulting force was measured. (c) The relationship between applied voltage and blocking force (n=6). At all voltages, the measured blocking force was less than theoretically predicted.

The blocking force of parylene-coated actuators was measured to ensure that the actuators would be able to stretch the tissue. A representative measurement and the corresponding input voltage signal are shown in Figure 2-22a) and b). There was nearly a linear relationship between force and voltage, as shown in Figure 2-22c). At 20V the average measured force was 411±39μN. This value was, however, much less than the theoretically predicted value of 1059μN.

2.5.5 Discussion (the third approach)

The main finding from this portion of my thesis was that the approach of assembling actuators, securing them to the base, and then dicing them to form an array of miniature actuators could be successfully applied to bimorphs as well as unimorphs. As expected, the bimorphs tested in this section of my thesis showed considerably more normalized deflection than previously seen with the unimorphs. Furthermore, the deflection-voltage relationship was not linear. Nonlinearity in soft piezoelectric ceramics is well documented and has been attributed to the field dependence of elastic and piezoelectric coefficients due to extrinsic piezoelectric effects (i.e. domain-wall translation, and domain switching) (24). These effects contribute to greater than theoretically predicted peaks deflections at high voltages (24). Indeed, with only applying 20V, the deflection of 70μm thick, 2mm long bimorphs was greater than the desired 15μm. This nonlinearity, however, cannot explain the greater than theoretically predicted deflection at low voltages. In Figure IV-1 and Table V-1 in the appendix, I investigated in three different samples how changing the length of the actuator in the base affected the

measured piezoelectric deflection at low voltage and found that as this length decreased, the deflection approached the theoretical value. This finding suggests that the greater than theoretically predicted deflection at low voltages in this sample was caused by the 2mm length of the actuator in the base not being completely clamped by the relatively soft epoxy but rather contributing to the measured deflection. This effect of actuator motion in the base could be exploited in future work to achieve even greater peak deflections.

The parylene coating decreased the peak deflection by roughly 20% at all tested voltages. Although this effect was much greater than predicted by the model, it was remarkably similar to the measured increase (25%) in actuator stiffness due to the coating. The coated actuators were also shown to generate blocking forces up to 411μN. However, this value was likely an underestimation of the actual blocking force because of slight deflections of the actuators during the force measurement. For this reason, the generated forces with the measured deflections were plotted in Figure 2-23 with the free deflection data of coated actuators on a deflection-force graph. This graph is akin to equation (1), where the slope of the line of best fit is the α constant, which is the inverse of actuator stiffness, and the y-intercept is the β constant multiplied by the applied voltage.

Probably the most striking result from this graph is that the slopes, or stiffness, calculated at each voltage are nearly identical, giving an average value of stiffness of 44 ± 2μN/μm, which is in good agreement with the measured stiffness of 41.1 ± 1.3μN/μm. These values are, however, much lower than the theoretical value for the actuator stiffness (136μN/μm). Also from this graph, the blocking force is estimated to be 563μN at 20V. Although it is still less than the theoretically predicted value (1059μN), it is approximately 28x higher than the expected active tissue force (20μN). Therefore, the

actuators should not have any trouble overcoming the baseline tone or contractile force of the tissue.

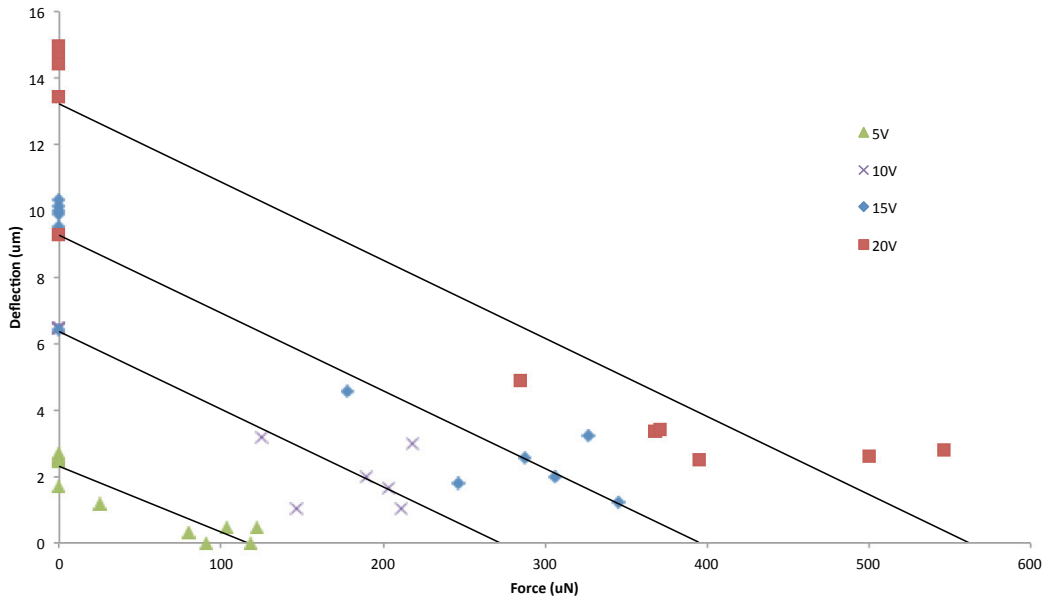

Figure 2-23: The relationship between deflection and force at different voltages (n=6). The y-intercept is the measured free deflection, the x-intercept is the measured blocking force and the slopes of the lines of best fit are the actuator stiffness.

Although there was good agreement between the measured values of actuator stiffness by the two methods and the effect of the parylene coating on piezoelectric deflection and stiffness, the reason for the large differences from the theoretical values is unclear. Contained in Table V-2, V-3, and V-4, in the appendix are the calculated differences from the measured/theoretical values for all the variables when individually altered in an attempt to account for the lower than expected stiffness measurements, and the greater than expected effect of the parylene coating on piezoelectric deflection and actuator stiffness, respectively. The results from these tables demonstrate that a single variable is not accountable. For example, if we assumed that only the actuator thickness was measured incorrectly, then to account for the lower than predicted actuator stiffness,

the actuator thickness would have to be 44μm rather than 70μm, which is not reasonable. Furthermore the explanation that the additional 2mm length of the actuators in the base accounted for the greater than theoretical piezoelectric deflection at low voltages, cannot fully explain the lower than predicted actuator stiffness, and moreover, the percent change in deflection and stiffness due to the parylene coating is not affected by the length of the actuator[1]. Another possibility worth mentioning is that the micromachining, mainly dicing the actuators into a microarray, may have caused micro-fractures in the PZT that greatly reduced its stiffness so to match the measured value of stiffness and percentage changes due to the parylene coating.

In addition to using the actuators to stretch the tissues, I also intended to use the bimorphs as sensors to measure changes in the mechanical properties of the tissues. In the *passive* microtissue model, the contractile force is estimated by imaging the deflection of the cantilevers (35, 60, 61). It would be nice if this same method could be used for the piezoelectric actuators. However, given that a microtissue will exert roughly 20μN of force on an actuator during a maximal contraction, the change in offset position will only be 0.5μm because of the high stiffness of the actuators. As for the passive tissue force, the tissues' elasticity, modeled by equation (13) and the tissue properties listed in Figure 2-4d), will only decrease the peak deflection by roughly 2% with the measured values of actuator stiffness and free deflection.

To improve the device's sensitivity to track changes in the mechanical properties of the tissues, the actuator stiffness needs to be reduced. The simplest method to decrease actuator stiffness would be to make the actuators thinner and longer. I have tried to

[1] This statement assumed that the length of the actuator remained constant. It is possible, however, that the parylene clamped further up the actuator, decreasing the effective actuator length.

fabricate actuators with dimensions of 2.5mmx25μmx400μm (lxt_pxw), which have a theoretical stiffness of 6.1μN/μm, however the majority (>80%) of the actuators cracked during dicing. This is not to say that this method cannot be applied to fabricate actuators that are more sensitive to tissue contractility and stiffness. Indeed, I have had success in fabricating actuators with dimensions of 1.5mmx25μmx400μm (lxt_pxw) that have a measured stiffness of 11.0μN/μm (theoretical: 28.7μN/μm).

Although future work is required to optimize the dimensions (i.e. length and thickness) to fabricate actuators with a lower stiffness, a total actuator thickness of 25μm is likely near, or at, the fabrication limit when starting with bulk PZT. To get even thinner actuators, other methods would therefore be necessary. An appealing alternative would be to use thin film techniques: physical vapour deposition, pulsed-laser deposition, chemical vapour deposition or chemical solution deposition (42). These techniques have already been successfully used to create PZT/silicon actuators with submicron piezoelectric layers. At this thickness, the actuators could be fabricated to match the cantilever stiffness and dimensions in the *passive* microtissue model, making these alternative techniques a very appealing option.

Another method to reduce actuator stiffness would be to use a more compliant material instead of PZT. For instance, polyvinylidene fluoride (PVDF) is a piezoelectric polymer that might be more suitable for this application as it is about 19x (3.1e-10 vs. 1.613e-11m^2/N) more compliant and not susceptible to brittle fracture. PVDF also has the added bonus that it would be biocompatible, as it has previously been shown not affect cellular survival (38). The d_{31} constant is, however, 21x (15e-12 vs. 320e-12 m/V) lower than compared to PZT but the coercive field strength (80 vs. 0.78 V/μm) is 10x higher.

Although it is important that these different techniques and materials be investigated, they were beyond the scope of this thesis. The current actuator design did, however, successfully prove the concept for fabricating an array of miniature piezoelectric actuators. Moreover, these actuators could be used to assess the feasibility of the other thesis aims: 1) microtissue formation, and survival; and 2) a self-sensing method for actuator deflection and force. To conclude this chapter, the fabrication of piezoelectric actuators for an active microtissue model is a challenging task, but offers the ability to probe cellular contractile and phenotypic responses in the presence or absence of dynamic mechanical strain of self-assembled, miniature, tissue engineered constructs in a high-throughput manner.

Chapter 3: Verification of Real-Time Actuator Tracking

To track the motion of the posts, I created two labview programs: the first uses a shape-matching algorithm, and the second uses a pattern-matching algorithm. The two main prerequisites to the programs were that they 1) operated quick enough to analyze the 15fps camera feed in real-time; and 2) provided sufficient resolution to accurately track movements to the submicron level.

In both programs, the actuators were tracked in both the x- and y-directions for roughly 60 seconds. The data was analyzed in the frequency domain to solve for the peak deflection for both directions. Then, with the use of Pythagoras' theorem, the overall actuator peak deflection was determined.

Analyzing the data in the frequency domain has the benefit that the Fourier transform acts as a narrow band spectrum analyzer that sweeps over the spectrum with a bandwidth of

$$Frequency\ resolution = \frac{Sampling\ frequency}{Size\ of\ the\ data\ set} \quad (29)$$

This has the effect of pushing down the noise, or raising the SNR, by the process gain

$$Process\ gain = 10log\frac{Size\ of\ the\ data\ set}{2} \quad (30)$$

By increasing the size of the data set, the noise floor is reduced, and the resolution of the tracking algorithm is increased. Moreover, the noise in the signal's bin is reduced due to a lower frequency resolution, which allows for more accurate measurements. Therefore, with a data collection time of 60 seconds (i.e. a data size of 900 points when collected at 15Hz), the deflection results should be quite accurate with a sufficient resolution.

3.1 Shape Matching

The first program that I designed extracted the intensity plane from the 32-bit RBGA image, converted it into a binary image, and then used Labview's shape matching function to find the position of the tip of the actuators. Shown in Figure 3-1a) and b) is representative actuator deflection data collected with the shape-matching algorithm expressed in both the time and frequency domains, respectively. The signal at the fundamental frequency (0.3Hz) was much greater than the noise in the surrounding bins.

a) b)

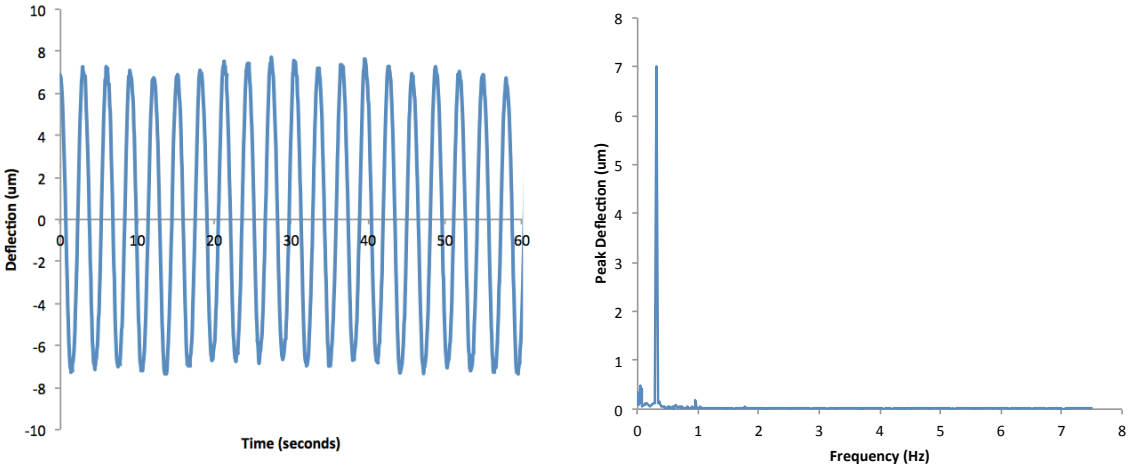

Figure 3-1: Representative deflection data analyzed with the shape matching algorithm expressed in a) the time and b) frequency domains.

The effect of changing the threshold for the binary image is shown in Figure 3-2. The range of tested thresholds extended from 160 up to 250. Outside this range, the post could not be tracked because the binary image was either entirely black or entirely white. The signal to noise ratio (SNR) and total harmonic distortion (THD) were calculated according to the following equations:

$$\boldsymbol{SNR}\ (dB) = 20log\left(\frac{RMS\ (Signal)}{RMS\ (noise)}\right) \quad (31)$$

$$THD\ (dB) = 10log\ \frac{{H_1}^2 + {H_1}^2 \ldots . {H_\infty}^2}{(Signal)^2} \quad (32)$$

The SNR and THD remained relatively constant throughout the range of tested thresholds indicating that the chosen threshold value had little bearing on the noise or the harmonics of the signal as long as it was within the useable range.

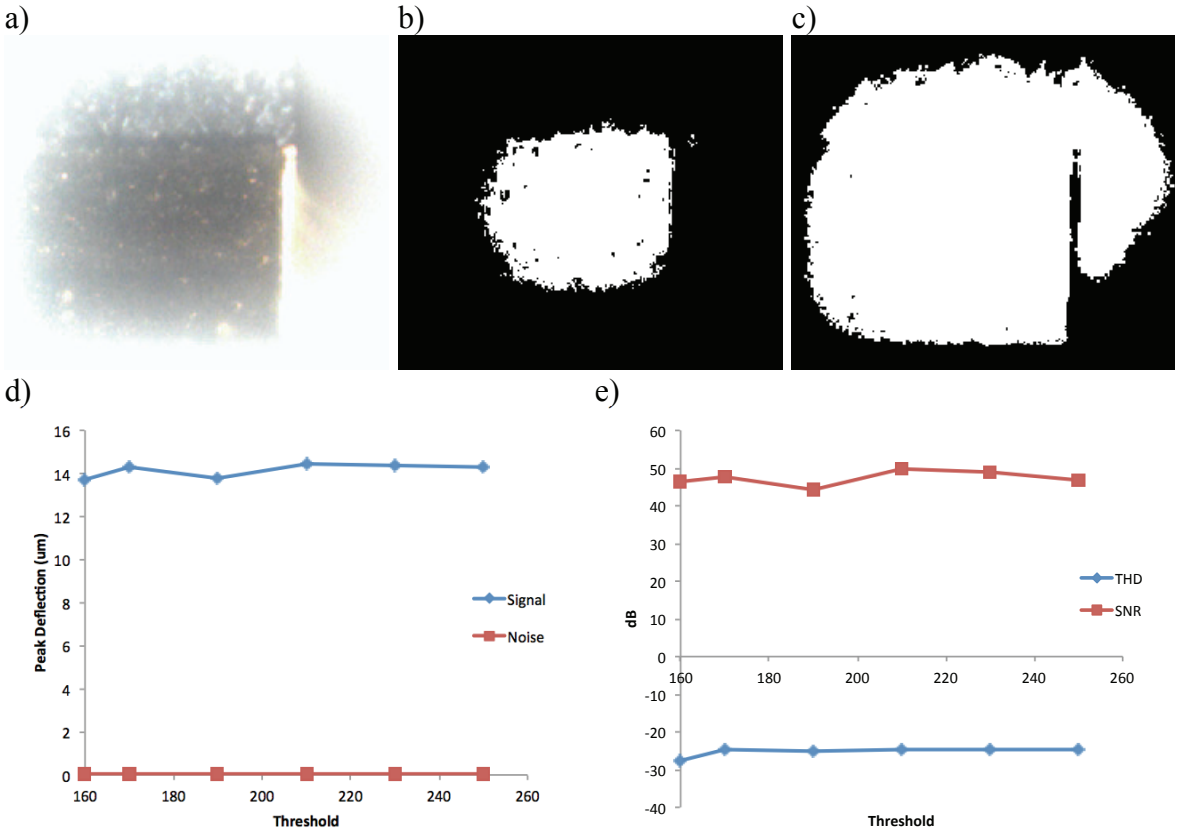

Figure 3-2: (a) An image of the tip of an actuator used to track deflection. To use the shape-matching algorithm, the image was converted into a binary image. Shown in panels (b) and (c) are example binary images with thresholds of 160 and 250, respectively. (d) Changing the threshold value had little effect on peak deflection and noise. (e) The calculated THD and SNR at all tested threshold values were acceptable.

The effect of changing the peak deflection and frequency of oscillation of the actuators is shown in Figure 3-3. Neither of these variables had any substantial impact on SNR nor THD, validating the program's ability to track the deflection of the posts within

the frequency and amplitude ranges tested. By defining the resolution as the deflection when SNR is equal to 1, the shape-matching tracking algorithm was capable of measuring theoretical peak deflections as small as 75nm when oscillating for 60 seconds.

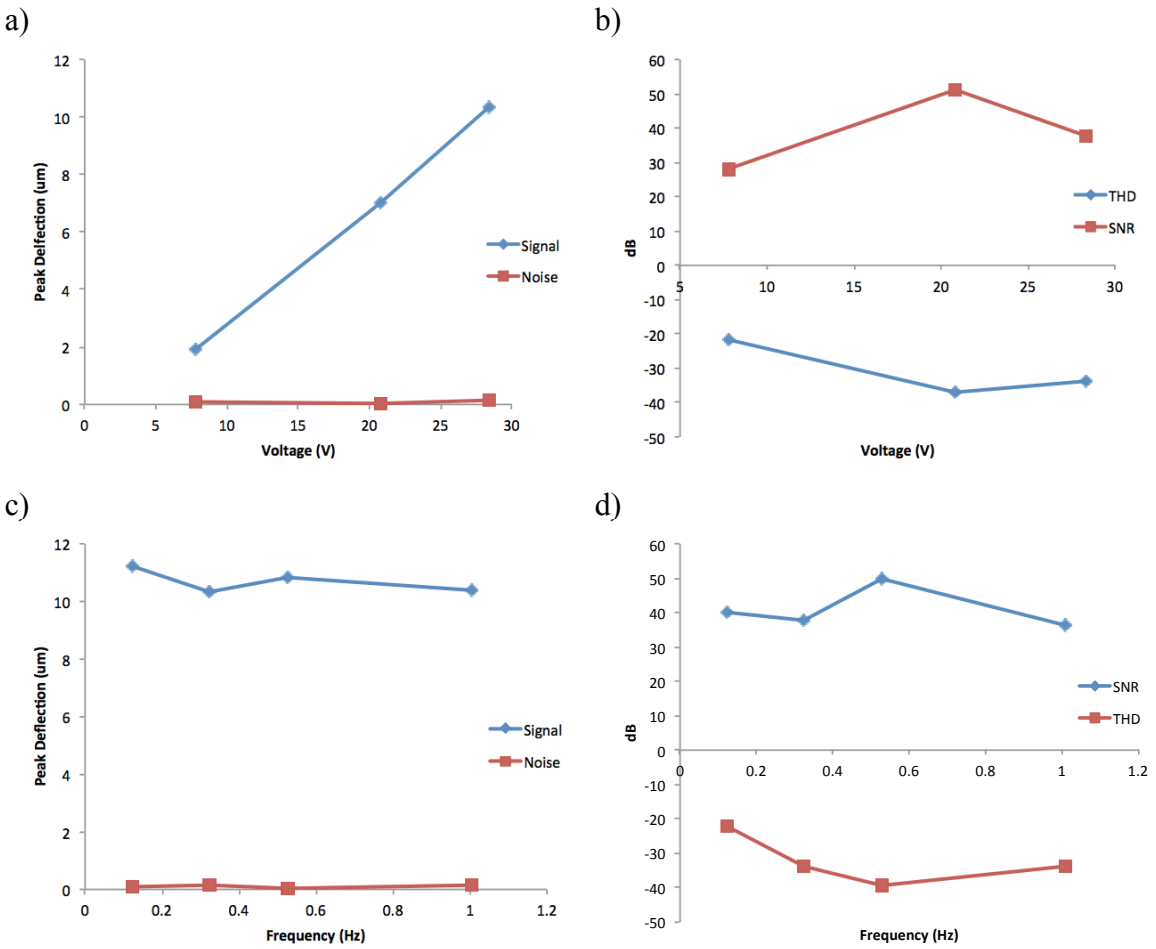

Figure 3-3: Changing the (a) applied voltage or (c) frequency had little effect on peak deflection and noise. The calculated THD and SNR at the tested (b) voltage and (d) frequency ranges were acceptable.

3.2 Pattern Matching

The shape-matching algorithm did work well when the posts were a different intensity value than the background. However, more often than not, the intensities nearly matched the background due to shadows from the low quality light source. In these cases, shape matching could not be used and so a more robust program was designed. In the

second program, the position of the post is found using Labview's pattern matching function on the intensity plane extracted from the 32-bit RBGA image. Shown in Figure 3-4 is representative actuator deflection data collected with the pattern-matching algorithm. As with the shape-matching algorithm, the noise was small in comparison to the signal.

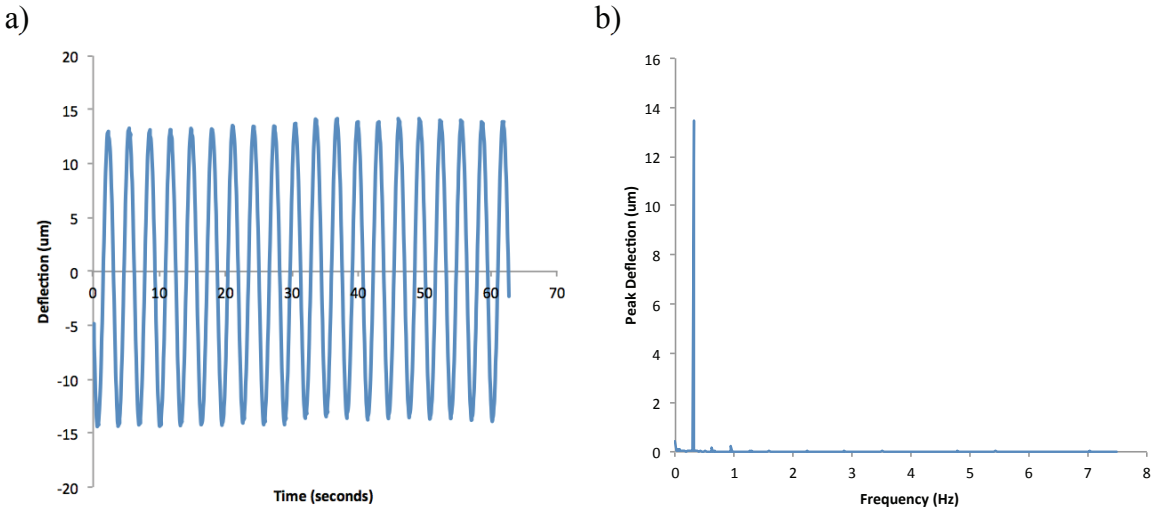

Figure 3-4: Representative deflection data analyzed with the pattern matching algorithm expressed in a) the time and b) frequency domains.

The effect of changing the peak deflection and frequency of oscillation of the actuators is shown in Figure 3-5. Both of these variables had a significant impact on SNR. It seemed that increasing the peak deflection increased the SNR, while increasing the frequency decreased the SNR. Neither of these variables, however, had an effect on THD. Nevertheless, the measured values for SNR and THD do validate the program's ability to track the deflection of the posts within the frequency and amplitude ranges tested.

Unlike the shape-matching algorithm, which found the position solely based on a geometric match in a binary image, the pattern-matching algorithm used both geometric

and intensity data to find the position for the best match, and therefore was capable of achieving a much better resolution. Indeed, with the same definition of resolution as used above, the pattern-matching algorithm was theoretically able to track peak deflections as small as 23nm when oscillating for 60 seconds.

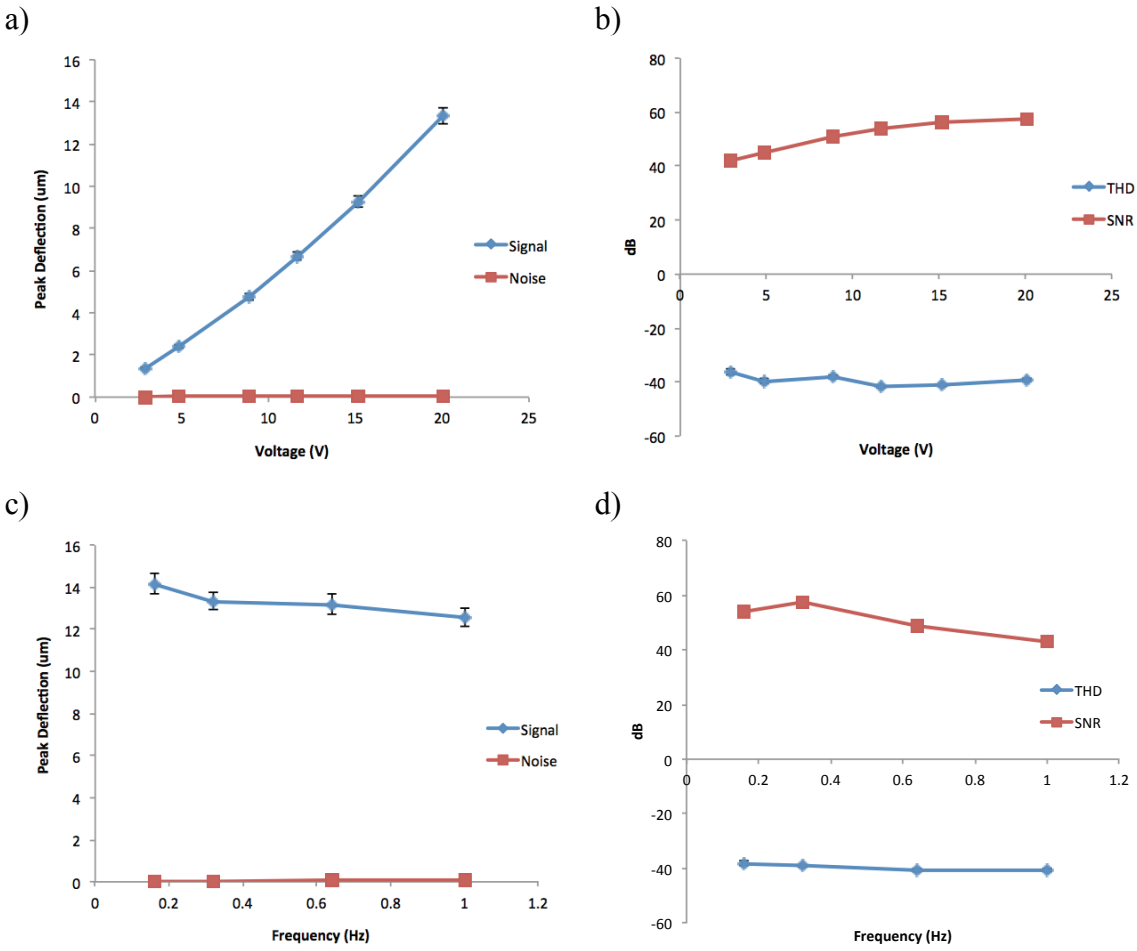

Figure 3-5: Changing the (a) applied voltage or (c) frequency had little effect on the noise compared to the signal. The calculated THD and SNR at the tested (b) voltage and (d) frequency ranges were acceptable.

Chapter 4: Microtissue Formation, Survival and Stiffness

4.1 Rationale

The effect of oscillatory stretch on ASM contractile phenotype has already been investigated in 2D cell culture and *ex vivo* tissue strips. There are distinct disadvantages to both these approaches. 2D cell cultures fail to recapitulate physiological conditions, while *ex vivo* tissue strips lack control over environmental and biochemical factors, have limited availability, cannot be used for chronic experiments, and display markedly lower intrinsic tone than observed *in vitro*. To fill the gap left by these two methods, there has been recent advancements in 3D cell culture techniques.

As described in the introduction, a 3D microtissue model for ASM has previously been developed in our lab (60, 61). Briefly, cells in a collagen solution are added to a specially designed PDMS mold and self-assemble around a pair cantilevers into a highly organized 3D structure similar to human tissue. Further benefits of this model are that gene and protein expression of the resulting microtissues can be assessed *in situ* through standard fluorescent staining protocols, and tissue tension can be measured from the visible deflection of the cantilevers and their known stiffness (35). These benefits make the microtissue system very desirable for the study of ASM contractile phenotype.

The purpose of this thesis was to simply expand this microtissue model to allow for future investigations into the effects of chronic oscillatory stretch on 3D cell culture. Thus as a proof of concept, I assessed whether live cells survived in the device, formed around the tops of sets of actuators into organized 3D structures and produced a

measureable response to contractile and relaxant agonists.

4.2 Methods

PDMS Wells

In the passive microtissue model, each set of cantilevers is located in an individual well. The well concentrates the cells around a set of cantilevers and prevents the cells from spanning multiple sets of cantilevers. For these reasons, the wells are critical to forming microtissues. In order to fabricate the wells, a negative mold was made to match the spacing of the actuators with the dicing saw. Using this mold, the wells were cast out of PDMS. The wells were then carefully lowered onto the device and secured in place with not yet polymerized PDMS.

Parylene Coating

Prior to forming tissues, the device was coated with parylene C. The coating process is illustrated in Figure 4-1. The Parylene coating was meant to serve two functions. The first was to act as a barrier for electrical insulation. Parylene C is regularly used as a thin coating for electrical components because of its excellent dielectric strength of 220 V/μm. The other function of the parylene coating was to serve as a barrier for biocompatibility. Parylene C has been FDA approved for implantable devices because of its biological and chemical inertness, which makes it appropriate for this device.

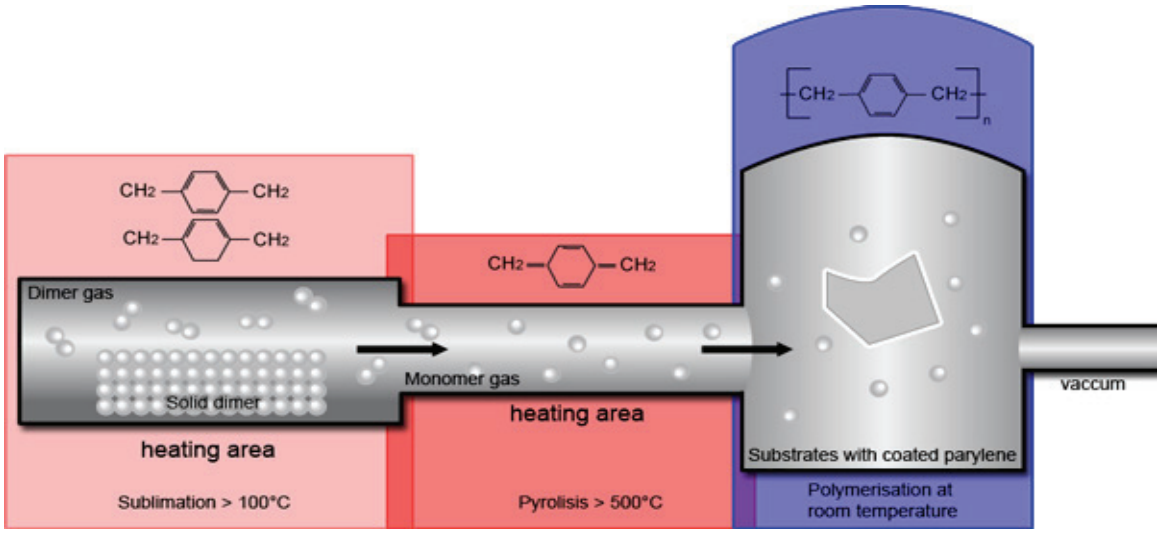

Figure 4-1: An illustration of the parylene deposition process. Parylene C, in the form of solid dimer is vaporized into a gas. This gas is further heated in another chamber until it is broken into monomers. These monomers flow into a third chamber containing the sample and polymerize on the sample's surface, forming a conformal coating.

Sample Silanization

A-174 silane (440159, Sigma Aldrich, Oakville, ON) has commonly been used to improve parylene adhesion to oxidized surfaces. A standard wet protocol was followed. In brief, the promotion solution was made of equal parts 99% pure isopropyl alcohol (IPA) and deionized water, to which A-174 silane, up to a final concentration of 0.5% (1 part to 200, by volume), was added. The samples were submerged in this solution for 15-30 minutes, dried, and then rinsed with IPA several times. The samples were always parylene coated within 24 hours.

Hydrolysis of Saline Bubble test

To test the quality of the parylene coating, samples were submerged in phosphate buffered saline (PBS) and a 9V electrical field was applied across the electrodes. The

formation of hydrogen or oxygen bubbles on the electrodes, due to the hydrolysis of water, was used as an indication whether there were pinholes in the coating.

Cell Culture

Human ASM cells (Donor 12) immortalised by stable transfection with human telomerase reverse transcriptase [previously characterised in (16)] were obtained as a generous gift from Dr. William Gerthoffer (University of South Alabama). Green fluorescent protein (GFP) labeled NIH-3T3 fibroblast cells were purchased commercially (AKR-214, CellBioLabs, San Diego, CA) and unlabelled NIH-3T3 fibroblast cells were obtained as a generous gift from Dr. Neale Ridgway (Dalhousie University). The cells were seeded into T-75 flasks (Costar, Cambridge, MA) and maintained in feeder media consisting of DMEM/F12 (11330, Invitrogen, Burlington, ON) with 10% FBS (12483, Invitrogen, Burlington, ON) and 1% penicillin-streptomycin (15140, Invitrogen, Burlington, ON) in a 37^{o}C humidified incubator with 5% CO_2 until 80-90% confluent.

Microtissue Formation

Previous work has shown that microtissues composed solely of 3T3 cells exhibited no structural problems (35) whereas microtissues fabricated with ASM cells required a minimum inclusion of 20% fibroblasts to provide structural integrity or they would dissociate from the posts within three days (61). Therefore, although ASM cells were eventually incorporated into the tissues to create a model for airway smooth muscle, it was reasoned that solely starting with 3T3 fibroblasts would provide the best chance to

form tissues, and as such, proof of concept of an *active* microtissue model. Once the concept was proven for microtissues solely consisting of fibroblasts, microtissues consisting of 80% ASM cells and 20% fibroblasts were fabricated.

Similar protocols for microtissue fabrication can be found in previous publications (24, 43). The dishes with the stretching devices were decontaminated by three washes with 70% ethanol and 15 minutes of UV radiation. The surfaces of the actuators and wells were treated with 0.2% pluronic F-127 (P6866, Invitrogen, Burlington, ON) for five minutes to reduce cell adhesion, rinsed with PBS, and air-dried. Once confluent, 3 million cells were centrifuged into a pellet and resuspended in a 3ml media-collagen mixture containing 1x DMEM/F12 (12400, Invitrogen, Burlington, ON), 14.3 mM $NaHCO_3$, 15mM d-ribose (R9629, Sigma Aldrich, Oakville, ON), 1% FBS, 2.5mg/ml collagen I (354326, BD Biosciences, Mississauga, ON) and 1M NaOH to achieve a final pH of 7.0-7.4. The cell-collagen solution was pipetted into the dishes. To remove the air bubbles blocking the entry of the solution into the wells, the dishes were vacuumed for 2 minutes. The cell-collagen solution was redistributed to get as many cells into the wells as possible, and then the excess was removed by aspiration. The dishes were incubated at 37^oC for 15min to initiate collagen polymerization. Feeder media was added to the dishes and changed every 24 hours.

Imaging and Survival Assay

Imaging was performed on a Leica DM IRB microscope using a 2.5x or 10x objective and captured with a PCO Sensicam CCD camera. Fluorescent fibroblasts were used for preliminary microtissue attempts because the device was optically opaque, and

as a consequence, the microtissues could not be captured under bright field. The GFP label on the fibroblasts also allowed for a convenient method to determine cell survival as the cells will only produce GFP if they were alive. At the same time point, the nuclei of all the cells were stained with Hoechst 33342 (H1399, Invitrogen, Burlington, ON; 5ug/ml) in PBS for 30 minutes and imaged to verify their presence. This cell survival assay, along with bright field imaging, was also used to independently test the biocompatibility of each element used to fabricate the device. For the ASM/fibroblast microtissues, the nuclei of dead cells were stained with propidium iodide (81845, Sigma Aldrich, Oakville, ON; 10ug/ml) in PBS for 30 min.

Tissue Stiffness Measurements

Stiffness measurements were taken three days after microtissue fabrication. One day prior to the measurements, the microtissues were switched to serum-free IT media consisting of DMEM/F12 with 5.8 µg/mL insulin (I1882, Sigma Aldrich, Oakville, ON) and 1.0 mg/mL transferrin (T4382, Sigma Aldrich, Oakville, ON). The tissue stiffness was calculated according to equation (33) using the measured peak deflections with (d_T) and without (d_o) the presence of the tissue, and the theoretical actuator compliance (α).[1]

$$S = \frac{(d_{o1} - d_{T1}) + (d_{o2} - d_{T2})}{2(d_{T1} + d_{T2})\alpha} \quad (33)$$

[1] Note that since essentially only the difference between two points of the tissues' force-length curve was measured, an assumption of linearity was made. In the future, an alternative method could include a separate higher frequency, low amplitude signal to measure the tissue stiffness at several points along its force-length curve.

The analysis only included microtissues that were mechanically secured to two functioning actuators and without any attachments to the sides of the wells.

The deflection of each set of actuators was imaged by the15 fps firewire camera through an Olympus BH2-UM microscope with a 5x objective and a 1.5x camera eyepiece adapter to give a sensitivity of 1.439μm/pixel. The camera feed was acquired and analyzed with the pattern-matching algorithm discussed in the third chapter, and with this setup, was capable of tracking deflections as small as 3.5nm.

The driving voltage for the actuators was produced and recorded by the 16-bit data acquisition card with digital to analog capability. To produce voltages greater than 10V, the output signal from the digital to analog convertor was amplified by the 20x voltage amplifier. In order to stretch the tissues using both actuators at the same time, the direction of the electric field was reversed for opposing rows of actuators. To investigate the stiffness-strain relationship, the actuators were driven at progressively larger voltages at 0.3Hz as shown in Figure 4-2. At each voltage, the tissues were preconditioned by oscillating for at least 2 minutes prior to measurements of tissue stiffness. Values of peak strain were calculated based on equation (34).

$$\varepsilon = \frac{(\delta_{T1} + \delta_{T2})}{L} \quad (34)$$

This procedure was completed at baseline and following sequential 20 minute incubations with a contractile agonist (80mM potassium chloride, KCl), a relaxant agonist (0.1mM forskolin), and an actin polymerization inhibitor (10μM cytochalasin D). Between pharmacological conditions, the tissues were washed with warmed IT media to

remove the effects of the previous treatment and kept in the incubator for an hour to allow for recovery to baseline.

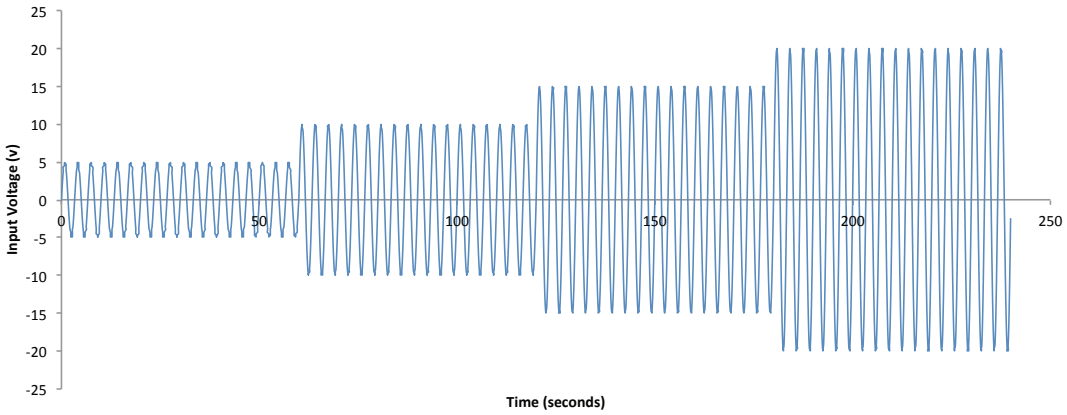

Figure 4-2: To investigate the stiffness-strain relationship, the actuators were driven at progressively larger voltages at 0.3Hz.

A linear regression analysis was used to examine the relationships between strain and stiffness. A repeated measures two-way ANOVA was used to examine for differences between pharmacological conditions.

Storage and Loss Moduli

The stiffness measurements calculated in the previous section were calculated as the magnitude of the oscillatory force over the oscillatory strain. However, the tissue relationship between force and strain is dynamic and it would be useful to measure the storage, E', and loss, E'', components of the tissues' stiffness. This can be accomplished by examining the phase, δ, between the applied oscillatory stress and the measured strain.

$$\tan(\delta) = \frac{E''}{E'} \quad (35)$$

The use of this analysis is unfortunately complicated because in the device the actuators are used also as the sensors, and thus a measured phase lag between the input stress (i.e. input voltage) and the output strain (i.e. the imaged actuator/tissue strain) represents the entire system rather than just the lag between stress and strain of the tissue. In other words, the magnitude of the phase lag does not only depend on the damping caused by the tissue but also the relative stiffness of the tissue to the stiffness of the actuators. Nevertheless, the phase of the applied stress to the system corresponds to the phase of the input voltage corrected for any phase lag caused by the finite electrode resistance, the extrinsic piezoelectric effect, and/or the software used for data collection. While, the phase of the resulting strain corresponds to the measured phase of the deflection of the actuators.

The difference in phase between these signals was measured in the frequency domain by examining the phases of the imaged actuator/tissue motion and the applied voltage signal. To correct the phase for the applied stress to the tissue, the analysis was first completed on the same actuators when the tissue was not present, and then subtracting the result.

4.3 Results

Preliminary Microtissue Attempts

Preliminary microtissue attempts used a device fabricated with the first approach outlined in the second chapter. Prior to adding the cells, the sample was coated with a 350nm layer of parylene C. This thickness of parylene was chosen solely based on its

dielectric strength and the maximal applied voltage. After two days, the cells were stained with Hoechst and imaged. There were clearly Hoechst-stained cells in the wells, and they had started to arrange themselves around the actuators (Figure 4-3). However, none of the cells expressed GFP, and so it was concluded that they were dead. Because this protocol has been used successfully before to make 3D cell cultures, and the positive control cells (not shown) in collagen gels without the device did not die, the cell death was likely due to a flawed parylene coating.

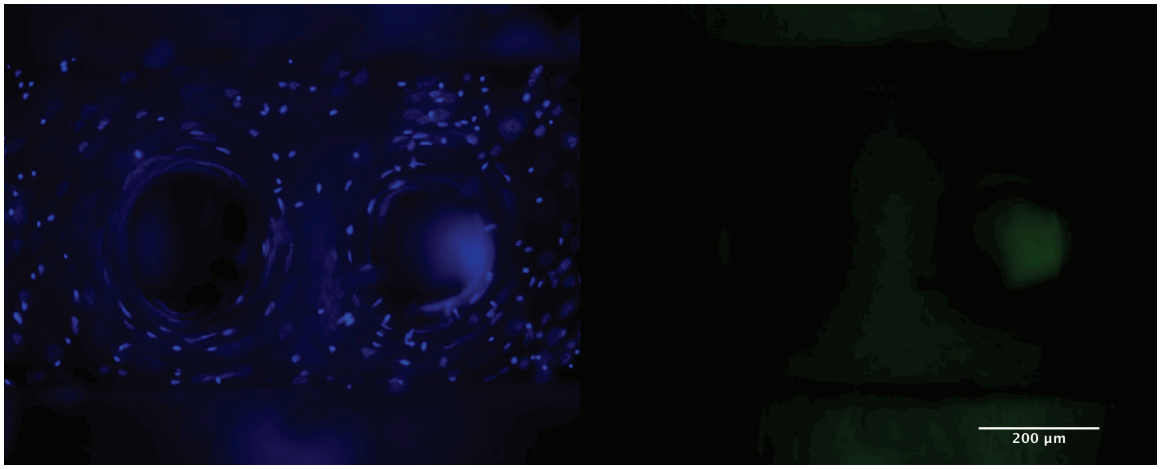

Figure 4-3: Epifluorescent images of preliminary microtissue attempts fabricated solely using 3T3 cells. The cells were stained with Hoechst (right) but did not express GFP (left). This was used as an indication that the cells died within the device.

Biocompatibility Tests

To investigate the culprit that lead to the cell death, GFP-labeled 3T3 fibroblasts in collagen gels were incubated with each component individually used in fabricating the actuators. Brass, PZT, Epotek 301 epoxy, conductive epoxy and cyanoacrylate glue each led to cell death (n=1).

Parylene Coating

Two possible methods of improving the parylene coating were investigated: 1) samples were silanize to improve parylene adhesion to oxidized surfaces; and 2) the parylene thickness was increased to prevent pinholes and improve its permeability. However, instead of fabricating several arrays of actuators to investigate these hypothesizes, simplified unimorphs, consisting of all the same materials used for the device, were used as substitutes. All samples underwent a biocompatibility test, like above, and a hydrolysis of saline bubble test. The biocompatibility test was used as an indication for cell survival, while the bubble test was used to examine the parylene coating for pinholes and areas of high permeability.

Table 4-1: A summary of hydrolysis of saline and biocompatibility results (n=1). Samples with 3um thick parylene did not produce any bubbles and were biocompatible, passing both tests.

Silanization	Thickness	Bubble Test	Biocompatibility
Silanized	0.35μm	Yes Bubbles	Not Biocompatible
	1μm	Yes Bubbles	Not Biocompatible
	3μm	No Bubbles	Biocompatible
Non-silanized	0.35μm	Yes Bubbles	Not Biocompatible
	1μm	Yes Bubbles	Biocompatible
	3μm	No Bubbles	Biocompatible

The results for the hydrolysis of saline bubble tests and the biocompatibility tests are summarized in Table 4-1. Samples that received the thinnest coating (0.35μm) failed both tests. Silanization at this thickness, however, did seem to show a slight improvement during the hydrolysis of saline bubble test as the location of bubble formation was localized only to the edges, whereas with the non-silanized sample, the bubbles formed everywhere on its surface. Somewhat surprisingly, the silanization step made no

difference for the thicker coatings. In fact the 1μm, non-silanized sample was biocompatible, whereas the 1μm, silanized sample was not biocompatible. It is difficult to explain this result, but a possibility was that the silanized sample might have had some dust or oil on its surface that prevented a flawless parylene coating from forming. Both samples that received a 3μm coating were biocompatible and did not form any bubbles during the hydrolysis of saline test, and therefore this thickness was selected for all future attempts at fabricating the device. Also because there did not seem to be any difference between silanized and non-silanized samples at this parylene thickness, this step was omitted.

Fibroblast Microtissue Formation

For all the following attempts at forming microtissues, the device consisted of 2mmx70μmx400μm (lxwxt) bimorph actuators with a 3μm thick parylene coating. The base was made out of clear PVC to limit cytotoxicity and allow for bright field cell imaging. A photograph of the device is shown in Figure 4-4a). In this device, the 3T3 cells survived at least up to four days and compacted into a 3D tissue with an even distribution of cells around the actuators. Epifluorescent images of the Hoechst-stained and GFP-labeled microtissues taken 4 days after the cells were seeded are shown in Figure 4-4b).

Although the cells compacted into tissues and showed strong attachment to the actuators, the tissues were also attached to the sides of the wells. Two methods to prevent the tissues from attaching to the sides of the wells were investigated: 1) increasing the treatment time with Pluronic F-127 to 5min since this step was meant to prevent protein

absorption into the PDMS; and 2) preferably parylene coating only the posts since this is not a prominent problem with the passive wells and parylene has previously been shown to have greater cell adhesion and protein absorption compared to PDMS (4). Unfortunately, neither of these solutions led to any difference in the tissues' appearance.

a)

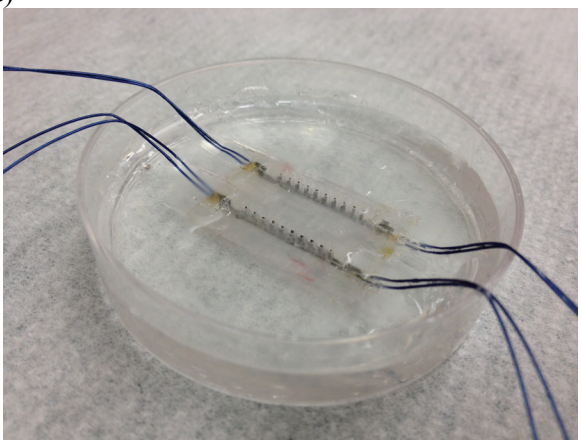

b)

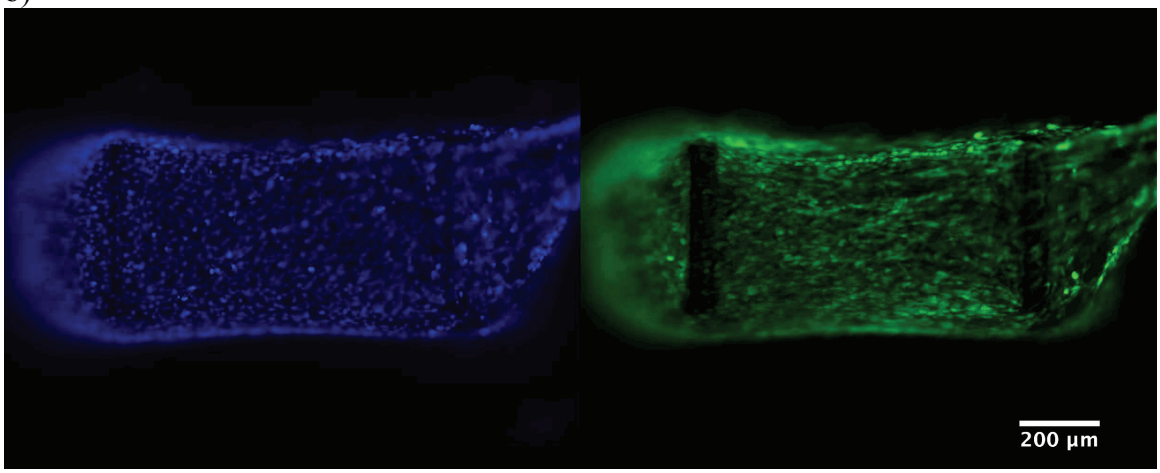

Figure 4-4: (a) A photograph of the final version of the device. It consisted of two rows of sets of bimorph actuators within PDMS wells. (b) Epifluorescent images of a representative microtissue fabricated with 3T3 cells using the final version of the device. The cells were stained with Hoechst (left) and expressed GFP (right), indicating that the cells survived for at least 4 days.

ASM/Fibroblast Microtissue Formation

Due to the success with fabricating solely fibroblast microtissues, I next investigated the formation of microtissues consisting of 80% ASM cells and 20% fibroblasts to create a model of airway smooth muscle. Similar to the fibroblast microtissues, initial attempts survived in the device and compacted into 3D tissues around the actuators but also had attachments to the sides of the wells. Since the volume of the wells was much greater than in the passive microtissue model, it was hypothesized that

a)

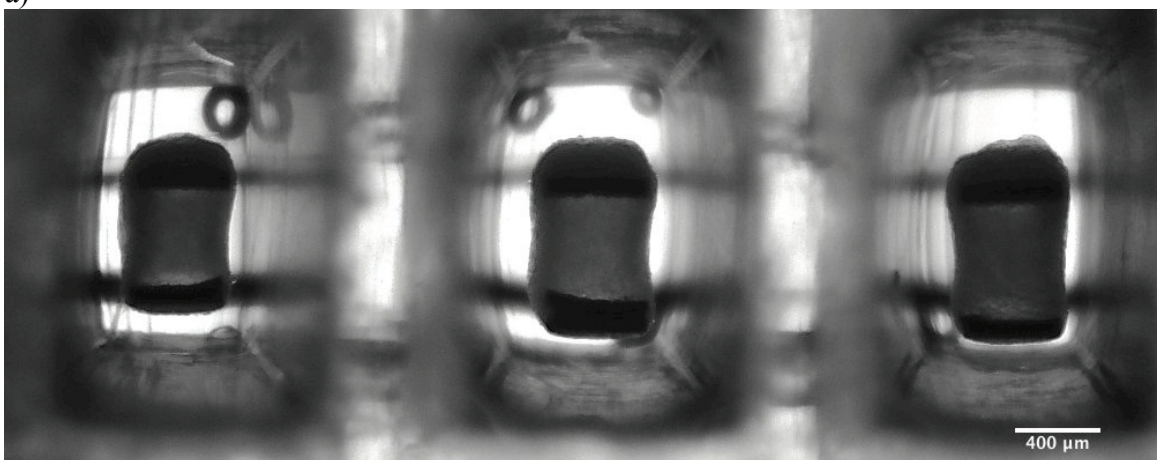

b)

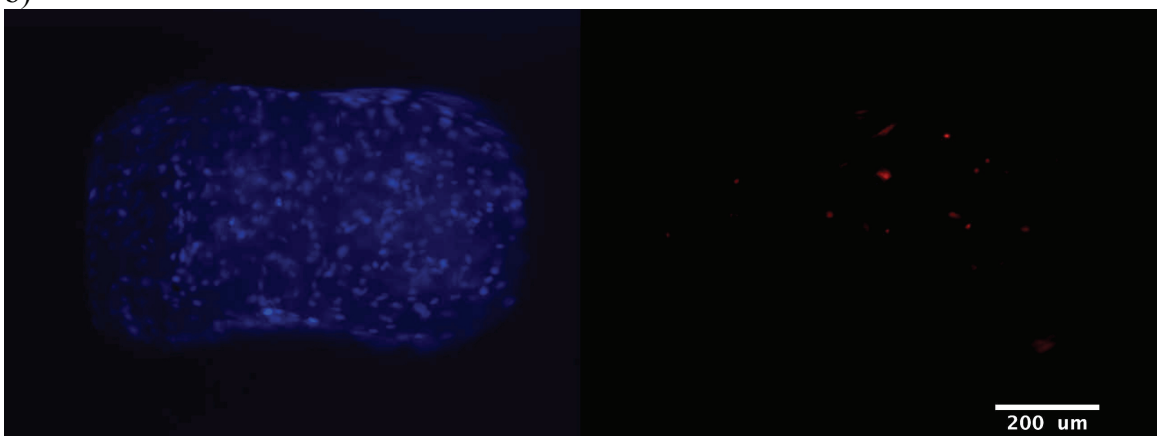

Figure 4-5: (a) A bright field image of an array of three ASM/fibroblast microtissues fabricated within the device. (b) A representative epifluorescent image of a Hoechst (left) and propidium iodide (right) stained microtissue. There was negligible cell death compared to the total number of cells within the tissue.

there was simply too much collagen for the cells to compact without attaching to the wells. Accordingly the collagen concentration was halved to test this hypothesis. At this concentration, the ASM/fibroblast microtissues still compacted around the actuators but without any attachments to the sides of the wells. A bright field image of an array of three tissues is shown in a). A representative epifluorescent image of a Hoechst and propidium iodide stained microtissue is shown in b). Compared to the total number of cells, the dead cells stained with propidium iodide were negligible.

Tissue Stiffness Measurements

In ASM/fibroblast microtissues, there was visible tissue tension when resting at baseline. Shown in Figure 4-6a), the actuators were capable of overcoming this tension to stretch the tissue at a peak deflection slightly less than when a tissue was not present ($n=6$, $p<0.01$). A linear regression analysis was performed to investigate changes in tissue stiffness with amplitude of tidal stretch. Shown in Figure 4-6c), imposing greater and greater stains caused a significant decrease in tissue stiffness ($R^2=0.48$, $p<0.01$) and at small strains ($<\pm1\%$) the baseline tissue stiffness was 20.58 ± 1.04N/m ($n=3$).

In addition to baseline measurements, microtissue stiffness was measured after incubations with a contractile agonist (KCl), a relaxant agonist (Forskolin), and an actin inhibitor (Cytochalasin D). Shown in Figure 4-7a), the actuators stretched the tissues under all pharmacological conditions at a peak deflection slightly less than when the tissue was not present ($n=8$, $p<0.01$). Shown in Figure 4-7b), the tissue stiffness significantly decreased in a strain dependent manner for all conditions ($n=4$, $p<0.01$). At small strains ($<\pm1\%$), the tissue stiffness following KCl (23.0 ± 2.0N/m) was measurably

greater than after forskolin (16.9± 5.4N/m) and cytochalasin D (16.8±5.7N/m) (n=4, p<0.1).

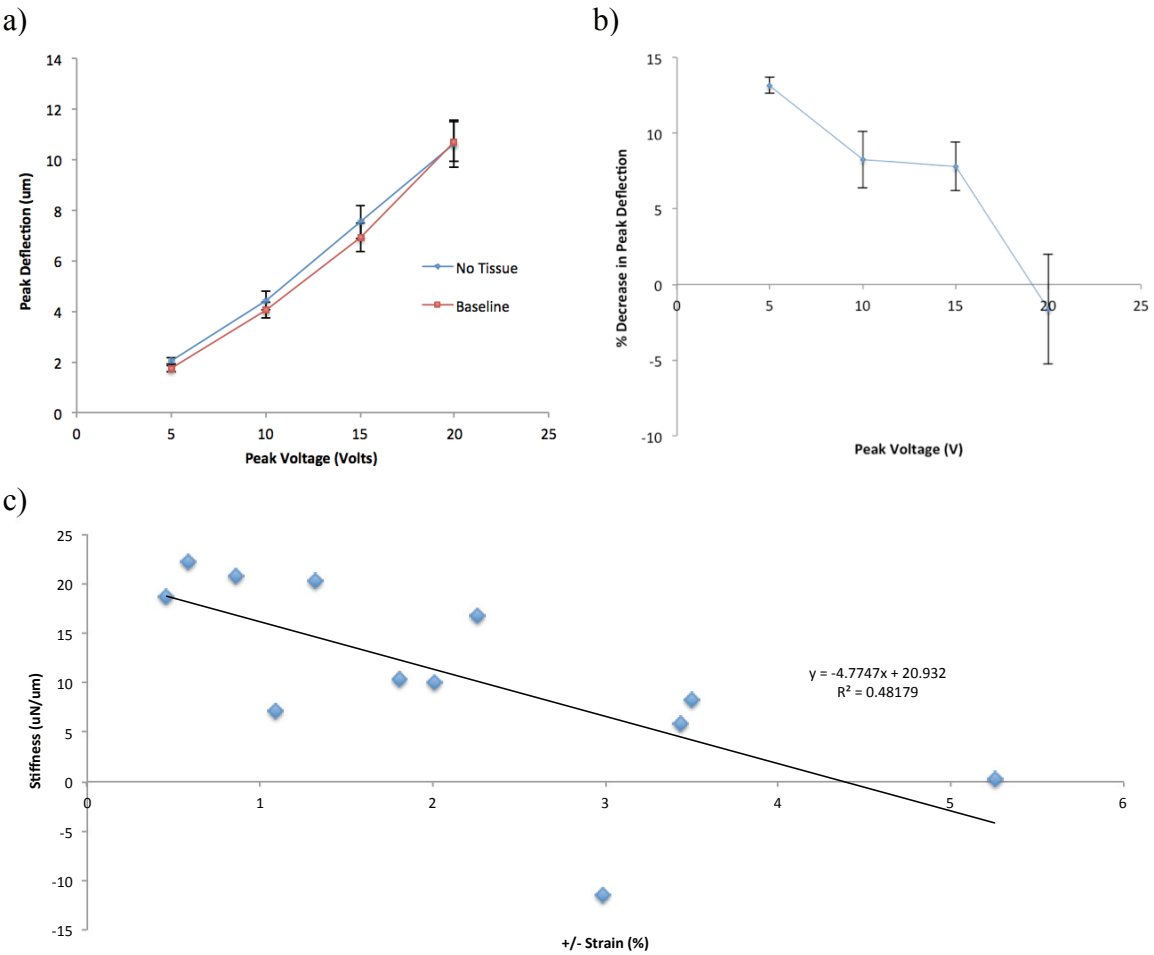

Figure 4-6: (a) Peak actuator deflections with and without a tissue (n=6). (b) The percent decrease in peak deflection with the tissues. Due to their stiffness, the presence of the tissues resulted in a slight decrease in actuator deflection (p<0.1). (c) Furthermore, the tissues stiffness significantly decreased in a strain dependent manner (n=3, p<0.01).

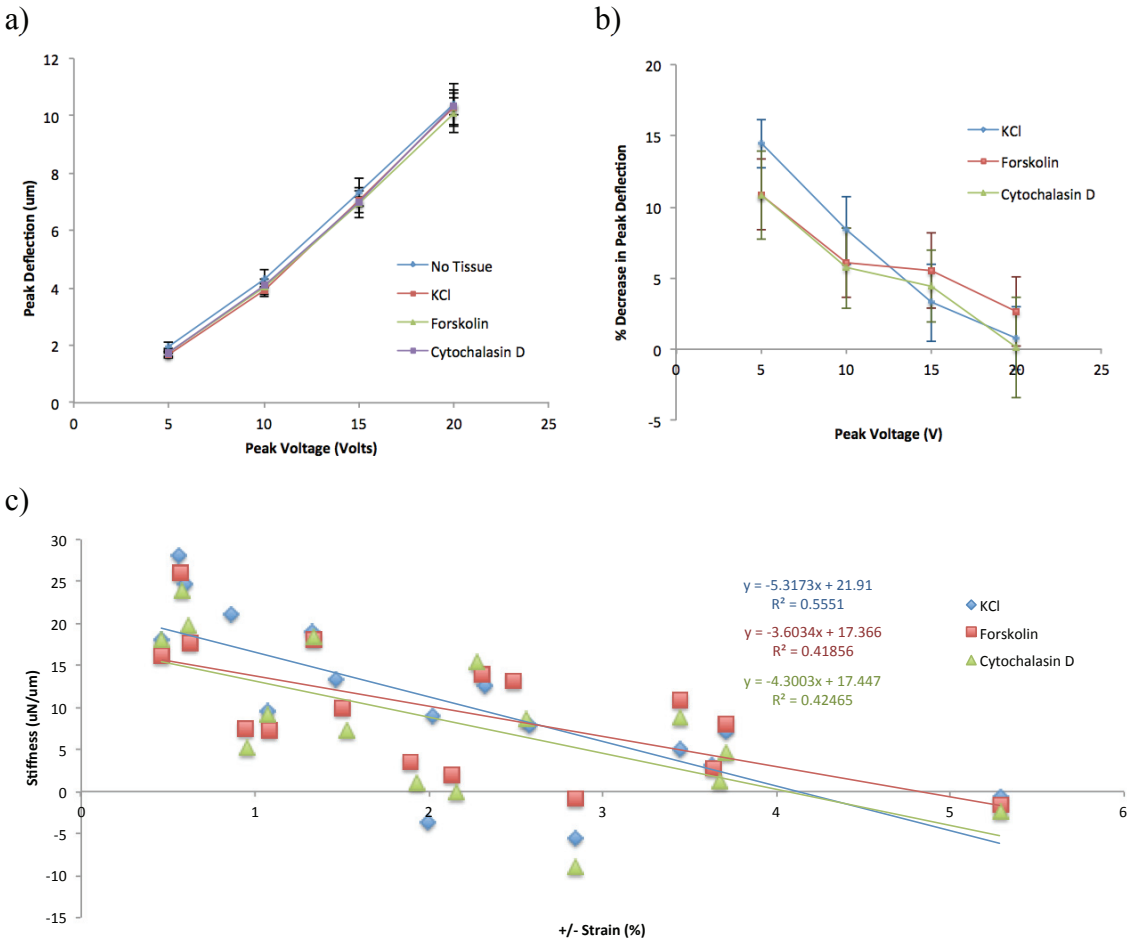

Figure 4-7: (a) Peak actuator deflections without and with a tissue under different pharmacological conditions (n=4). (b) The percent decrease in peak deflection with the tissues for the different pharmacological conditions. (c) For all conditions, the tissue stiffness decreased in a strain dependent manner. At small strains, tissue stiffness following KCl was measurably greater than after forskolin and cytochalasin D (n=4, $p<0.1$).

Storage and Loss Moduli

Fraction changes between the storage and loss moduli of the tissues were investigated by examining the phase between the measured strain and the applied input voltage. Shown in Figure 4-8a), the strain slightly lagged behind the input voltage.

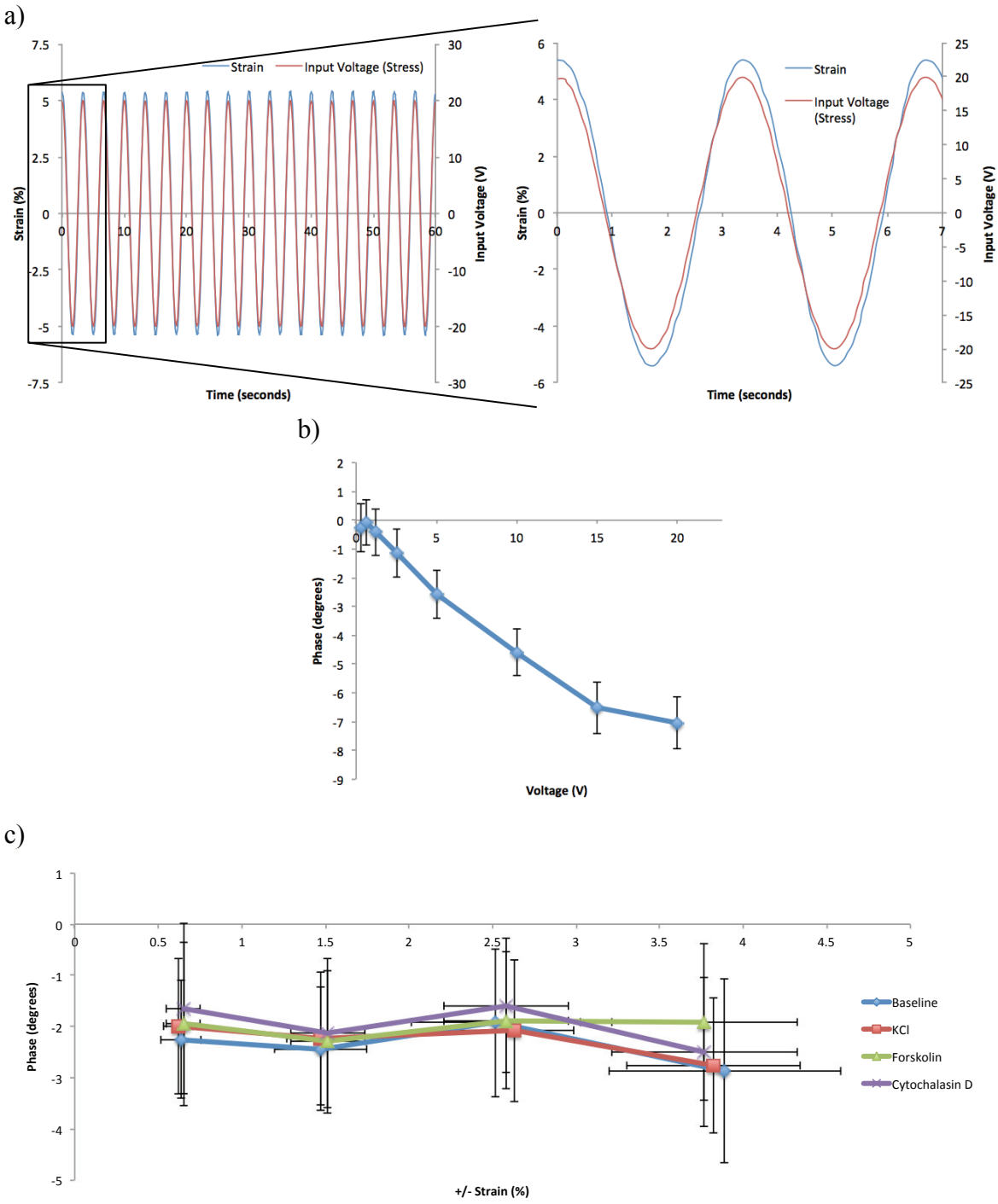

Figure 4-8: (a) Representative strain and input voltage (stress) data (left). A magnified view reveals a small phase shift (right). (b) The correction applied to account for the change in phase created by the actuators. (c) The phase between the corrected stress and strain did not change in a strain dependent manner nor was affected by pharmacological conditions (n=4).

The phase was corrected for lags caused by the finite electrode resistance, the extrinsic piezoelectric effect, and/or the software used for data collection. The correction is shown in Figure 4-8c). Near 0V, the phase between actuator deflection and input voltage was close to 0^o but as the voltage increased, the deflection lagged the input voltage. The phase between the corrected applied stress and measured strain for the tissues at increasing amplitudes of strain and under the different pharmacological conditions is shown in Figure 4-8d). The presence of the tissue caused roughly a 2^o phase lag, which was not affected by the magnitude of the strain or the pharmacological conditions. There was a considerable amount of variability in the measurements of phase compared to the magnitude of the lag. By comparing the responses within the individual tissues (data not shown), this variability was not caused by a limited resolution of the deflection tracking but rather is explained by the variability of the actuators and tissues.

4.4 Discussion

The main finding from this section of my thesis was that microtissues fabricated using fibroblast cells alone, and 20% fibroblast and 80% ASM cells could by formed in the device and survive with negligible cell mortality. Furthermore the device used a microarray format that could enable high-through experiments on living cells in a controllable 3D environment during acute or chronic periods of oscillatory stretch. Also the entire tissue can be stained and imaged for markers of cellular phenotype, making it an extremely compelling, physiologically relevant system to probe cellular mechanics.

To achieve these feats using materials that would have otherwise resulted in cell

death, the device was coated with 3μm thick parylene. This strategy of using a barrier for biocompatibility does, however, lend itself to the possibility of failure if the barrier becomes damaged. Another, possibly better, strategy would be to start with biocompatible materials. There have been recent claims of lead-free piezoelectric ceramics with properties comparable to that of PZT (63), however these materials are still in the development stage and are not commercially available. PVDF, on the other hand, is commercially available in thick films or may be formed from a melt or from cast solution. Also, as already mentioned in the second chapter, PVDF is far more compliant compared to PZT, and therefore would allow easier measurement of contractile force production and changes in tissue stiffness.

Nevertheless, even with the present actuator design, I managed to measure the stiffness of an array of microtissues with reasonable success. The tissues' stiffness were calculated using the values of peak actuator deflection when the tissue was and was not present, and the theoretical actuator stiffness in a mathematical model of actuator dynamics with elastic loading. Using this method to measure tissue stiffness did have a few limitations. First, the model assumed that the thickness of the tissue was negligible in comparison to the length of the actuators so that the tissue would receive roughly the same amplitude of strain throughout its thickness, and the force it produced to oppose the actuator deflection occurred solely at the tips of the actuators. In all likelihood, the tissue thickness was not negligible and the use of this model underestimated the tissue stiffness. However, the portion of the tissues that were closest to the tip of the actuators did receive the largest amplitude of strain, and theoretically contributed the largest moment of force to oppose the actuators, validating this approach.

Another limitation to this approach to measure tissue stiffness was that it greatly

depended on the error in the measurements of actuator deflection. As shown in Figure 4-9a), the reproducibility of measurements tissue stiffness improved with the amplitude of strain, and reached a reasonable value (<±10% initial tissue stiffness) at ±0.5% strain. Moreover, this error in deflection tracking was likely the cause of the negative measurements of stiffness in Figure 4-6 and 4-7.

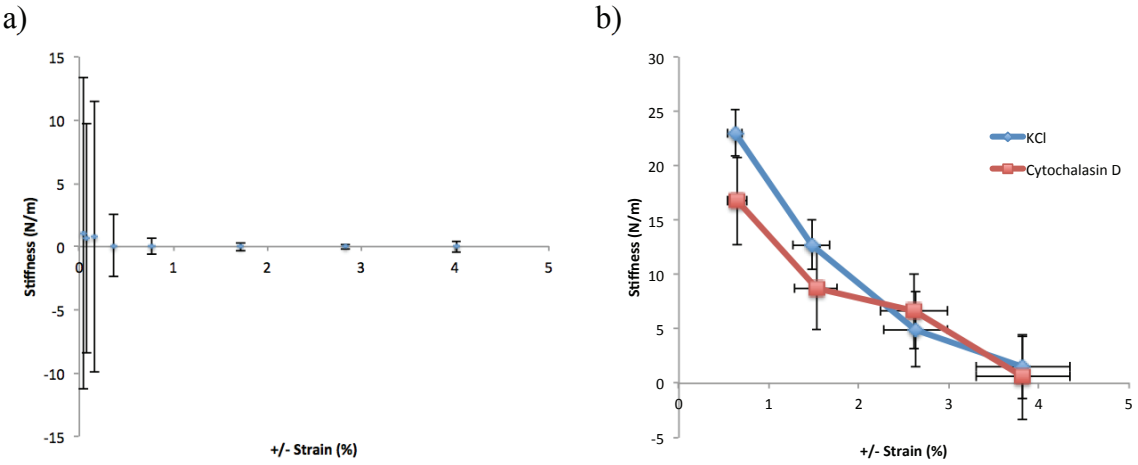

Figure 4-9: (a) The noise floor for measurements of stiffness. Error bars are the standard deviation (n=6) and reach an acceptable value at strains >±0.5%. (b) The average stiffness-strain responses for KCl and cytochalasin D (n=4).

Preliminary results showed that the tissues' stiffness decreased in a strain amplitude dependent manner. Although the tissue stiffness is determined by the mechanical properties of both the cells and ECM, this finding is similar to previously published results using maximally contracted isolated sections of bovine tracheal smooth muscle (80% decrease in stiffness at an oscillatory strain amplitude of ±4%) (14), and single canine cell culture (66% decrease in stiffness at an oscillatory strain amplitude of 10%) (40). Furthermore it is consistent with the current understanding that ASM cells behave as SGMs and respond to stretch by immediate fluidization of their cytoskeleton

(29) (54), and reflects the ability of an acute oscillatory stretch, delivered by a deep inspiration, to dilate the airways in healthy subjects (11). Interestingly, the study on single cell culture also showed that prior chronic uniaxial stretch caused the cells to quickly recover their stiffness when the amplitude of strain was decreased after an acute period of large oscillatory stretch. This result reflects the inability of an asthmatic to maintain dilated airways following a deep inspiration. Although I did attempt to study the recovery period (data not shown), it was done at a strain that did not give reproducible results. This then should be a focus for future investigations.

To test the robustness of the device's ability to measure changes in tissue stiffness, the tissues were subjected to mechanistically distinct pharmacological agents. As expected, a contractile agonist led to an increase (12% compared to baseline) in stiffness when measured at small strains, while both a relaxant agonist and an actin polymerization inhibitor decreased (18% compared to baseline) tissue stiffness. The magnitude of the respective responses, however, were much lower than previously published changes in stiffness in 2D cultured ASM cells or changes in tissue tension in ASM 3D microtissues (61). The exact reason for this disparity is unknown but it may have possibly been caused by poor cellular alignment, lower collagen and cell density, and/or the state of the cytoskeleton at the measured strain.

Under all pharmacological agents the stiffness decreased in a strain dependent manner. The average tissue response to KCl and cytochalasin D is shown in Figure 4-9b). At low strains, there appeared to be a separation between the responses, however, at large strains, the responses converged. These results can also be explained by the fluidization of the cytoskeleton. At low strains, the cytoskeleton is mostly intact, and therefore, the cells can contract and increase their stiffness in response to KCl, or relax and decrease

their stiffness in response to cytochalasin D (or forskolin). However, at large strains, the cytoskeleton is almost completely fluidized and so the delivery of a contractile agonist or relaxant agonist has no affect. This finding reflects the ability of a deep inspiration to reverse airway narrowing after the inhalation of a bronchoconstrictor in healthy subjects (11).

The fraction between the loss and the storage moduli of the tissues was investigated through examining the phase lag between the applied stress (input voltage) and the measured strain (imaged actuation/tissue motion). Although the tissue stiffness decreased, the amplitude of strain did not affect the phase. This invariant phase response might be explained by the relatively high stiffness of the actuators, making their motion insensitive to the internal frictional stresses in the tissue. However, there did seem to be an offset of roughly 2^{o} caused by the tissue. Another possibility is that the fraction between the storage and loss moduli simply did not change with strain or the pharmacological conditions. This finding is consistent with the generally agreed paradigm that the relationship between elastic and frictional stresses is nearly invariant in soft biological tissues and living cells (9, 10). However, since the measured phase depended on the relative stiffness of the tissues and actuators, and the results suggested that the tissues stiffness decreased in a strain dependent manner, then there could have been an increase in the fraction between the storage and loss moduli. Indeed, a strain dependency of phase has already been documented, albeit small, in ASM cells (54) and tissue strips (14, 15). Perhaps in future work, tissue and actuator dynamics could be modeled together so that this phase can be better used to investigate changes in the elastic and internal frictional stresses in the tissues.

In conclusion, the findings from this chapter suggest that this *active* microtissue

model can be used to measure the effect of acute oscillatory stretch on the state of the cellular cytoskeleton. It can also be used to measure the contractile response through changes in tissue stiffness. The strain dependency of tissue stiffness was quite remarkably, especially after the delivery of KCl. This ability of strain to decrease tissue stiffness and completely reverse cellular contractile force further emphasizes that out of all known bronchodilator agents, a simple stretch is the most efficacious (18).

Chapter 5: A Self-Sensing Approach for the Measurement of Actuator Deflection and Tissue Properties

5.1 Rationale

In present cell culture stretching devices, the contractile function of ASM cannot be directly measured, but instead must be inferred from proliferation, cytoskeletal organization and contractile specific protein expression. Since the relation between these parameters and active force development is not always clear, a device capable of measuring contractile function directly has a significant advantage. Furthermore, by simultaneously measuring cantilever deflection and force during sinusoidal stretching, tissue properties, such as dynamic tissue stiffness, may be elucidated, as previously shown in the fourth chapter.

Several external sensors have been developed to measure the applied force and deflection of piezoelectric actuators. However, none of these external methods are particularly well suited for this research due to dimension restrictions and precision limitations. Instead, I hypothesized that the self-sensing method, where the actuator performs simultaneously as its own sensor, may be a suitable alternative. Self-sensing is based on converting charge into a measurable voltage from which the deflection and applied force can be estimated. There are several advantages to the self-sensing method relative to the use of external sensors. Among them, the self-sensing method allows a consistent reduction in the cost by eliminating expensive sensors while the attained resolution can be submicrometric and comparable to external sensors.

While not a new concept for vibration control or damping in piezoelectric actuator

applications, self-sensing was just recently adapted for quasistatic (more than hundreds of seconds) displacement measurement for piezoelectric cantilevers with reasonable accuracy (27). Since the generated charge on the actuator is related to the applied voltage, and as well, the applied force, this method of self-sensing was later extend to track actuator deflection and force measurements simultaneously (26, 27). In this section of my thesis, I attempted to apply this method of self-sensing for tracking the deflections of my bimorph actuators and discuss its potential to measure changes in tissue force and stiffness.

5.2 Methods

Electronics Fabrication

To measure charge, a precise current integrator (charge amplifier), as depicted in Figure 5-1, was built with the expertise of Andre Bezanson, a PhD. candidate in the school of biomedical engineering, and Pascal Poirier, an electrical engineer at Thoracics. The actual circuit diagram and PCB layout are included in appendix VII.

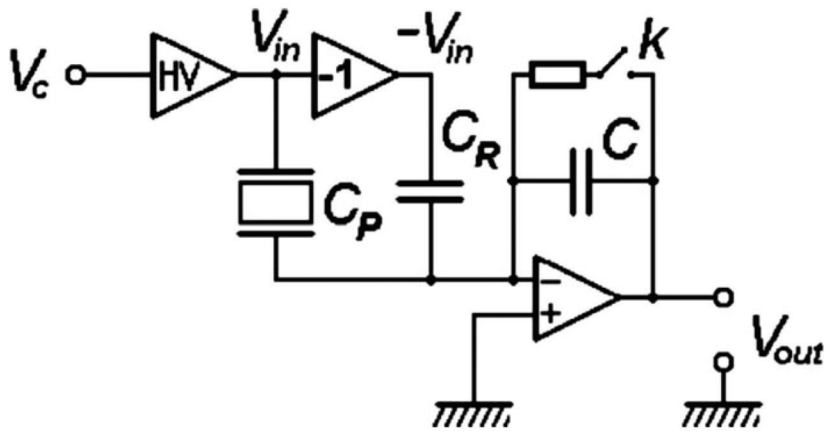

Figure 5-1 (Modified from Ivan *et al.* 2009): The electronic circuit schematic of a charge amplifier

The input signal, V_{in}, is applied to the piezoelectric actuators, C_P, and is also inverted and applied to a reference capacitor, C_R. According to the second Kirchoff law, C_R "absorbs" a significant part of the charge from the piezoelectric actuators allowing for the output to saturate at a higher V_{in} value while preserving the same sensitivity.

The feedback capacitor, C, integrates the difference in current from C_p and C_R due to external force variation and applied voltage. It works by using a capacitive feedback loop with an operational amplifier to "balance out" or "null" the input charge. The feedback signal is therefore a measure of the input charge and can be converted into a readable voltage, V_{out}. The electromechanical relay-switch, k, drains the charge on the feedback capacitor to prevent saturation of the output signal.

The operational amplifier (OPA111BM, Burr-Brown Corporation, Tucson, AZ) used in the charge amplifier was the same model used in previous attempts of self-sensing (26, 27). It has a very low bias current and noise, which makes it suitable for this application. The feedback and reference capacitors were chosen based on their high leakage resistance of 500 GΩ. When calculating deflection or force, the effect of this leakage resistance was assumed to be negligible in comparison to the leakage resistance of the piezoelectric actuator.

Experimental Setup

The deflection of the posts was captured with the same camera setup as used in the second chapter. The digital to analog convertor on the NI-6035E card was used as the voltage inputs for the actuators and the reference capacitor. The inputs were driven at the

same amplitude and frequency except with an 180^{o} phase shift relative to one another. The output and the input signals were acquired with the NI-6035E card with a sampling frequency of 1000Hz, and then averaged down to a sampling frequency of 15Hz to match the speed of the camera.

Identification of Variables

In the method of self-sensing presented in (26, 27), the integrated electrical current (i.e. the electrical charge), is compensated against the drift from the amplifier's bias current (i_{bias}) and leaking resistance of the piezoelectric actuators (R_{FP}). Their method also includes a compensation for dielectric absorption nonlinearities (Q_{DA}) when a DC signal is applied after a step in voltage; however, as the device will always be driven with a low frequency (0.3Hz) sinewave this compensation was not necessary.

From the output signal, the free deflection, d_{est}, was calculated according to the following equation:

$$d_{free\_est} = -\frac{C}{\mathrm{A}}V_{out} + \frac{C_R}{\mathrm{A}}V_{in} - \frac{1}{R_{FP}\mathrm{A}}\int V_{in}(t)dt - \frac{1}{\mathrm{A}}\int i_{bias}(t)dt \quad (36)$$

where $A = \frac{C_p}{\beta}$

This equation can be derived by substituting equation (1) into equation (2) with the condition that F=0, and then including the compensations for leakage resistance, bias current and the cancelled charge by C_R.

The capacitances were verified with a digital scopemeter. As for the other variables, the steps for their identification follow:

1) Under F_{ext}=0 and V_{in}=0, i_{bias} of the amplifier was derived from the rate of

change of V_{out} and the known value of C.

$$i_{bias} = C\frac{d}{dt}(V_{out}(t)) \quad (37)$$

2) Under F_{ext}=0 and a constant applied voltage (V_{in}≠0), R_{FP} was derived from i_{bias} (identified above) and the rate of change of V_{out} after several hundred seconds to eliminate the influence of residual creep.

$$R_{FP} = \frac{V_{in}}{C\frac{d}{dt}(V_{out}(t)) - i_{bias}} \quad (38)$$

3) Under F_{ext}=0, A was derived using the measured value of actuator deflection, d, and V_{out} immediately after applying a step in the V_{in} in the following the equation:

$$A = \frac{(-CV_{out} + C_R V_{in})}{d} \quad (39)$$

5.3 Results

Test Load

To ensure that the charge amplifier was correctly integrating current, a test capacitor (6800pf) was first attached to its input in place of the piezoelectric actuators, C_p. A step voltage was then applied only to this test capacitor while the voltage to the reference capacitor was kept constant. The resulting step in the output voltage was immediately measured. Shown in Figure 5-2a) is the relationship between the step in the input voltage and the measured step in the output voltage. Linear regression gives a near prefect fit (R^2=0.99977) passing close to the origin with a slope (-0.67)

approximately equal to the capacitance ratio of the test (6800pf) and feedback (10000pf) capacitors. In Figure 5-2b), this same data is expressed as charge. The line of best fit has a slope nearly equal to negative one. This finding indicated, as expected, that the charge at the input of the charge amplifier was exactly balanced by the charge on the feedback capacitor, and therefore the amplifier was correctly integrating current.

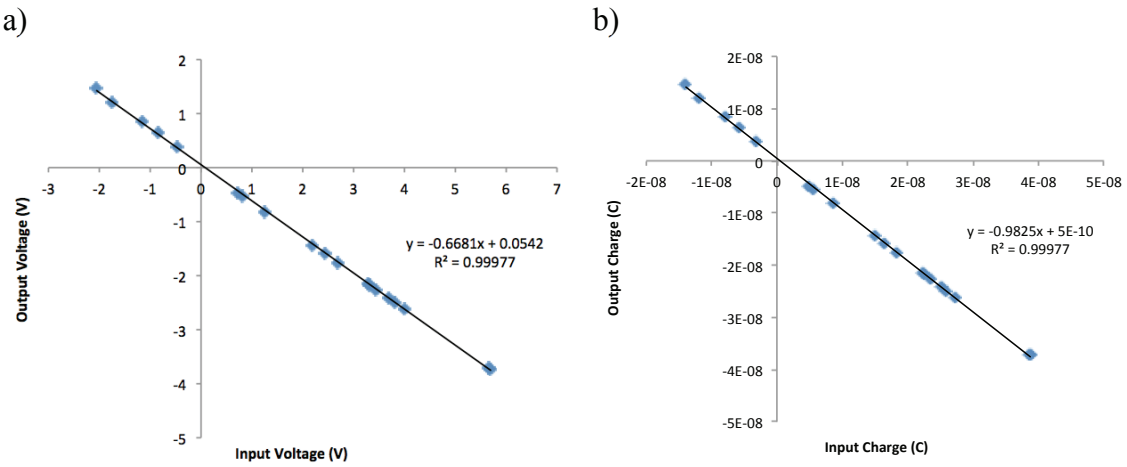

Figure 5-2: Steps in input voltage were applied to a test capacitor while the output voltage from the charge amplifier was measured. (a) The relationship between the step in the input voltage and the step in the output voltage. (b) The same data is expressed as charge. Linear regression gives nearly a perfect fit. Furthermore, the slope shows that the change in charge on the test capacitor was exactly balanced by the change in charge on the feedback capacitor.

Identification of Constants

With zero input voltage, the output voltage drifted at a rate solely determined by the bias current of the op-amp as shown in Figure 5-3a). From this figure, the i_{bias} was calculated to be -11pA.

When an input voltage was applied, the output voltage drifted at a rate determined by the bias current of the op-amp and the leakage resistance of the actuators. Shown in Figure 5-3b) is the linear relationship between the drift in the

output, expressed as current, at different input voltages. According to Ohm's law (i.e. $V = IR$), the inverse of the slope of that relationship corresponds to the leakage resistance, which was calculated to be 21.43 GΩ. The y-intercept of that relationship is also, as expected, in close agreement with the bias current measured with zero input voltage.

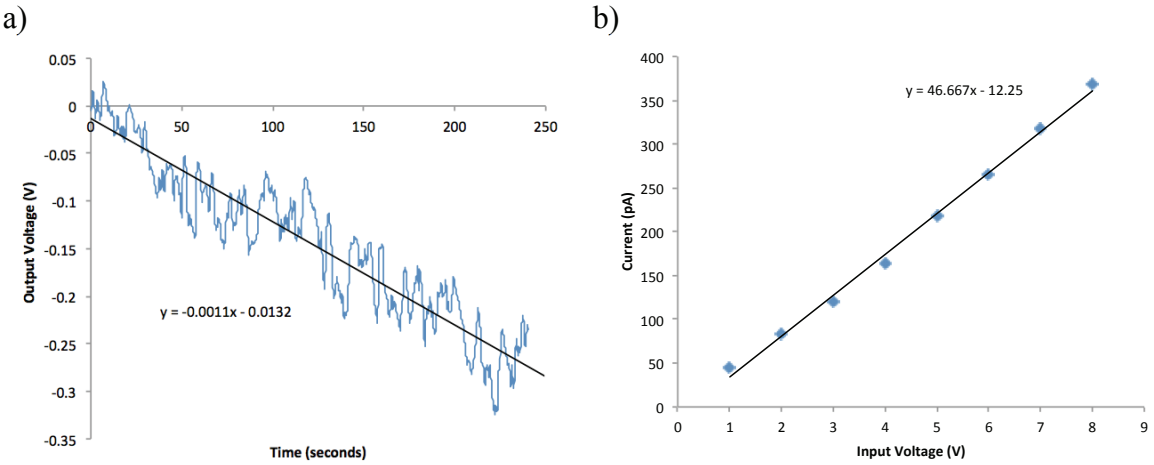

Figure 5-3: (a) The drift in the output voltage due to the bias current of the amplifier. (b) The relationship between the rates of drift in the output voltage, expressed as current, and the input voltage. The inverse of the slope of this relationship is the leakage resistance of the actuators.

The A constant was determined by measuring the deflection of the actuators and output voltage immediately following a step in the input voltage. Using the data shown in Figure 5-4, the A constant was calculated to be -1.296e-8C/μm. The measured value of the A constant was not equal to the ratio of C_p/β because of the extra capacitance of the clamped portion of the actuator in the base.

a)

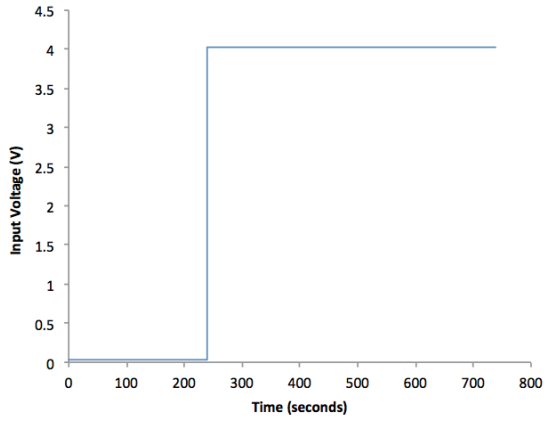

b)

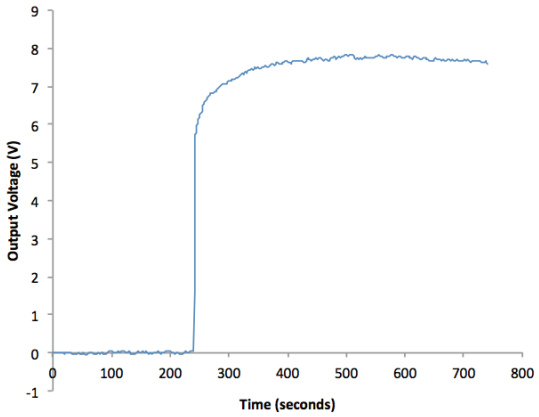

c)

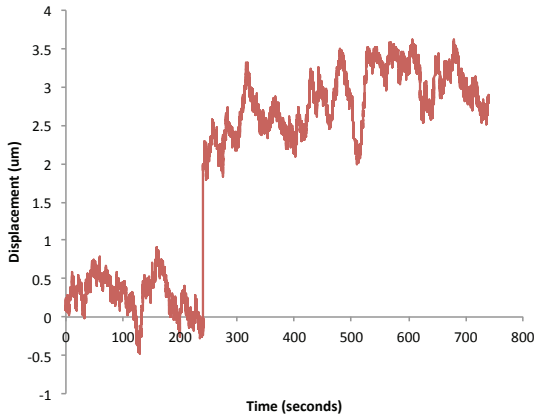

Figure 5-4: The A constant was calculated by applying (a) a step input voltage and immediately measuring (b) the step output voltage and (c) the actuator deflection. Note the noise in the output voltage is much less than the noise measured by the video tracking method.

Verification of Self-Sensing for Free Deflection

To test the accuracy and resolution of the self-sensing method, the output signal was collected for 60 seconds while the actuators were driven with a 5V, 0.3Hz sinusoidal wave. Using the identified constants, summarized in Table 5-1, the output signal was compensated for the bias current, the leakage resistance and the cancelled charge by C_R. The output voltage was then converted into a displacement using the measured A constant.

Table 5-1: A summary of measured constants used in the algorithm to determine free deflection

Variable	Measured Value
C_P (f)	19260e-12
C_R (f)	6800e-12
C (f)	10000e-12
i_{bias} (A)	-11e-12
R_{FP} (Ω)	2.143e10
A (C/um)	-1.296e-8

The compensations, and the measured deflection from the charge amplifier and the video tracking method are shown in Figure 5-5. The drift caused by the bias current was small because of the high quality operational amplifier. The effect of the leakage resistance was also small because of the high quality actuators, low input voltage, and the relatively short period of oscillation. The leakage resistance also accounted for a slight drift in the output signal because of a small offset in the input voltage. Nevertheless, the calculated deflection from the self-sensing method nearly matched the measured deflection with the video tracking method.

The Fourier transforms for the self-sensing and video tracking methods are shown in Figure 5-6. The peak deflection attained with the charge amplifier method was 2.666μm, whereas the peak deflection attained with the video tracking method was 2.657μm, giving an accuracy of 0.34%. Moreover, the SNR for the self-sensing method was 53.67dB, which would theoretically allow for displacements as small as 5.5nm (71pC) to be tracked.

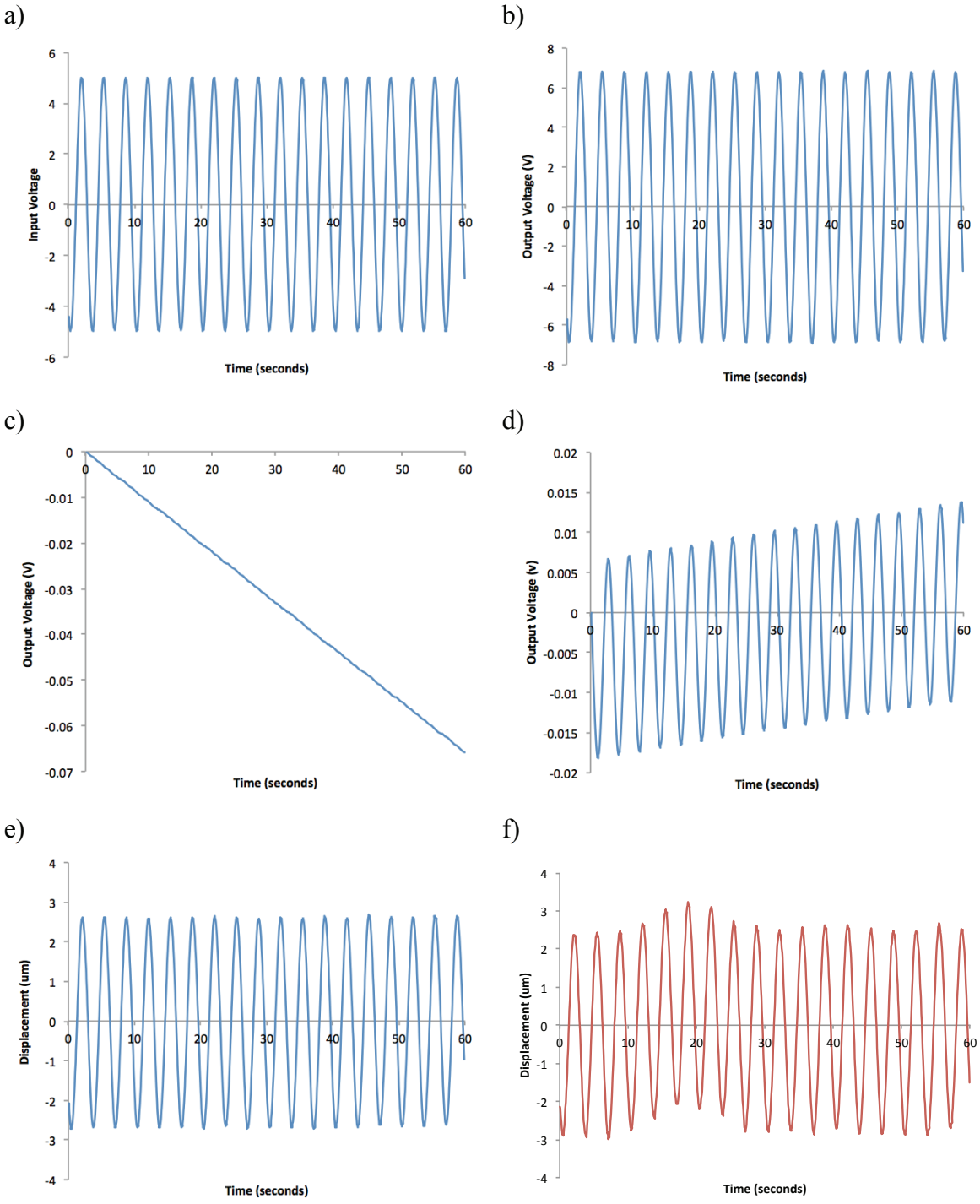

Figure 5-5: (a) A ±5V, 0.3Hz sinewave was applied to the actuators. (b) The output voltage was measured and compensated for (c) the bias current of the operational amplifier, and (d) the leakage resistance of the actuators. The deflection of the actuators measured with (e) the self-sensing method agreed well the deflection measured with (f) the video-tracking method.

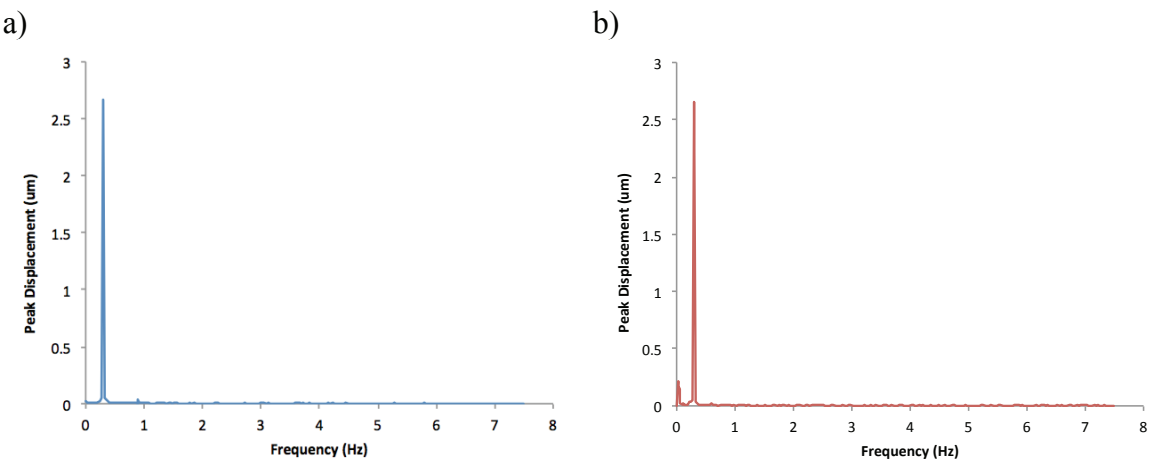

Figure 5-6: The measured actuator deflection with (a) the self-sensing method, and (b) the video-tracking method expressed in the frequency domain. The deflections agreed well with one-another at the fundamental frequency, however the noise floor was much lower with the self-sensing method.

Using Generated Charge to Measure Force

To examine the force sensing capability of the device, a uniformly distributed load was applied by gently blowing on parylene-coated actuators while tracking the tip deflection and generated charge. With zero applied voltage, the tip deflection and generated charge when an external pressure is applied can be described by the following set of equations

$$d = \frac{3s_{11}^{p}L^4}{2t^3}P \quad (40)$$

$$Q = \frac{d_{31}wL^3}{2t^2}P \quad (41)$$

These equations can be rearranged to solve for the applied pressure

$$P = \frac{d}{\frac{3s_{11}^{p}L^4}{2t^3}} \quad (42)$$

$$P = \frac{Q}{\frac{d_{31}wL^3}{2t^2}} \quad (43)$$

where $Q = CV_{out} + \int i_{bias}(t)dt$.

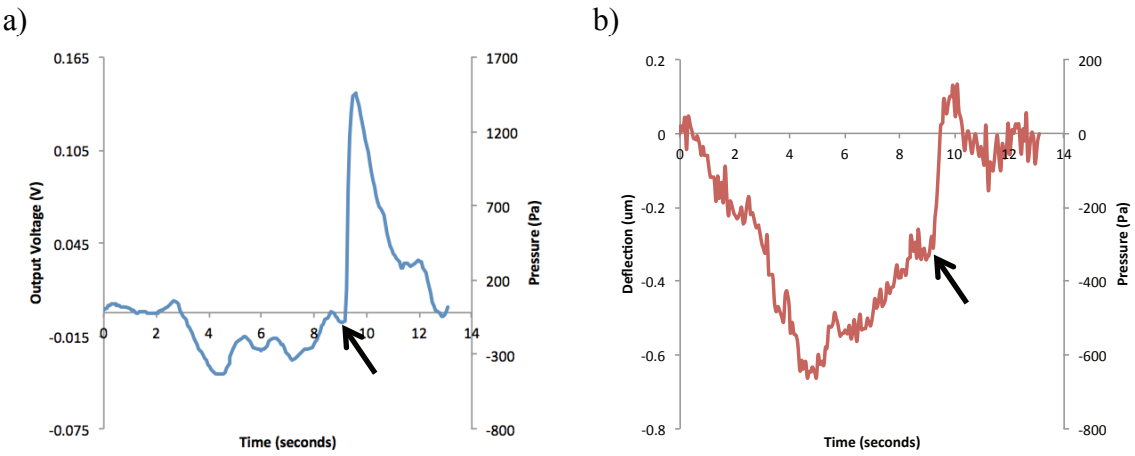

Figure 5-7: To investigate whether the generated charge could be used to measure force, the actuators were uniformly loaded by gently blowing on them. (a) The measured output voltage and corresponding calculated pressure from the charge amplifier. (b) The measured deflection and corresponding calculated pressure from the video-tracking method. The arrow indicates the start of blowing.

Shown in Figure 5-7**,** is the measured output voltage from the charge amplifier, the measured tip deflection from the video-tracking method and the calculated applied pressures from both methods. Upon the start of blowing, denoted by the arrow, there was a sudden peak in the output voltage and tip deflection. However, the calculated pressure from the charge amplifier method (1515Pa) was much higher than the calculated pressure from the video-tracking (471Pa) method.

5.4 Discussion

The main finding from this portion of my thesis was that the self-sensing method could be used to track the deflection of my actuators. Self-sensing has many benefits over the video-tracking methods described in chapter 3, which include the ability to track the

average peak deflection without having to image each individual cantilever. The resolution attained with self-sensing was equally as good, or even better than, the resolution attained with the video-tracking methods, allowing for very small deflections to be tracked. Furthermore, the accuracy of the self-sensing method was 0.34%. This was not surprising since Ivan *et al.* (27) have already shown that self-sensing is capable of achieving 0.55% peak-to-peak error when tracking a quasistatic deflection of piezoelectric actuators for more than 1000 seconds.

Because the design of the actuators changed greatly throughout this thesis, their capacitance was much higher than originally expected, and so more charge was generated at a given input voltage. As a consequence, with the chosen values of C_R and C, the output of the amplifier saturated at an input voltage well below the necessary value to attain the ±5% tissue stretch. Luckily C_R and C can easily be replaced. A closer matching of C_R to C_p would allow for a higher input voltage while attaining the same sensitivity but with loss in SNR (i.e. resolution). On the other hand, increasing C would also allow for a higher input voltage but with a loss in sensitivity. These factors can be weighed to optimize the performance of the charge amplifier for a specific application.

It was also found that the charge amplifier was capable of detecting an external pressure through integrating the current (i.e. electrical charge) when zero voltage was applied. However, the calculated value for pressure did not agree with the calculated value based on the video-tracking method. A possible explanation was that the piezoelectric and/or mechanical constants for the actuators might not have matched the theoretical values used for the calculations of pressure. This is strong possibility since the measurements of deflection and stiffness discussed in the second chapter did not agree with the theoretical values either. Another possibility was that the deflection of the

actuator captured with the video tracking method was not representative of the entire sample. Yet another possibility was that some of the deflection captured by the video-tracking method was lost in the transient low-frequency noise or the frame-rate of the camera was not quick enough to accurately capture the motion. A final possibility was that the pressure measurement with the charge amplifier might have simply been an artifact caused by electromagnetic interference from a magnetic (and electrical) field generated by the motion of charged particles in the air while I was blowing. Nevertheless, the use of piezoelectric actuators to detect external forces is supported by theory and has routinely been used in several different applications so this finding should not be much of a concern.

The question remains whether this method can be used for measuring changes in tissue force and stiffness during chronic oscillatory stretch. Shown in Figure 5-8a) is the theoretical change in charge and deflection offset for actuators of different thicknesses with a 20μN tissue contraction. Thinner actuators will have a larger change in charge and deflection offset, and thus, are more sensitive for measurements of tissue force. However, the ability to manufacture much thinner actuators to measure tissue force is limited by the methods and materials used for fabrication. Nevertheless, a 70μm thick, 2mm long actuator will have a deflection offset of 92nm and a charge offset of 7.84pC. These numbers are too small to be measured with the video-tracking method because of interfering low frequency noise, whereas for the charge amplifier, the measurement would be greatly dependent on the accuracy for the compensations of drift caused by the bias current and leakage resistance. Furthermore, since a full contraction occurs over several minutes rather than it being a sudden event, the charge generated by the change in offset position may leak out during the contraction, preventing any measurement of the

contractile force.

Instead of measuring static tissue force, an alternative approach would be to measure dynamic tissue stiffness, like I have done in chapter four. Substituting equations (12) and (13) into equation (2), the peak charge while stretching an elastic tissue is given by:

$$Q = \beta\left(-\frac{E_t A}{l_o}\right)\left(\frac{\beta V}{1+\alpha\left(\frac{E_t A}{l_o}\right)}\right) + C_p V_{in} \quad (44)$$

Shown in Figure 5-8b) is the effect of the presence of an elastic tissue on the theoretical peak charge for a 2mm long actuator with different thicknesses. Again, thinner actuators are more sensitive to the presence of the tissue, and thus, are favoured for measuring stiffness. Nevertheless, the presence of an elastic tissue will decrease the peak charge of a 70μm thick, 2mm long actuator by 6.95pC. This is equivalent to a decrease in peak deflection of 81nm, which is well within the theoretical resolution of the video-tracking method but for real-time chronic investigations into tissue mechanical properties, ideally this method would be avoided. The charge amplifier method, on the other hand, is perfectly suited for this application. Although this decrease in charge is outside its resolution (71pC), it was calculated based on a single tissue acting on a single actuator. The device can be fabricated with hundreds of actuators, which would all contribute to the change in charge and improve the ability to measure tissue stiffness.

Ultimately this device would be used to track changes in stiffness due to tissue contraction and/or the application of chronic or acute tidal stretches. In airway smooth muscle tissue strips, contraction with acetylcholine has been shown to lead to a 115%

a)

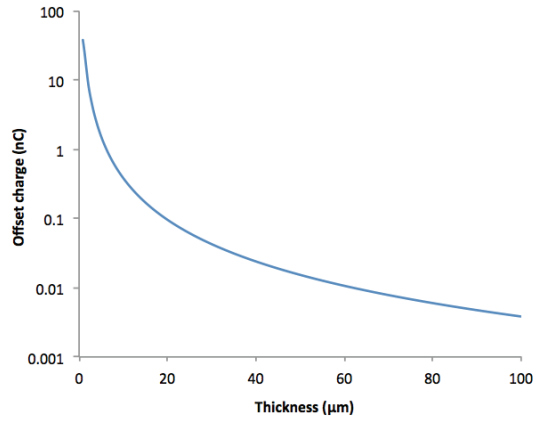

b)

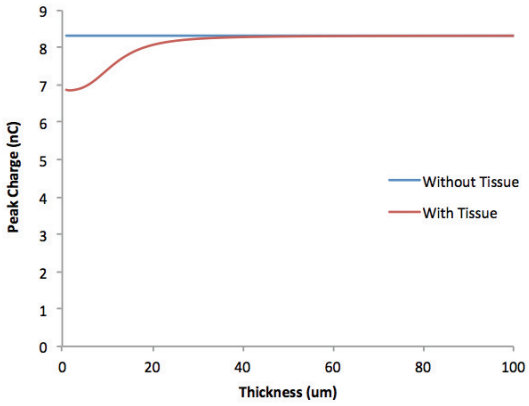

c)

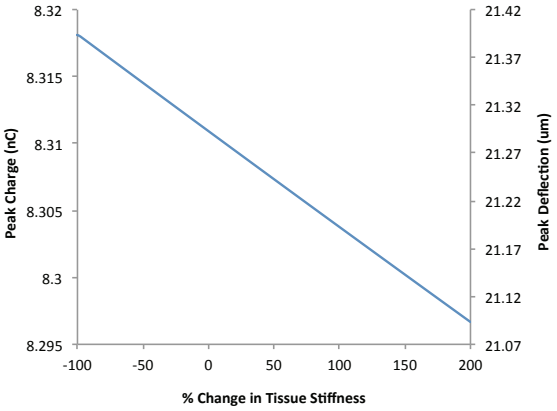

d)

Constant	Value
S_p^{11} (m^2/N)	0.131e-10
d_{31} (C/N)	-320e-12
$\boldsymbol{\varepsilon_{33}^{x}}$ (F/m)	2.771e-8
E_c (V/m)	0.78e6
t_p (m)	70e-6
l (m)	2e-3
w(m)	2e-4
E_t (Pa)	25 000
t_t (m)	100e-6
l_o (m)	600e-6

Figure 5-8: (a) The theoretical effects on offset charge and deflection, normalized to length, for a bimorph actuator with a constant tip force of 20µN when varying the piezoelectric layer thickness. (b) The theoretical effect on peak charge with stretching an elastic tissue when varying the piezoelectric layer thickness while the actuator length was kept constant at 2mm. (c) The theoretical effects on peak charge and deflection for a 70µm thick, 2mm long bimorph actuator when the tissue stiffness is changed. (d) The constants used in the model.

increase in stiffness, which was reduced to 15% with the delivery of an acute oscillatory stretch of ±4% (14). In cultured airway smooth muscle cells, contraction with potassium chloride has been shown to lead to a 129% increase in stiffness in control, non-stretched cells, and a 171% increase in stiffness in chronically stretched cells (49). As for the device's ability to measure these changes, the peak charge and deflection as a function of tissue stiffness is shown in Figure 5-8c). The change in peak charge on a single actuator

due to muscle contraction or relaxation is too small to be measured, but again, if there were hundreds of actuators this method would be capable of investigating stretch and pharmacologically induced changes in tissue stiffness.

Chapter 6: Conclusions

In this thesis, I constructed a novel platform to probe cellular contractile and phenotypic responses in the presence or absence of dynamic mechanical strain of self-assembled, miniature, tissue engineered constructs in a high-throughput manner. Although the fabrication process was challenging, in the end the device consisted of parylene coated piezoelectric bimorph actuators in an array format. The actuators were shown to be capable of delivering ±5% continuous oscillatory stretch of a microtissue with living cells at breathing frequency. Furthermore, by optically tracking submicron changes in peak deflection, the device was found capable of measuring changes in oscillatory microtissue stiffness due to pharmacological agents and the delivery of an acute stretch. Preliminary data showed that tissue stiffness significantly decreased in a strain dependent manner. This finding is in agreement with current views of cytoskeleton fluidization, and directly reflects the ability of a deep inspiration to reverse ASM contraction and lead to dilation of the airways. I also provided proof of concept for an alternative method to track actuator free deflection and an applied force based on measuring the generated electrical charge on the actuators. Furthermore, the ability of this method to track changes in tissue contractility and dynamic stiffness was discussed and it was found that it should be capable as long as the device contained enough actuators with attached tissues.

6.1 Statement of Contributions

[1] Developed and discussed the success of three different protocols used to fabricate an

array of miniature piezoelectric unimorph or bimorph actuators. Furthermore, the deflection and force production of actuators fabricated with successful methods were characterized.

[2] Showed that the device was capable of achieving ±5% stretch of an array of ASM/fibroblast microtissues at breathing frequency with negligible cell mortality.

[3] Preliminary results showed that the device was capable of measuring oscillatory stiffness changes in the microtissues due to pharmacological conditions and delivery of acute oscillatory stretch.

[4] Preliminary results showed that ASM/fibroblast microtissues responded to acute oscillatory stretch through a striking decrease in stiffness similar to previously published findings in ASM *ex-vivo* tissue strips and *in-vitro* cell culture.

[5] Provided proof of concept that a self-sensing method can be successfully applied for the array of miniature actuators to measure their peak deflection and an externally applied force.

6.2 Future Directions

Device Fabrication

[1] To improve the device's sensitivity to the mechanical properties of the microtissues,

the actuator stiffness needs to be reduced through changes in dimensions or materials. An actuator stiffness of 5-10uN/um is recommended as this would allow for easier measurements of tissue contractility and stiffness while the desired ±5% stretch can still be achieved. It may, however, be difficult to achieve this actuator stiffness with a reasonable actuator length using the methods outlined in this thesis. Accordingly, I would recommend investigating the use of thin film techniques so actuators with thinner piezoelectric layers may be fabricated, and the use of piezoelectric polymers, which have a lower Young's modulus compared to PZT.

[2] Perhaps one of the biggest limitations to the device compared to the *passive* microtissue model is the length of the actuators. In order to achieve the ±5% tissue stretch with the current actuator thickness, the actuators had to be made much longer, and as a consequence, the amount of collagen and cells that needed to be compacted to form the tissues was much greater. This likely meant that the tissues had a thickness much greater than the 100μm thickness measured in tissues formed in the *passive* microtissue model. Although I had plans to characterize the tissue thickness by measuring the calibrated distance between the top and bottom focal planes of the tissues seen through an optical microscope, the tissues were much thicker than anticipated and so a good focus could not be attained at both these locations. In future work, the tissue thickness should be characterized. Moreover, the effects of cell/collagen density and actuators length (i.e. well depth) on tissue thickness should be investigated. It may also be possible to attain the ±5% tissue stretch by lengthening the actuator in the base while reducing the exposed length of the actuator to more closely match the *passive* microtissue model.

[3] One possible reason given to explain why the magnitude of change in stiffness caused by pharmacological agents did not match previously published findings was poor cellular orientation. Since the dimensions of the actuators (i.e. width and separation) and wells (i.e. depth, width, length) likely impacted the gross tissue morphology by regulating the stresses in the tissues (i.e. the internal stresses (and cells) in skinnier tissues will be more aligned), these should be improved to produce the greatest amount of cellular alignment. I hypothesize that this may be achieved by reducing the width and depth of the wells (i.e. actuator width and length).

Microtissue Response to Stretch

[1] Since it has been previously been shown that chronic strain alters the stiffness recovery period in response to an acute stretch in single cells, it would be interesting to investigate whether chronic strain has the same effects in a 3D cell culture. Moreover, chronic strain in 2D cell culture has also been shown to affect proliferation, contractile specific protein expression, cytoskeletal remodeling, force of generation, calcium sensitivity, velocity of shortening, and shortening capacity. All of these changes could be investigated in 3D cell culture using the device.

[2] In addition to a change in loading, the stretch-induced pro-contractile response seen in 2D cell culture is also hypothesized to be due to an increase in baseline tone. Therefore it would also be interesting to study the microtissue response after a chronic incubation with both a long-acting relaxation agonist or contractile agonist.

[3] Since the cellular phenotype is likely regulated by the ECM protein composition and mechanical properties, these factors should be altered to most closely match *in vivo* conditions.

References

1. **Ammit AJ, Armour CL, and Black JL**. Smooth-muscle myosin light-chain kinase content is increased in human sensitized airways. *American journal of respiratory and critical care medicine* 161: 257-263, 2000.

2. **An SS, Bai TR, Bates JH, Black JL, Brown RH, Brusasco V, Chitano P, Deng L, Dowell M, Eidelman DH, Fabry B, Fairbank NJ, Ford LE, Fredberg JJ, Gerthoffer WT, Gilbert SH, Gosens R, Gunst SJ, Halayko AJ, Ingram RH, Irvin CG, James AL, Janssen LJ, King GG, Knight DA, Lauzon AM, Lakser OJ, Ludwig MS, Lutchen KR, Maksym GN, Martin JG, Mauad T, McParland BE, Mijailovich SM, Mitchell HW, Mitchell RW, Mitzner W, Murphy TM, Pare PD, Pellegrino R, Sanderson MJ, Schellenberg RR, Seow CY, Silveira PS, Smith PG, Solway J, Stephens NL, Sterk PJ, Stewart AG, Tang DD, Tepper RS, Tran T, and Wang L**. Airway smooth muscle dynamics: a common pathway of airway obstruction in asthma. *The European respiratory journal : official journal of the European Society for Clinical Respiratory Physiology* 29: 834-860, 2007.

3. **Bateman ED, Hurd SS, Barnes PJ, Bousquet J, Drazen JM, FitzGerald M, Gibson P, Ohta K, O'Byrne P, Pedersen SE, Pizzichini E, Sullivan SD, Wenzel SE, and Zar HJ**. Global strategy for asthma management and prevention: GINA executive summary. *The European respiratory journal : official journal of the European Society for Clinical Respiratory Physiology* 31: 143-178, 2008.

4. **Chang TY, Yadav VG, De Leo S, Mohedas A, Rajalingam B, Chen CL, Selvarasah S, Dokmeci MR, and Khademhosseini A**. Cell and protein compatibility of parylene-C surfaces. *Langmuir : the ACS journal of surfaces and colloids* 23: 11718-11725, 2007.

5. **Deng L, Fairbank NJ, Cole DJ, Fredberg JJ, and Maksym GN**. Airway smooth muscle tone modulates mechanically induced cytoskeletal stiffening and remodeling. *Journal of applied physiology* 99: 634-641, 2005.

6. **Deng L, Fairbank NJ, Fabry B, Smith PG, and Maksym GN**. Localized mechanical stress induces time-dependent actin cytoskeletal remodeling and stiffening in cultured airway smooth muscle cells. *American journal of physiology Cell physiology* 287: C440-448, 2004.

7. **Dunsch RB, J.M.** Unified mechanical approach to piezoelectric bender modeling. *Sensors and Actuators A: Physical* 134: 436-446, 2007.

8. **Elias JA, Zhu Z, Chupp G, and Homer RJ**. Airway remodeling in asthma. *The Journal of clinical investigation* 104: 1001-1006, 1999.

9. **Fabry B, Maksym GN, Butler JP, Glogauer M, Navajas D, and Fredberg JJ**. Scaling the microrheology of living cells. *Physical review letters* 87: 148102, 2001.

10. **Fabry B, Maksym GN, Butler JP, Glogauer M, Navajas D, Taback NA, Millet EJ, and Fredberg JJ**. Time scale and other invariants of integrative mechanical behavior in living cells. *Physical review E, Statistical, nonlinear, and soft matter physics* 68: 041914, 2003.

11. **Fish JE, Ankin MG, Kelly JF, and Peterman VI**. Regulation of bronchomotor tone by lung inflation in asthmatic and nonasthmatic subjects. *Journal of applied physiology* 50: 1079-1086, 1981.

12. **Fredberg JJ**. Airway narrowing in asthma: does speed kill? *American journal of physiology Lung cellular and molecular physiology* 283: L1179-1180, 2002.

13. **Fredberg JJ**. Airway smooth muscle in asthma: flirting with disaster. *The European respiratory journal : official journal of the European Society for Clinical Respiratory Physiology* 12: 1252-1256, 1998.

14. **Fredberg JJ, Inouye D, Miller B, Nathan M, Jafari S, Raboudi SH, Butler JP, and Shore SA**. Airway smooth muscle, tidal stretches, and dynamically determined contractile states. *American journal of respiratory and critical care medicine* 156: 1752-1759, 1997.

15. **Fredberg JJ, Inouye DS, Mijailovich SM, and Butler JP**. Perturbed equilibrium of myosin binding in airway smooth muscle and its implications in bronchospasm. *American journal of respiratory and critical care medicine* 159: 959-967, 1999.

16. **Gosens R, Stelmack GL, Dueck G, McNeill KD, Yamasaki A, Gerthoffer WT, Unruh H, Gounni AS, Zaagsma J, and Halayko AJ**. Role of caveolin-1 in p42/p44 MAP kinase activation and proliferation of human airway smooth muscle. *Am J Physiol Lung Cell Mol Physiol* 291: L523-534, 2006.

17. **Griffith LG, and Swartz MA**. Capturing complex 3D tissue physiology in vitro. *Nature reviews Molecular cell biology* 7: 211-224, 2006.

18. **Gump A, Haughney L, and Fredberg J**. Relaxation of activated airway smooth muscle: relative potency of isoproterenol vs. tidal stretch. *Journal of applied physiology* 90: 2306-2310, 2001.

19. **Gunst SJ, Tang DD, and Opazo Saez A**. Cytoskeletal remodeling of the airway smooth muscle cell: a mechanism for adaptation to mechanical forces in the lung. *Respiratory physiology & neurobiology* 137: 151-168, 2003.

20. **Gunst SJ, Warner DO, Wilson TA, and Hyatt RE**. Parenchymal interdependence and airway response to methacholine in excised dog lobes. *Journal of applied physiology* 65: 2490-2497, 1988.

21. **Haertling GH**. Rainbow ceramics- a new type of ultra-high-displacement actuators. *Am Cer Soc Bull* 73: 101-106, 1994.

22. **Halayko AJ, Salari H, Ma X, and Stephens NL**. Markers of airway smooth muscle cell phenotype. *The American journal of physiology* 270: L1040-1051, 1996.

23. **Halayko AJ, and Solway J**. Molecular mechanisms of phenotypic plasticity in smooth muscle cells. *Journal of applied physiology* 90: 358-368, 2001.

24. **Hall DA**. Review Nonlinearity in piezoelectric ceramics. *Journal of Materials Science* 36: 4575-4601, 2001.

25. **Hughes JM, Hoppin FG, Jr., and Mead J**. Effect of lung inflation on bronchial length and diameter in excised lungs. *Journal of applied physiology* 32: 25-35, 1972.

26. **Ivan IA, Rakotondrabe M, Lutz P, and Chaillet N**. Current integration force and displacement self-sensing method for cantilevered piezoelectric actuators. *Rev Sci Instrum* 80: 126103, 2009.

27. **Ivan IA, Rakotondrabe M, Lutz P, and Chaillet N**. Quasistatic displacement self-sensing method for cantilevered piezoelectric actuators. *Rev Sci Instrum* 80: 065102, 2009.

28. **King GG, Pare PD, and Seow CY**. The mechanics of exaggerated airway narrowing in asthma: the role of smooth muscle. *Respiration physiology* 118: 1-13, 1999.

29. **Krishnan R, Trepat X, Nguyen TT, Lenormand G, Oliver M, and Fredberg JJ**. Airway smooth muscle and bronchospasm: fluctuating, fluidizing, freezing. *Respiratory physiology & neurobiology* 163: 17-24, 2008.

30. **Lambert RK, Wiggs BR, Kuwano K, Hogg JC, and Pare PD**. Functional significance of increased airway smooth muscle in asthma and COPD. *Journal of applied physiology* 74: 2771-2781, 1993.

31. **Laprad AS, and Lutchen KR**. The dissolution of intact airway responsiveness from breathing fluctuations: what went wrong? *Journal of applied physiology* 110: 1506-1507, 2011.

32. **Latourelle J, Fabry B, and Fredberg JJ**. Dynamic equilibration of airway smooth muscle contraction during physiological loading. *Journal of applied physiology* 92: 771-779, 2002.

33. **Laudadio RE, Millet EJ, Fabry B, An SS, Butler JP, and Fredberg JJ**. Rat airway smooth muscle cell during actin modulation: rheology and glassy dynamics. *American journal of physiology Cell physiology* 289: C1388-1395, 2005.

34. **Lauzon AM, Tyska MJ, Rovner AS, Freyzon Y, Warshaw DM, and Trybus KM**. A 7-amino-acid insert in the heavy chain nucleotide binding loop alters the kinetics of smooth muscle myosin in the laser trap. *J Muscle Res Cell M* 19: 825-837, 1998.

35. **Legant WR, Pathak A, Yang MT, Deshpande VS, McMeeking RM, and Chen CS**. Microfabricated tissue gauges to measure and manipulate forces from 3D microtissues. *P Natl Acad Sci USA* 106: 10097-10102, 2009.

36. **Leguillette R, Laviolette M, Bergeron C, Zitouni N, Kogut P, Solway J, Kachmar L, Hamid Q, and Lauzon AM**. Myosin, transgelin, and myosin light chain kinase: expression and function in asthma. *American journal of respiratory and critical care medicine* 179: 194-204, 2009.

37. **Leite-Junior JH, Rocco PR, Faffe DS, Romero PV, and Zin WA**. On the preparation of lung strip for tissue mechanics measurement. *Respiratory physiology & neurobiology* 134: 255-262, 2003.

38. **Low YK, Meenubharathi N, Niphadkar ND, Boey FY, and Ng KW**. alpha- and beta-poly(vinylidene fluoride) evoke different cellular behaviours. *Journal of biomaterials science Polymer edition* 22: 1651-1667, 2011.

39. **Ludwig MS, and Dallaire MJ**. Structural composition of lung parenchymal strip and mechanical behavior during sinusoidal oscillation. *Journal of applied physiology* 77: 2029-2035, 1994.

40. **Maksym GN, Deng L, Fairbank NJ, Lall CA, and Connolly SC**. Beneficial and harmful effects of oscillatory mechanical strain on airway smooth muscle. *Canadian journal of physiology and pharmacology* 83: 913-922, 2005.

41. **Mitzner W**. Airway smooth muscle: the appendix of the lung. *American journal of respiratory and critical care medicine* 169: 787-790, 2004.

42. **Muralt P**. PZT thin films for microsensors and actuators: Where do we stand? *IEEE transactions on ultrasonics, ferroelectrics, and frequency control* 47: 903-915, 2000.

43. **Naghshin J, Wang L, Pare PD, and Seow CY**. Adaptation to chronic length change in explanted airway smooth muscle. *Journal of applied physiology* 95: 448-453; discussion 435, 2003.

44. **Oliver MN, Fabry B, Marinkovic A, Mijailovich SM, Butler JP, and Fredberg JJ**. Airway hyperresponsiveness, remodeling, and smooth muscle mass: right answer, wrong reason? *American journal of respiratory cell and molecular biology* 37: 264-272, 2007.

45. **Petrie EM**. *Epoxy adhesive formulations*. New York: McGraw-Hill, 2006, p. xv, 535 p.

46. **Puig-de-Morales M, Millet E, Fabry B, Navajas D, Wang N, Butler JP, and Fredberg JJ**. Cytoskeletal mechanics in adherent human airway smooth muscle cells: probe specificity and scaling of protein-protein dynamics. *American journal of physiology Cell physiology* 287: C643-654, 2004.

47. **Seow CY, and Fredberg JJ**. Historical perspective on airway smooth muscle: the saga of a frustrated cell. *Journal of applied physiology* 91: 938-952, 2001.

48. **Shanahan CM, Weissberg PL, and Metcalfe JC**. Isolation of gene markers of differentiated and proliferating vascular smooth muscle cells. *Circulation research* 73: 193-204, 1993.

49. **Smith PG, Deng L, Fredberg JJ, and Maksym GN**. Mechanical strain increases cell stiffness through cytoskeletal filament reorganization. *American journal of physiology Lung cellular and molecular physiology* 285: L456-463, 2003.

50. **Smith PG, Garcia R, and Kogerman L**. Strain reorganizes focal adhesions and cytoskeleton in cultured airway smooth muscle cells. *Experimental cell research* 232: 127-136, 1997.

51. **Smith PG, Moreno R, and Ikebe M**. Strain increases airway smooth muscle contractile and cytoskeletal proteins in vitro. *The American journal of physiology* 272: L20-27, 1997.

52. **Smith PG, Roy C, Dreger J, and Brozovich F**. Mechanical strain increases velocity and extent of shortening in cultured airway smooth muscle cells. *The American journal of physiology* 277: L343-348, 1999.

53. **Smith PG, Roy C, Fisher S, Huang QQ, and Brozovich F**. Selected contribution: mechanical strain increases force production and calcium sensitivity in cultured airway smooth muscle cells. *Journal of applied physiology* 89: 2092-2098, 2000.

54. **Trepat X, Deng L, An SS, Navajas D, Tschumperlin DJ, Gerthoffer WT, Butler JP, and Fredberg JJ**. Universal physical responses to stretch in the living cell. *Nature* 447: 592-595, 2007.

55. **Wang L, Liu HW, McNeill KD, Stelmack G, Scott JE, and Halayko AJ**. Mechanical strain inhibits airway smooth muscle gene transcription via protein kinase C signaling. *American journal of respiratory cell and molecular biology* 31: 54-61, 2004.

56. **Wang L, Pare PD, and Seow CY**. Selected contribution: effect of chronic passive length change on airway smooth muscle length-tension relationship. *Journal of applied physiology* 90: 734-740, 2001.

57. **Wang QM, Du XH, Xu BM, and Cross LE**. Electromechanical coupling and output efficiency of piezoelectric bending actuators. *Ieee T Ultrason Ferr* 46: 638-646, 1999.

58. **Wang QM, Du XH, Xu BM, and Cross LE**. Theoretical analysis of the sensor effect of cantilever piezoelectric benders. *J Appl Phys* 85: 1702-1712, 1999.

59. **Wang QM, and Cross LE**. Tip deflection and blocking force of soft PZT-based cantilever RAINBOW actuators. *J Am Ceram Soc* 82: 103-110, 1999.

60. **West A, Zaman, N., Cole, D., Walker, M., Legant, W., Chen, C., Cowley, E., Maksym, G.** Development and characterization of a 3D microtissue model of airway smooth muscle. In: *Abstract and oral presentation to 7th International Young Investigators' Symposium on Smooth Muscle*2011.

61. **West AR, Zaman N, Cole DJ, Walker MJ, Legant WR, Boudou T, Chen CS, Favreau JT, Gaudette GR, Cowley EA, and Maksym GN**. Development and characterization of a 3D multicell microtissue culture model of airway smooth muscle. *American journal of physiology Lung cellular and molecular physiology* 304: L4-16, 2013.

62. **Wheatley JR, Pare PD, and Engel LA**. Reversibility of induced bronchoconstriction by deep inspiration in asthmatic and normal subjects. *The European respiratory journal : official journal of the European Society for Clinical Respiratory Physiology* 2: 331-339, 1989.

63. **Zhang SX, R.; Shrout, T. R.** Lead-free piezoelectric ceramics vs. PZT? *Journal of Electroceramics* 19: 251-257, 2007.

I. Appendix: Bimorph Array Fabrication

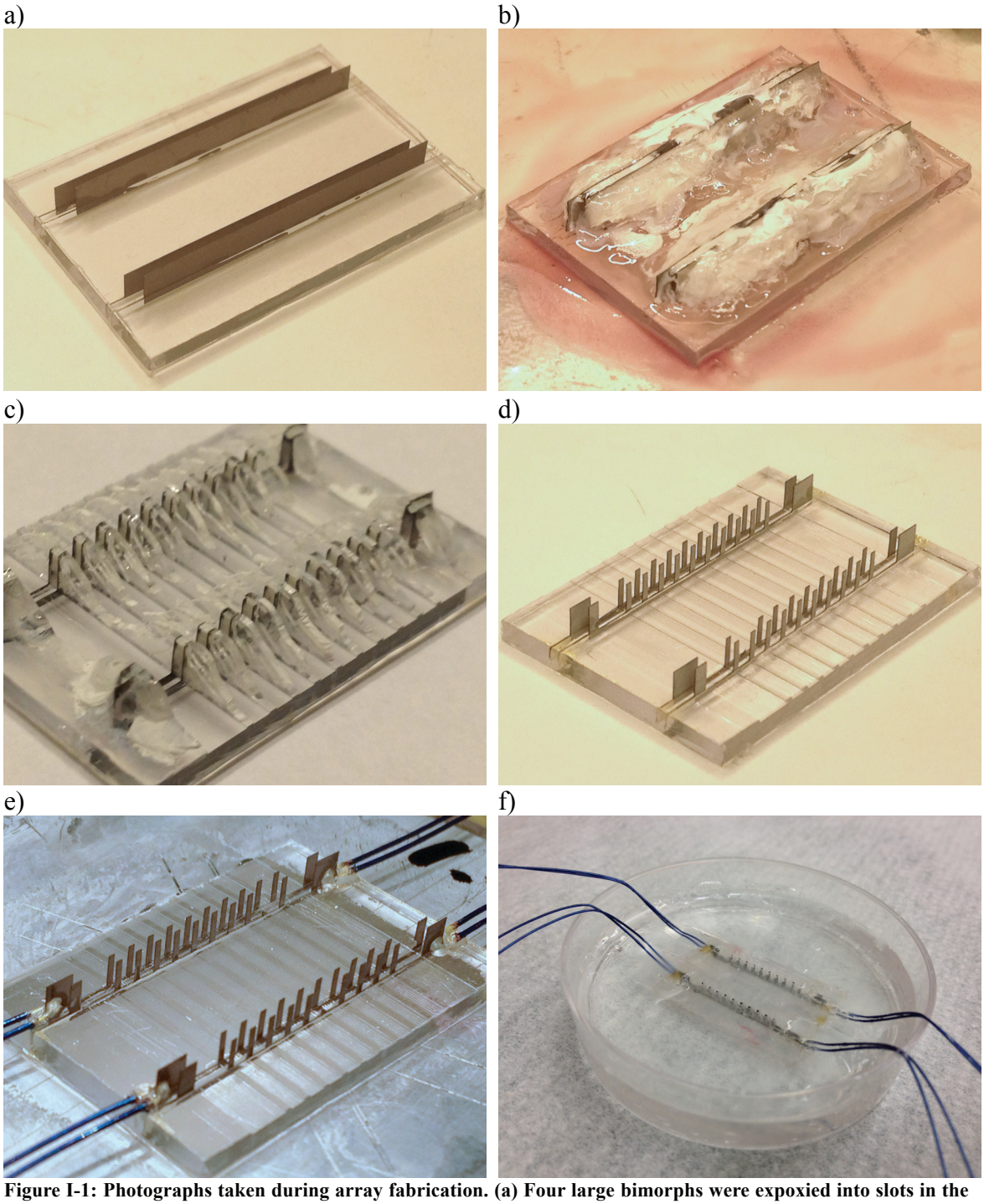

Figure I-1: Photographs taken during array fabrication. (a) Four large bimorphs were expoxied into slots in the PVC base spaced apart by the desired tissue length to create two rows of sets of actuators. (b) The sample was then encased in cyanoacrylate glue and (c) diced into many miniature actuators. (d) Once the cyanoacrylate glue was removed, (e) micro-coaxial cables were attached. (f) For the samples used to grow tissues, the PDMS wells were attached, the device was placed in a petri dish and parylene coated.

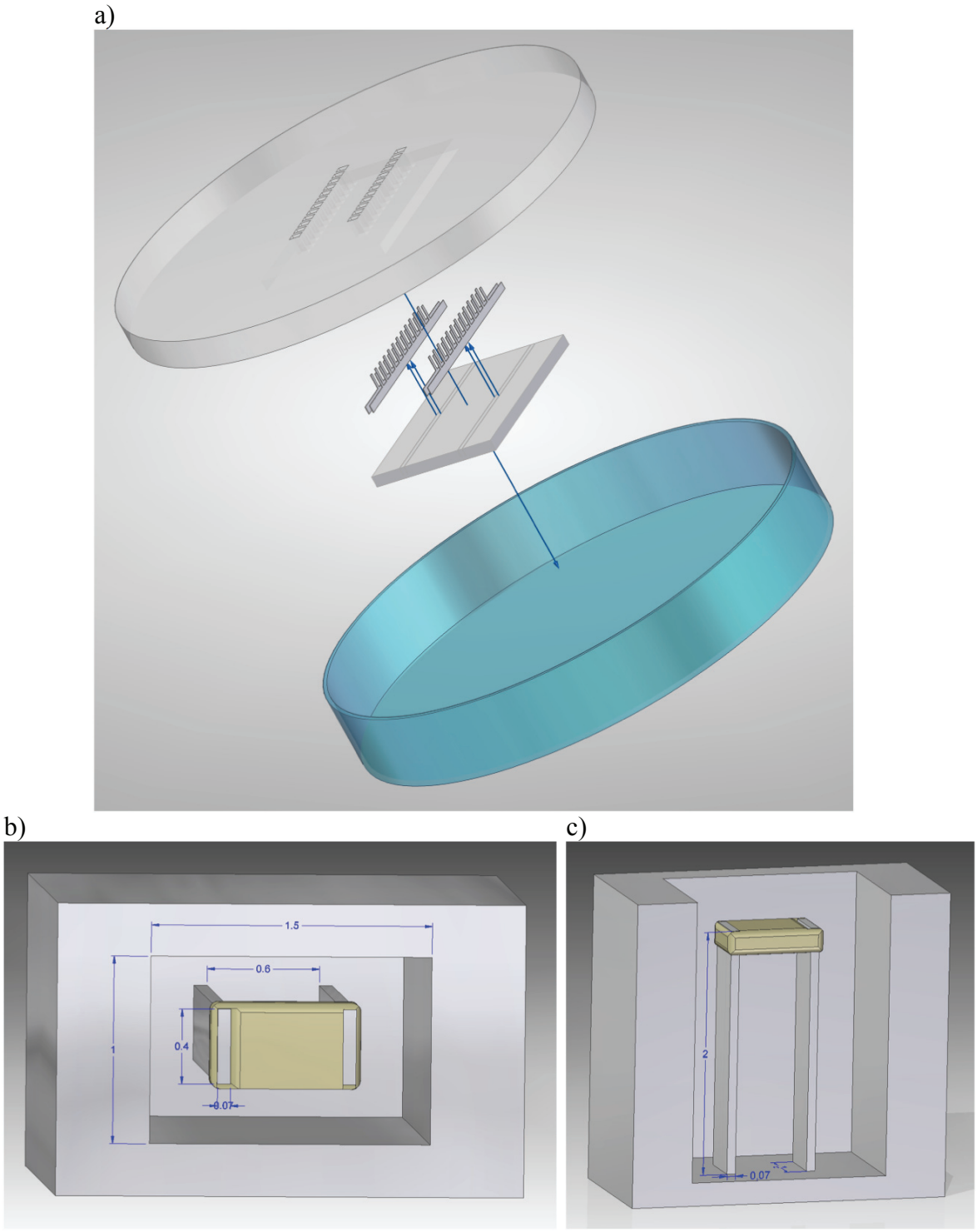

Figure I-2: Schematic drawings of the device. (a) An exploded view of the device assembly. (b) and (c) Top and side views, respectively, of a single well containing a tissue formed across the pair of actuators.

II. Appendix: Actuator Deflection Sensitivity to Lapping

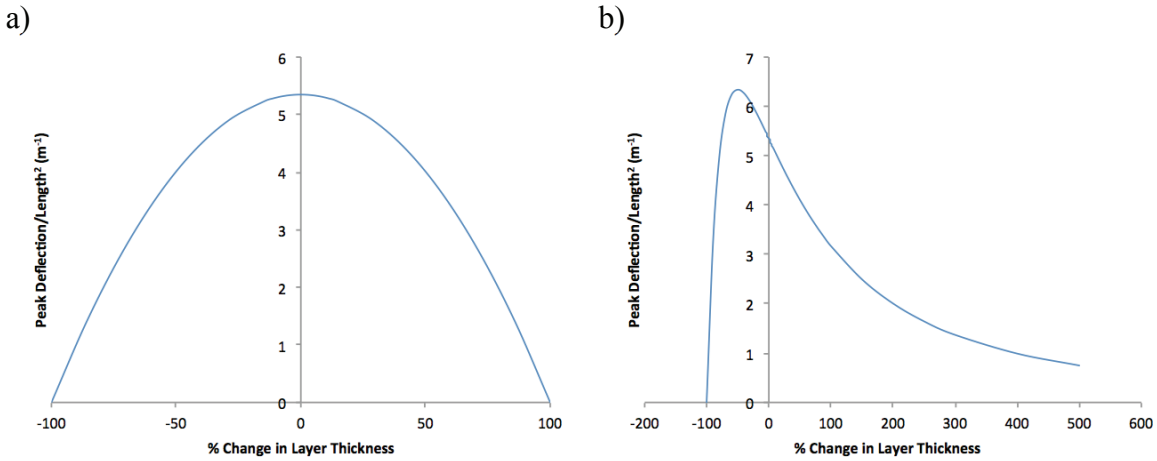

Figure II-1: The sensitivity of piezoelectric deflection of a 70µm thick bimorph actuator to a change in thickness of one layer when (a) the total actuator thickness is constant and (b) the total actuator thickness is not constant.

III. Appendix: Force Calibration and Bulk PZT Compliance

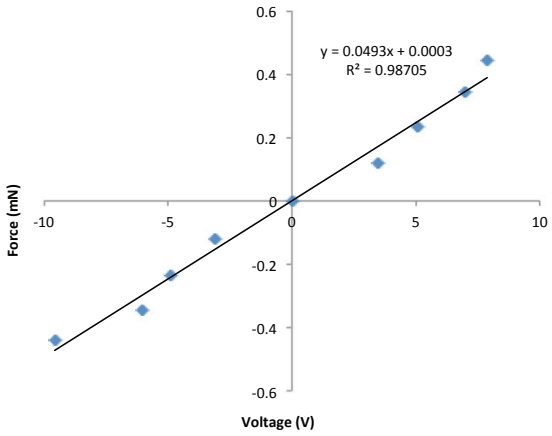

Figure III-1: The calibration of the force transducer's sensitivity. Known forces were applied to the force transducer by attaching a known mass and altering its angle with respect to the direction of gravity. The resulting voltage from the force transducer was measured and plotted with the known forces. The slope of this relationship (0.0493V/mN) was in good agreement with the given sensitivity (0.05V/mN).

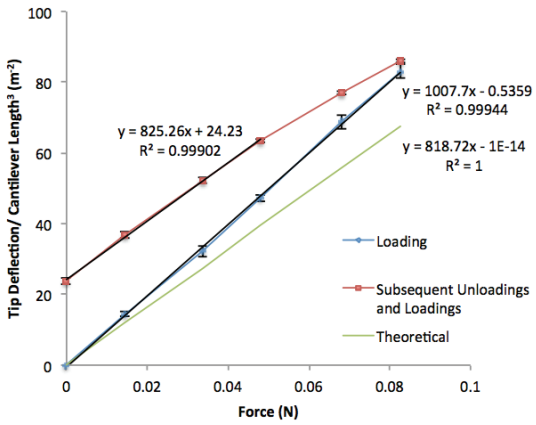

Figure III-2: The verification of the Young's modulus of PZT in bulk cantilevers. Large cantilevers (50-60mmx200µmx10mm; lxtxw) were loaded and then unloaded with known masses and the resulting deflection was measured with a digital caliper. During the first loading (blue) the cantilever compliance (i.e. slope), normalized to its length, was larger than theoretically (green) predicted due to plastic changes in the material, while the linear range of subsequent unloadings and reloadings of the cantilevers (red) were in good agreement with the theoretical value.

IV. Appendix: The Contribution of Actuator Length in the Base to the Measured Deflection

a)

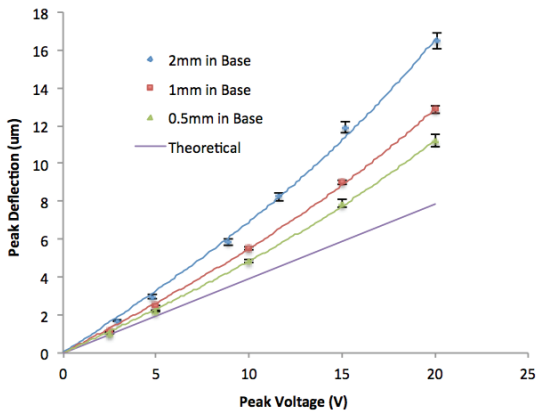

b)

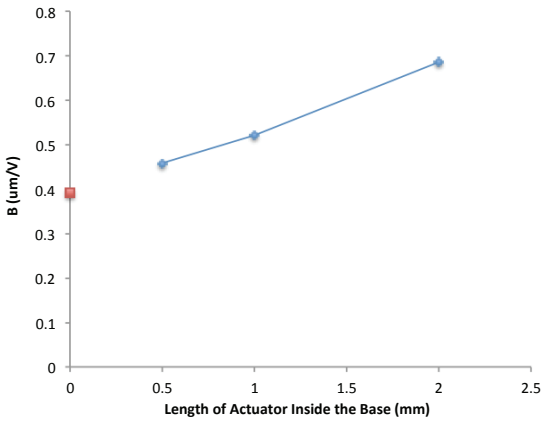

Figure IV-1: The effect of altering the length of the actuator inside the base on piezoelectric deflection at small voltages. Three sets of actuators with identical dimensions (2mmx70µmx; lxt) were fabricated with different lengths inside the base. (a) B was calculated by fitting the average deflection-voltage response for each set of actuators with a third order polynomial, differentiating with respect to voltage, and then taking the limit as the voltage approaches zero. (b) As the length of the section of the actuator inside the base approached zero, the deflection of the actuators approached the theoretical value.

V. Appendix: Explanations for Differences from Theoretical Deflection, Stiffness, and Effect of Parylene Coating

Table V-1: The measured/theoretical values and the calculated values to account for the greater than predicted deflection at low voltage.

	Measured/Theoretical value	Calculated Value	Percent Difference (%)
2mm in Base (B=0.6485μm/V)			
d_{31} (m/V)	320e-12	530e-12	49.4
Actuator Length (mm)	2	2.5730	25.1
Actuator Thickness (μm)	70	54.4	25.1
1mm in Base (B=0.4556μm/V)			
d_{31} (m/V)	320e-12	372e-12	15.0
Actuator Length (mm)	2	2.1566	7.5
Actuator Thickness (μm)	70	64.9	7.5
0.5mm in Base (B=0.328μm/V)			
d_{31} (m/V)	320e-12	328e-12	2.5
Actuator Length (mm)	2	2.0235	1.2
Actuator Thickness (μm)	70	69.2	1.2

Table V-2: The measured/theoretical values and the calculated values to account for the less than predicted non-coated actuator stiffness (33.0μN/um vs. 132.6μN/um).

	Measured/Theoretical value	Calculated Value	Percent Difference (%)
S_p^{11} (m^2/N)	1.613e-11	6.499e-11	120.5
Actuator Length (mm)	2	3.1824[1]	45.6
Actuator width (μm)	200	49.6	120.5
Actuator Thickness (μm)	70	44.0	45.6

Table V-3: The measured/theoretical values and the calculated values to account for the 24.6% increase in stiffness due to the parylene coating.

	Measured/Theoretical value	Calculated Value	Percent Difference (%)
S_p^{11} (m^2/N)	1.613e-11	1.415e-10	159.1
S_c^{11} (m^2/N)	2.381e-10	2.089e-11	167.7
Parylene Thickness (μm)	3	19.9	147.6
Actuator width (μm)	200	2.3	195.5
Actuator Thickness (μm)	70	9.2	154.0

[1] This length was calculated with the assumption that the actuator width does not change. However, when the actuators enter the base their width increases from 200μm to 22mm. This assumption, therefore, causes the calculation of actuator length to be greatly under-estimated.

Table V-4: The measured/theoretical values and the calculated values to account for the 20.8% decrease in peak piezoelectric deflection due to the parylene coating.

	Measured/Theoretical value	Calculated Value	Percent Difference (%)
S_p^{11} (m^2/N)	1.613e-11	1.968e-10	169.7
S_c^{11} (m^2/N)	2.381e-10	1.951e-11	169.7
Parylene Thickness (μm)	3	20.8	149.6
Actuator width (μm)	200	2.1	195.8
Actuator Thickness (μm)	70	8.8	155.0

VI. Appendix: Deflection Data for all Tested Bimorph Designs

a)

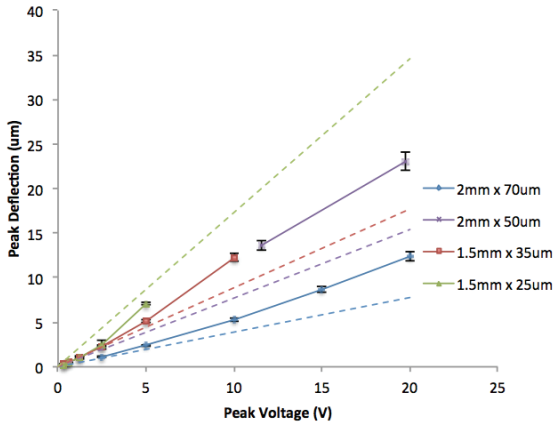

b)

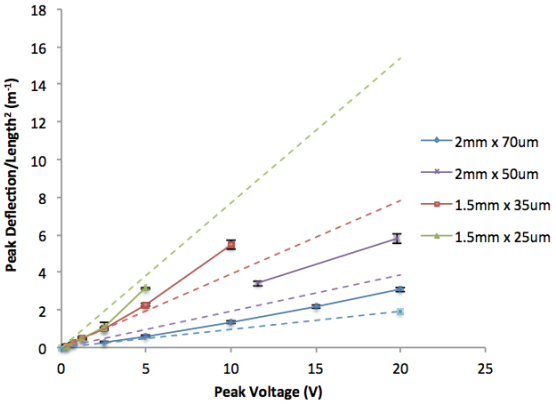

c)

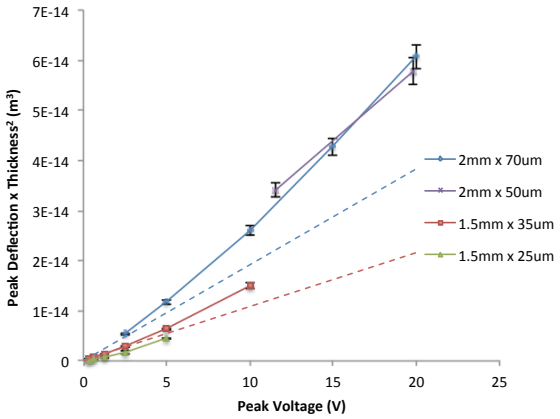

Figure VI-1: (a) The deflection-voltage relationship for all tested actuator designs. The 25µm thick actuators were the only sample that had a measured deflection less than theoretically predicted. This may have been due to an uneven layer thickness or microfractures in the material. The deflection of 50µm thick sample was only measured at two different voltages because it unfortunately broke before lower voltages could be tested. (b) The deflection was normalized to actuator length to investigate the effect of actuator thickness. (c) The deflection was normalized to actuator thickness to investigate the effect of actuator length.

VII. Appendix: The Charge Amplifier

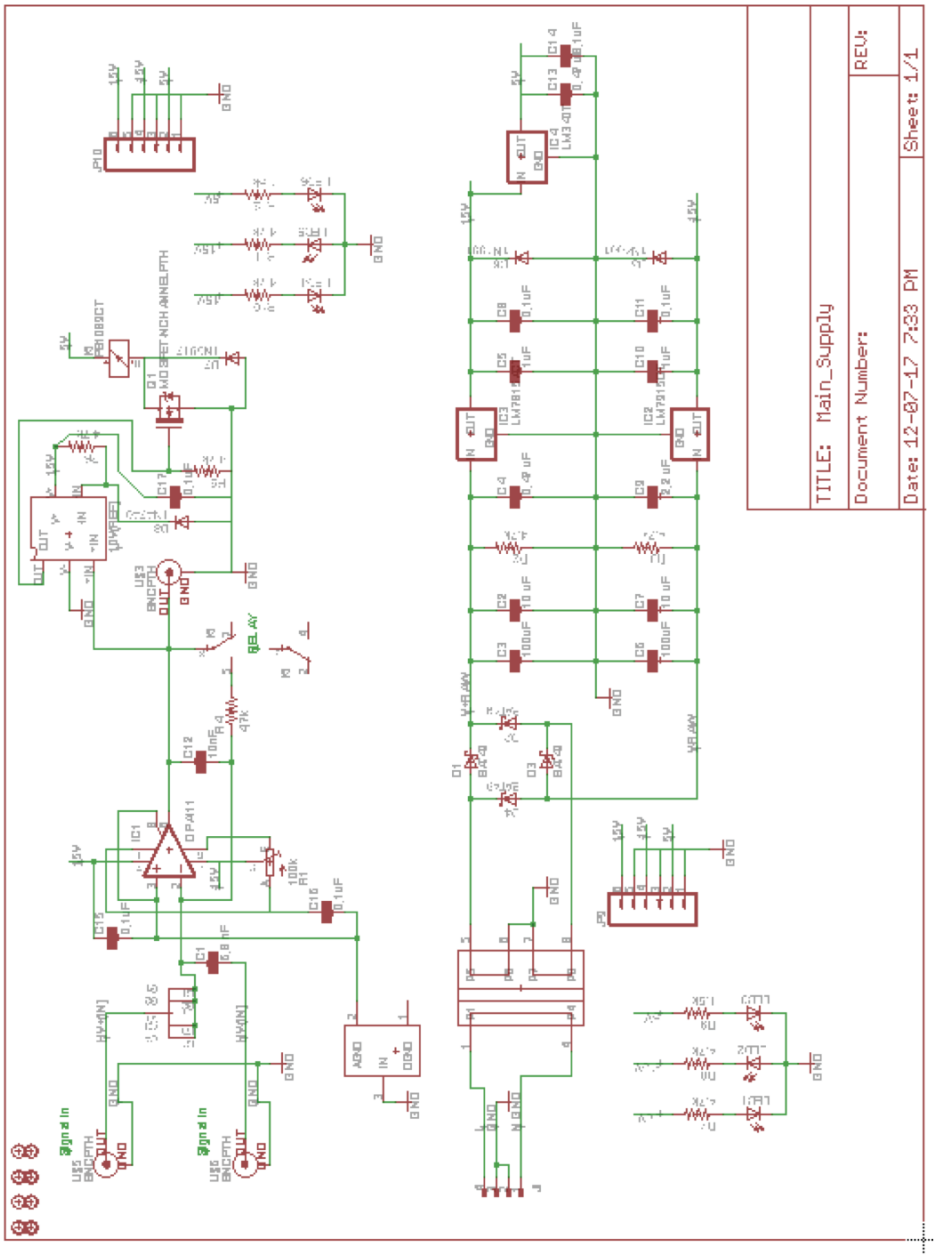

Figure VII-1: The circuit diagram for the charge amplifier designed by Andre Bezanson.

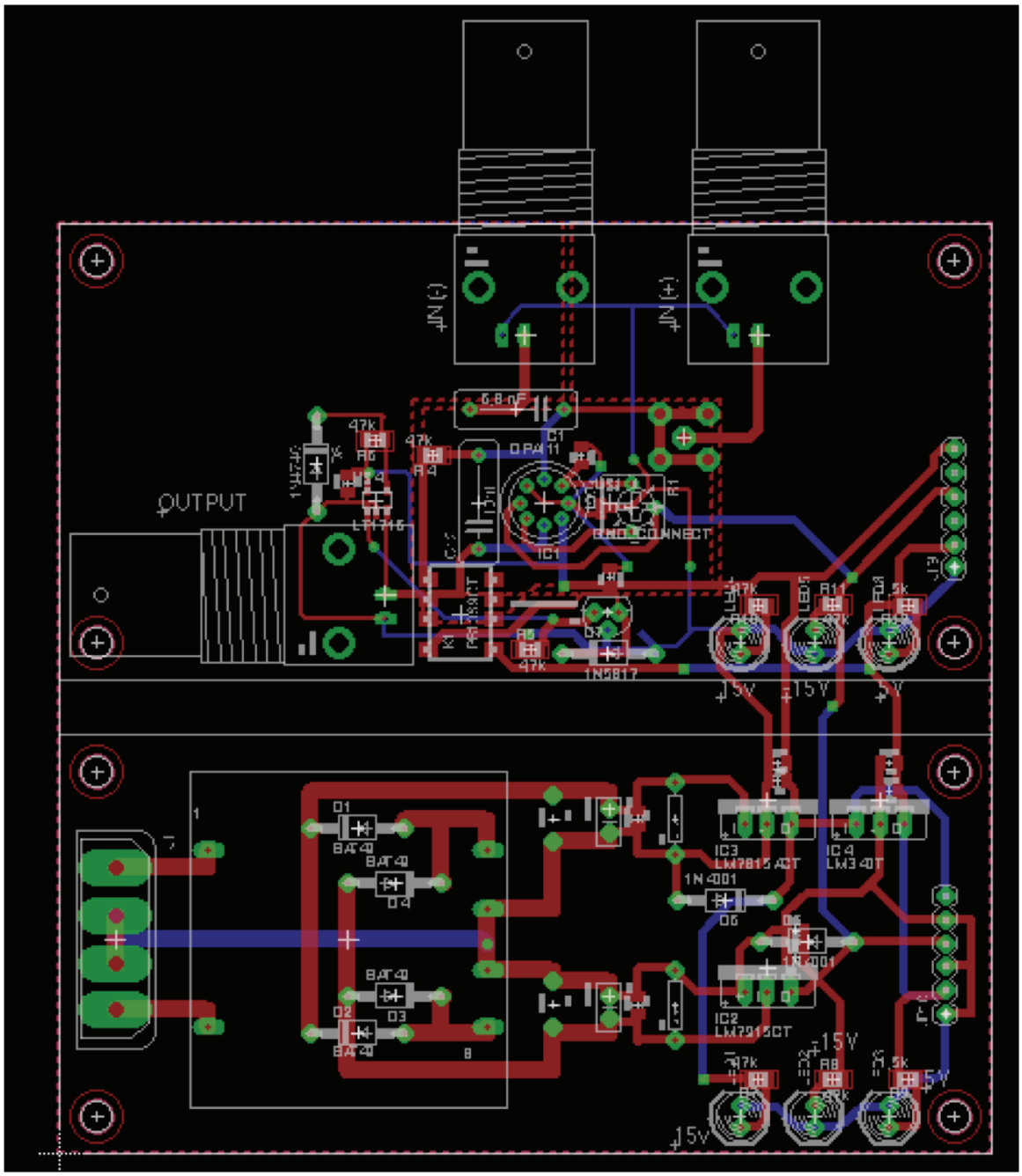

Figure VII-2: The PCB layout for the charge amplifier designed by Andre Bezanson.